Pontifícia Universidade Católica
do Rio de Janeiro

Enrico Luigi Moreira Perocco

Analysis of the blood flow during the cardiac cycle in the ascending aorta

Dissertação de Mestrado

Dissertation presented to the Programa de Pós-Graduação em Engenharia Mecânica of PUC-Rio in partial fulfillment of the requirements for the degree of Mestre em Engenharia Mecânica.

Advisor: Prof^{a}. Angela Ourivio Nieckele
Co-advisor: DSc. Ivan Fernney Ibañez Aguilar

Rio de Janeiro
September 2022

Pontifícia Universidade Católica
do Rio de Janeiro

Enrico Luigi Moreira Perocco

Analysis of the blood flow during the cardiac cycle in the ascending aorta

Dissertation presented to the Programa de Pós-Graduação em Engenharia Mecânica of PUC-Rio in partial fulfillment of the requirements for the degree of Mestre em Engenharia Mecânica. Approved by the Examination Committee:

Profª. Angela Ourivio Nieckele
Advisor
Departamento de Engenharia Mecânica – PUC-Rio

DSc. Ivan Fernney Ibañez Aguilar
Co-advisor
Departamento de Engenharia Mecânica – PUC-Rio

DSc. Guilherme Moreira Bessa
University of Alberta

Prof. Bruno Alvares de Azevedo Gomes
PUC-Rio

Rio de Janeiro

September 2022

Enrico Luigi Moreira Perocco

The author is a graduated in Mechanical Engineering from Universidade Federal Fluminense in 2017, and in Industrial Engineering in 2019 also from Universidade Federal Fluminense. Moreover, the author was an engineering exchange student for one year at the University of Colorado. He is currently a postgraduate student in the Mechanical Engineering program at PUC-Rio. He has experience in the areas of computational fluid dynamics and bioengineering subjects, oriented to the academic and scientific fields.

Bibliographic data

Perocco, Enrico Luigi Moreira

Analysis of the blood flow during the cardiac cycle in the ascending aorta / Enrico Luigi Moreira Perocco; advisor: Angela Ourivio Nieckele ; co-advisor: Ivan Fernney Ibañez Aguilar. – 2022.

148 f.: il. color. ; 30 cm

Dissertação (mestrado)–Pontifícia Universidade Católica do Rio de Janeiro, Departamento de Engenharia Mecânica, 2022.

Inclui bibliografia

1. Engenharia Mecânica – Teses. 2. Aorta ascendente. 3. Fluxo sanguíneo. 4. Ciclo cardíaco. 5. Modelagem de turbulência. 6. Escoamento em transição. I. Nieckele, Angela Ourivio. II. Ibañez Aguilar, Ivan Fernney. III. Pontifícia Universidade Católica do Rio de Janeiro. Departamento de Engenharia Mecânica. IV. Título.

CDD: 621

To my mom, Kellyda. who supported me unconditionally throughout my entire life. Your guidance was essential for me to get to this moment.

Acknowledgments

I would like to initially thank God for helping me and illuminating my path during all these years of life and for giving me the strength to obtain this master's degree.

I thank my family for always supporting me in various moments of my life, especially my parents, brothers, nephews, and grandmother, for their unconditional love, comfort, and endless support.

I also thank my best friends, Flávio, Karen and especially Loana, who were always present in moments of leisure and study and show that real friends are forever.

Thanks to all the employees of the Mechanical Engineering Department at PUC-Rio, especially to the professors that I had the opportunity to talk to and participate in during the classes.

A strong thanks to all the members of the Cardiovascular Engineering group at PUC-Rio, especially to my PhD. Advisor Angela Nieckele and Co-Advisor Dsc. Ivan Aguilar who without the support and commitment could not have completed this work.

I thank PUC-Rio in general, which despite not having many opportunities to be present due to the pandemic, proved to be an excellent and welcoming university.

This study was financed in part by the Coordenação de Aperfeiçoamento de Pessoal de Nível Superior - Brasil (CAPES) - Finance Code 001.

Abstract

Perocco, Enrico Luigi Moreira; Nieckele, Angela Ourivio; Ibañez Aguilar, Ivan Fernney. Analysis of the blood flow during the cardiac cycle in the ascending aorta. Rio de Janeiro, 2022. Número de páginas 148p. Dissertação de Mestrado – Departamento de Engenharia Mecânica, Pontifícia Universidade Católica do Rio de Janeiro.

Cardiovascular diseases are responsible for a high number of deaths in humans. Many of these pathologies are dependent on the cardiac cycle and are located in the aorta, the largest and main artery in our body. Knowledge of flow patterns and stress distributions in the walls of the aorta can help in the diagnosis and prevention of some of these diseases. Thus, the flow of blood during the cardiac cycle was numerically studied in a 3D model of the aorta of a specific patient, after TAVI (Transcatheter Aortic Valve Implantation) implantation. The cardiac cycle consists of two periods called systole and diastole. During the systole, blood is pumped from the heart to the aorta, presenting high flow rates, resulting in a turbulent flow. On the other hand, in diastole, with the closure of the aortic valve, the blood flows with low velocities in laminar regime. Until today, scientists face a challenge in turbulence modeling, as there is no single model that provides predictability for all situations involving the turbulent regime, with reasonable computational effort. In order to select the most suitable turbulence model for the analysis of the flow inside the aorta, in the presence of the transition of flow regimes during the cardiac cycle, with a reasonable cost, the methodology based on the Reynolds Average was selected. Different models were compared with experimental data extracted from the same real-scale aortic model, but a in steady state, with flow corresponding to the systolic peak. Finally, the impact of boundary conditions and turbulence models during the cardiac cycle on the distribution and values of stresses and turbulent quantities in the vascular endothelium were evaluated. It was shown that the spatial distribution of the temporal averages of tension was qualitatively and quantitatively similar, for the two cardiac cycles representative of different patients, but with small local changes for each case. In terms of turbulence models, it was observed that the SAS (Scale Adaptive Simulation) model was able to represent the relaminarization of blood flow in the diastolic period.

Keywords

Ascending Aorta; Blood Flow; Cardiac Cycle; Turbulence Modeling; Transitional Flow

Resumo

Moreira Perocco, Enrico Luigi; Nieckele, Angela Ourivio; Ibañez Aguilar, Ivan Fernney Análise do fluxo sanguíneo durante o ciclo cardíaco na aorta ascendente. Rio de Janeiro, 2022. Número de páginas 148p. Dissertação de Mestrado – Departamento de Engenharia Mecânica, Pontifícia Universidade Católica do Rio de Janeiro.

Doenças cardiovasculares são responsáveis por um elevado número de óbitos em seres humanos. Muitas dessas patologias são dependentes do ciclo cardíaco e estão localizadas na aorta, a maior e principal artéria do nosso corpo. O conhecimento dos padrões de escoamento e distribuições de tensões nas paredes da aorta podem auxiliar no diagnóstico e prevenção de algumas dessas doenças. Dessa forma, estudou-se numericamente o escoamento do sangue, durante o ciclo cardíaco, em um modelo 3D da aorta de um paciente específico, após a implantação de TAVI (*Transcatheter Aortic Valve Implantation*). O ciclo cardíaco é formado por dois períodos chamados de sístole e diástole. Durante a sístole, sangue é bombeado do coração para a aorta, apresentado altos valores de vazão, resultando em escoamento turbulento. Por outro lado, na diástole, com o fechamento da válvula aórtica, o sangue escoa com baixas velocidades em regime laminar. Até hoje, cientistas enfrentam um desafio na modelagem da turbulência, pois não existe uma única modelagem que forneça previsibilidade para todas as situações envolvendo o regime turbulento, com esforço computacional razoável. Para seleção do modelo de turbulência mais adequado para análise do escoamento no interior da aorta, na presença da transição de regimes de escoamento durante o ciclo cardíaco, com um custo razoável, selecionou-se a metodologia baseada na Média de Reynolds. Diferentes modelos foram comparados com dados experimentais extraídos do mesmo modelo aórtico em escala real, porém em regime permanente, com vazão correspondente ao pico da sístole. Por fim, avaliou-se o impacto das condições de contorno e dos modelos de turbulência durante o ciclo cardíaco na distribuição e valores de tensões e grandezas turbulentas no endotélio vascular. Mostrou-se que a distribuição espacial das médias temporais de tensão foram qualitativamente e quantitativamente similares, para os dois ciclos cardíacos representativos de diferentes pacientes, porém com pequenas mudanças locais para cada caso. Em termos dos modelos de turbulência, observou-se que o modelo SAS (*Scale Adaptive Simulation*) foi capaz de representar a relaminarização do escoamento sanguíneo no período diastólico.

Palavras-chave

Aorta Ascendente; Fluxo Sanguíneo; Ciclo Cardíaco; Modelagem de Turbulência; Escoamento em Transição.

A goal without a plan is
just a wish

Antoine de Saint-Exupéry

Summary

List of Figures

List of Tables

List of symbols and abbreviations

cm	Centimeter
D	Aortic valve diameter
D_a	Ascending Aorta average diameter
F_1, F_2	κ-ω turbulence model parameters
F_f	Face mass flux
Hg	Mercury
J_{nf}	Total flow (convective and diffusive) normal to control volume face
ℓ	Length
$\dot{m}$	mass Flow rate
m	meter
mm	milimeter
max	Maximum
min	Minimum
$\dot{m}_{ref}$	Reference Fisiological mass flow
N_f	Control Volume fase numberNúmero de faces no volume de controle
P	Pressure
$\hat{p}$	Modified pressure
Pa	Pascal
Q	Vortex identification parameter
R	Circular pipe radius
R_c	Aorta curvature average radius
R_a	Ascending Aorta average radius

Re	Reynolds number
Re_β, Re_k, Re_ω	Turbulence model parameters
Re_t	Turbulent Reynolds number
S	Strain rate magnitude
S_{ij}	Strain rate tensor
t	Time
Δt	Time-step
u	Velocity vector x component
u_j	velocity vector j componente
$\dot{\forall}$	Volumetric flow rate
v	Velocity vector y component
Δx	Average grid spacing
y^+	Dimensionless wall distance
w	Velocity vector z component
$\lvert V \rvert$	Velocoty vector magnitude

Greek Letters

a_ζ	Area average in a selected region
α, α^*, α_{t1}	K-ω turbulence model parameters
α_0^*, α_∞^*	K-ω turbulence model parameters
$\beta_{i,1}$; $\beta_{i,2}$, β_∞^*, β_i, β_i^*	K-ω turbulence model parameters ω
$c_{\theta t}$	Transition SST turbulence model paramter
δ, δ_{bl}	Transition SST turbulence model parameters
λ_θ	Thwaites´s pressure gradient coefficient

$\lambda_{\theta l}$	SAS Thwaites´s pressure gradient coefficient
θ	Momentum Thickness
θ_{bl}	Boundary layer momentum thickness
d_{κ}	Turbulent Kinetic Energy Destruction
D_{ω}	Specific turbulent dissipation rate destruction
G_{κ}	Turbulent Kinetic Energy Generation
G_{ω}	Specific turbulent dissipation rate generation
$P_{\gamma^1}, P_{\gamma^2}$	Transition SST turbulent model Destruction source terms
$E_{\gamma^1}, E_{\gamma^2}$	Transition SST turbulent model relaminaritzation source terms
$P_{\Theta t}$	Transition SST source term
$Re_{\Theta c}$	Transiton SST turbulence model transition momentum thickness Reynolds number
$\widetilde{Re}_{\Theta t}$	Transiton SST turbulence model critical Reynolds number
Re_{Ω}	Reynolds number based on Specific turbulent dissipation rate
Re_T, Re_V	Reynolds Numbers for SAS SST Turbulence Model
SC_{Φ}	Conseravation equation c source term
SP_{Φ}	Conseravation equation c source term
Γ_{Φ}	Diffusion Coeffcient
ε	Turbulent Kinetic Energy Dissipation
ϵ_{Ijk}	Levi-Civita symbol

κ	Turbulent Kinetic Energy
κ_{in}	Inlet Turbulent Kinetic Energy
μ	Blood Molecular Viscosity
μ_t	Turbulent Viscosity
$\xi_{\kappa\text{-}\varepsilon}$	Blending Factor between the κ-ω and κ-ε
ξ_i	Vorticity
ξ_ω	Vorticity Magnitude
ρ	Blood density
$-\rho\,\overline{U'_J\,U'_I}$	Reynolds Stress Tensor
$\sigma_{k,1}$; $\sigma_{k,2}$; $\sigma_{\omega,1}$; $\sigma_{\omega,2}$	K-ω turbulence model parameters
σ_{ij}	Stress Tensor
σ_k	Prandtl turbulent number of κ
σ_ω	Prandtl turbulent number of ω
$\sigma_{\theta t}$	Transition SST Turbulence Model parameter
σ_φ	SAS SST Turbulence Model parameter
τ_{ij}	Viscous Stress Tensor
τ_w	Wall Shear Stress
υ_f	Fluid cinematic viscosity
η_2	SAS SST Turbulence Model parameter
Φ	Time average variable
Φ'	Fluctuation
Φ_1; Φ_2	K-ω turbulence model parameter
Ω	Specific turbulent dissipation rate
Ω_{In}	Inlet specific turbulent dissipation rate

Ω^+	Aorta wall dimensionless specific turbulent dissipation rate
γ	Intermittency
γ_{Eff}	Effective Intermittency
Ω	Vorticity Magnitude
$\Omega\gamma$	SAS SST Turbulence model parameter
Ω_{ij}	Rotation tensor

Acronomys

3D	Tridimensional
ANSYS	Analysis System
BAV	Bicuspid Aortic Valve
BHVs	Bioprosthetic Heart Valves
CFD	Computational Fluid Dynamics
CTA	Computed Tomography Angiography
DICOM	Digital Imaging and Communication in Medicine
DNS	Direct Numerical Simulation
LES	Large Eddy Simulation
FEM	Finite Element Method
FSI	Fluid Structure Interaction
FVM	Finite Volume Method
INC	Instituto Nacional de Cardiologia

LEF	Laboratório de Engenharia de Fluidos
LV	Left Ventricule
OSI	Oscillatory Stress Index
PIV	Particle Image Velocimetry
RANS	Reynolds-averaged Navier–Stokes
SAS	Scale Adaptive Simulation
SST	Shear Stress Transport
TAP	Time Average Pressure
TAV	Tricuspid Aortic Valvle
TAVI	Transcatheter Aortic Aalve Implantation
TAWSS	Time Average Wall Shear Stress
TKE	Turbulent Kinetic Energy
TSS	Tensão principal do tensor de Reynolds
URANS	Unsteady Reynolds-averaged Navier–Stokes
WSS	Wall Shear Stress

1 INTRODUCTION

Cardiovascular illnesses are among the leading causes of death in humans. The most common disorders in this area occur in the human aorta, coronary arteries, and heart valves, and these are highly dependent on the cardiac cycle, which is composed of systole and diastole (World Health Organization, 2019).

The cardiovascular system, also known as the circulatory system, is responsible for guaranteeing the blood flow that delivers nutrients and oxygen to all cells in the body. It consists of the following organs and tissues:

- Heart: A muscular pump that forces the blood around the body
- Arteries: Vessels responsible for carrying blood away from the heart
- Veins: Vessels that bring blood back to the heart
- Capillaries: Tiny vessels that branch off from arteries to deliver blood to all body tissues

The heart, illustrated in Figure 1.1, consists of four distinct chambers: the two upper chambers are called right and left atriums, and the lower chambers are called right and left ventricles (LV). A wall separates the atriums and ventricles. The blood flow within these chambers is controlled by valves.

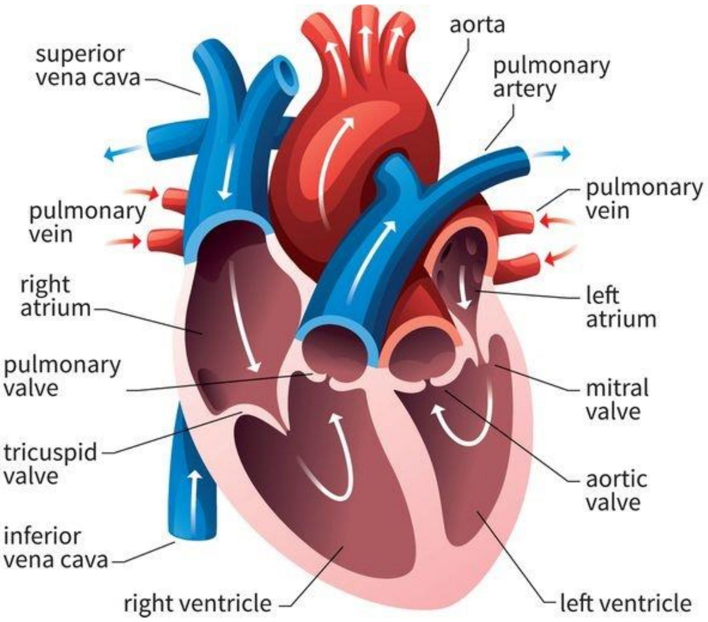

Figure 1.1 – Human cardiovascular system (Scoville, 2020).

The blood goes from the right atrium into the right ventricle via the tricuspid valve. Following a heartbeat, the ventricle pushes blood into the pulmonary artery via the pulmonic valve. This artery transports blood to the lungs, where it picks up oxygen before returning to the heart via the pulmonary vein. The oxygenated blood enters the left atrium and then descends through the mitral valve into the left ventricle. The left ventricle pushes blood through the aortic valve and into the aorta, an artery that supplies the rest of the body via a network of blood vessels. Finally, the blood returns to the heart from the body via two large blood vessels called superior and inferior vena cava. This blood is poor in oxygen since it is returning from the body where the oxygen was used. The vena cava pumps blood into the right atrium and then, the cycle starts again.

During the cardiac cycle, heart pumps blood from the left ventricle to the aorta, through the aortic valve. The aortic valve has three leaflets that open and close with each heartbeat, allowing a one-way flow of the blood (Komutrattananont *et al*., 2019).

The cardiac cycle is divided into two phases, systole and diastole. During the systole (contraction of the heart), blood flows from the left ventricle of the heart to the aorta through the opening of the aortic valve. In contrast, during the diastole (heart relaxation) the aortic valve closes, preventing blood to return to the left ventricle. Figure 1.2 graphically illustrates the flow rate inside the aorta during the systolic and diastolic periods.

Usually, the systole last 1/3 of the cardiac cycle, and due to the high flow rate, the blood flows in the turbulent regime. However, during the diastole, since the aortic valve is closed, low velocities are found inside the aorta and there is a transition to laminar flow.

The duration of a cardiac cycle depends on the number of beats a person has. Equation (1.1) can be used to calculate its duration. For example, a person with a heart rate of 75 beats per minute has a cardiac cycle that lasts 0.8 seconds, whereas a person with a heart rate of 60 beats per minute has a cardiac cycle that lasts 1 second (Mostafa *et* al., 2011 & Ostadfar, 2016). On average, the cardiac cycle lasts 0.8 seconds.

$$Duration\ (\frac{seconds}{beats}) = \frac{60\ (seconds/minute)}{Heart\ rate\ (beats/minute)} \tag{1.1}$$

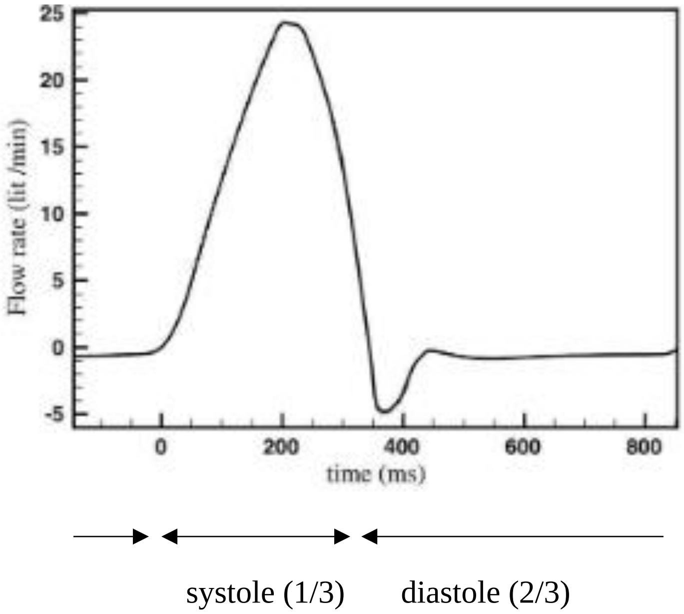

Figure 1.2 – Flow rate during the cardiac cycle. (Borazjani *et al.*, 2010).

The time variation of pressure at the left ventricle, left atrium and aorta during the cardiac cycle, shown in Figure 1.3, is known as the Wiggers diagram. This diagram shows that the process of opening and closing the aortic valve occurs due to a pressure difference between the aorta and the left ventricle, until the instant of approximately 0.25 s when the pressure in the aorta is greater than the pressure in the left ventricle. From then on, the pressure in the ventricle exceeds that of the aorta, forcing the aortic valve to remain open until 0.5s, when the aortic pressure again exceeds that of the ventricle, forcing the valve to close.

The cardiac cycle has a direct impact on human health. Several papers have been published in the literature that investigate fluid phenomena within the human vascular system. Medical simulations of circulatory function provide numerous benefits, which are being expanded not only into clinical settings but also into health-related fields such as sports medicine and rehabilitation (Lee, 2011). The engineering simulation community faces a significant problem in transferring its dynamics (CFD) to analyze hemodynamics in vascular systems allows for better diagnosis and prognosis (Brown *et al.*, 2012; Almeida *et al.*, 2019).

Bessa (2019) & Bessa *et al.* (2021) studied experimentally the flow inside the aorta model of a particular patient, considering steady state regime at the systole peak. The same aorta was investigated numerically by Ibanez (2019) & Ibanez *et al.* (2020), who studied the impact of the angle of inclination of a Transcather innovations into therapeutic applications. The use of computational fluid

Aortic Valve Implantation (TAVI) using the $\kappa - \omega$ Shear Stress Transport (SST) turbulence model and compared some of his results with Bessa (2019).

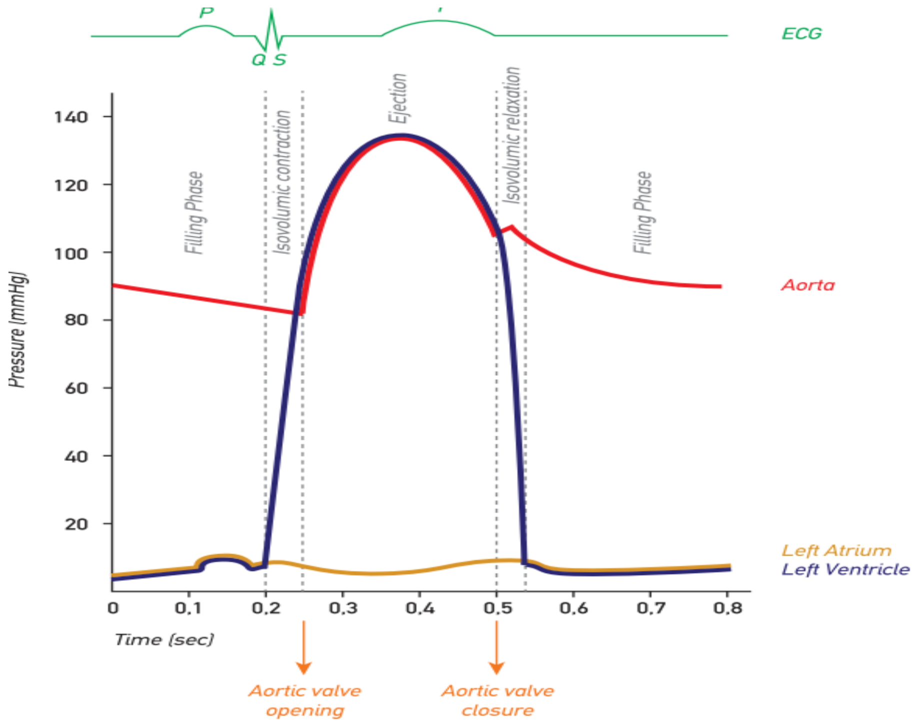

Figure 1.3 – Wiggers diagram showing the pressures in the aorta, the left ventricle, and the left atrium during the phases of the cardiac cycle (Katsi et al., 2020).

Turbulence is a phenomenon difficult to predict, due to the presence of small structures and its intermittence. Thus, there are a variety of methodologies with different models, which are more adequate for different applications (Pope, 2001). CFD simulation methods include direct numerical simulation (DNS), large eddy simulation (LES), and Reynolds Average Navier-Stoles (RANS) turbulence models. DNS is thought to be the gold standard because it provides numerical solutions to the Navier–Stokes equation at all spatial and temporal scales, without any modeling. DNS requires a very fine mesh and time step, and therefore, demands very high computational cost. LES models only the small scales (smaller than the grid size), and it has also high computational costs, although significantly smaller than DNS. RANS-based turbulence models all scales. It is less accurate, but significantly reduces computational costs. However, this approach fails to predict the flow behavior such as transition from laminar to turbulent.

The best turbulence model to predict the flow inside and aorta is still unknown, and different models have been applied in the literature, as it will be discussed in the literature review.

1.1 Objectives

The goal of this study is to use computational fluid dynamics (CFD) to numerically investigate the velocity and stress distributions (pressure and shear) in the vascular endothelium during the cardiac cycle in a specific patient's ascending aorta.

To accomplish this, a three-dimensional (3D) model of the aorta is created using computed tomography angiography images (CTA) from a patient who underwent a Transcather Aortic Valve Implantation (TAVI).

Different turbulence models are compared to high-quality experimental data of Bessa (2019), who analyzed the same aorta model in a full-scale, at steady state considering the peak of the systole. In the sequence, the flow prediction during the cardiac cycle obtained with a turbulent transitional model is compared with the results of Ibanez (2019) employing $\kappa - \omega$ SST turbulence model. Finally, the impact of changing the boundary conditions on the flow behavior and stress distribution in the vascular endothelium during the cardiac cycle is analyzed and discussed.

1.2 Organization of the manuscript

This document is divided into five chapters. The motivation and objective of this work was presented in this first chapter. The second chapter presents a literature review containing references about the areas of engineering and medicine necessary for better comprehending the theme in study, and to identify lacking areas of research where the present work can contribute. Chapter 3 reports the mathematical and numerical models necessary to obtain the results of the proposed study. Chapter 4 presents the performance of different turbulence models against experimental data of Bessa (2019), for steady state condition, while in Chapter 5 flow parameters obtained during the cardiac cycle for different pressure distribution at the aorta inlet corresponding to different cardiac cycle length, representing different patients is discussed. Finally, in Chapter 6 the conclusion and recommendations for future work are outlined.

2 LITERATURE REVIEW

The goal of this chapter is to present the most recent specialized literature on aortic anatomy as well as hemodynamic studies in the aortic region using CFD. The chapter is structured as follows. First, aorta anatomy-related works are presented. Following that, research on the most used turbulence models for analyzing blood flow in the ascending aorta is discussed. Finally, a conclusion regarding the literature is presented.

2.1 Cardiovascular Anatomy of the Aorta

The aorta, shown in Figure 2.1 is the biggest artery in the human body, it plays an important role in the blood flow in transporting oxygenated blood to supply all organs and cells. The aorta begins at the top of the left ventricle.

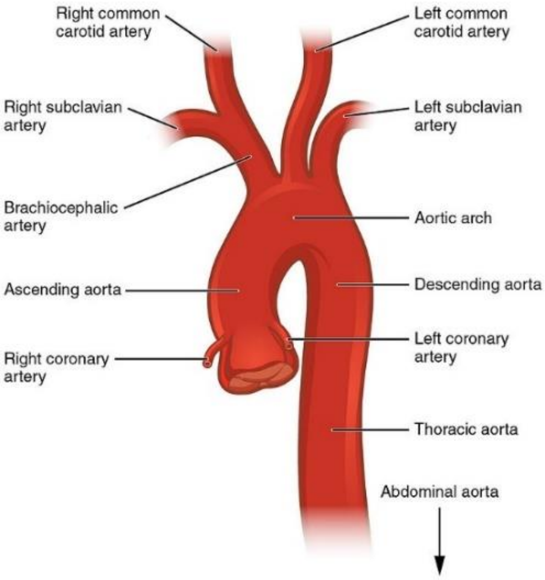

Figure 2.1 – The aorta and its divisions (Health Literacy Hub, 2021).

The aorta is divided into four sections described as follows:

- The ascending aorta curves over the heart. The coronary arteries branch off the ascending aorta to supply the heart with blood.
- The aortic arch curves over the heart, giving rise to branches that bring blood to

the head, neck, and arms.

- The descending thoracic aorta travels down through the chest. Its small branches supply blood to the ribs and some chest structures.
- The abdominal aorta begins at the diaphragm, splitting to become the paired iliac arteries in the lower abdomen. Most of the major organs receive blood from branches of the abdominal aorta.

The aortic root is the first section of the aorta containing parts of the aortic valve and connects the heart to the systemic circulation. As indicated in Figure 2.2, the aortic root consists of different parts: the aortic valve leaflets, the leaflet attachments, the sinuses of Valsalva, the inter leaflet triangles, the sinotubular junction, and the annulus.

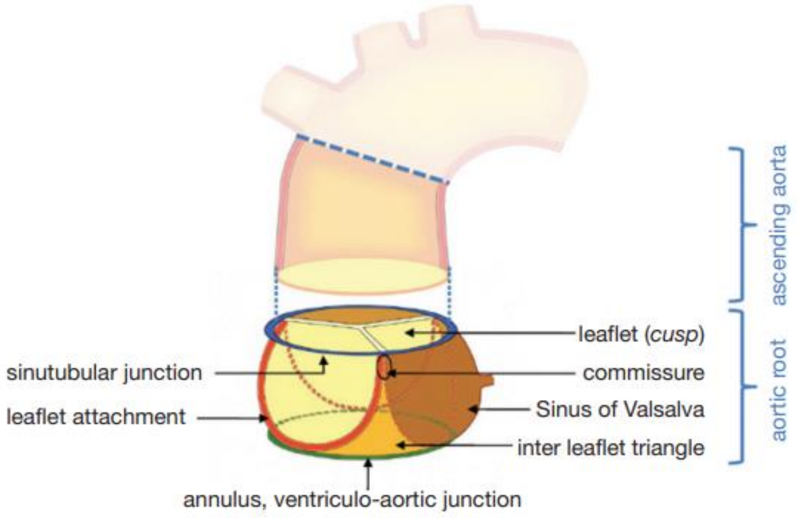

Figure 2.2 – The aortic root and its components (Charitos; Sievers, 2013).

The heart valves play an important role in the circulatory system's operation. They open and close during the cardiac cycle due to muscular contractions, ensuring one-way blood flow into and out of the heart. (Hutcheson & Aikawa, 2014).

The aortic valve is collectively called a semilunar valve as it consists normally of three semilunar-shaped leaflets that show a gentle concave curvature when viewed from above (Hussein *et al.*, 2020). These leaflets are connected at their bases to a tubular ring that provides support and approximates the valve geometry close to a circumferential shape (Piazza *et al.*, 2008).

As well as in the aorta, pathological diseases are also present in the aortic valve. Aortic stenosis is one of the most common and serious valve disease problems. In this type of disease, occurs a narrowing of the aortic valve opening, which restricts the blood flow from the left ventricle to the aorta and may also affect the pressure in the left atrium. According to Katsi *et al.* (2020), aortic valve stenosis is characterized by widespread calcification, fibrosis, thickening, and restriction of the valve's motion. In extreme situations, this can lead to a reduction in the orifice area and, eventually, heart failure symptoms. Although hearth valves have a complex shape, many researchers have studied the flow inside the aorta, representing the valve as a circular orifice (Almeida, 2019; Brown *et al.*, 2012; Gelio, 2021; Ibanez, 2019; Reymond *et al.*, 2013)

2.2 Numerical studies of blood flow through the Aorta

Over the years, the power of computer simulation techniques has advanced substantially, allowing the determination of flow in complex geometries such as the aorta. Thus, in the cardiovascular area, a new research strategy has emerged, i.e.: to characterize hemodynamics in selected patients, using the specific anatomical geometry of each patient. This type of approach is progressively used and it is considered the best representation of clinically relevant models to more reliably assess hemodynamic performance (Ibanez, 2019; Reymond *et al.*, 2013).

Cardiovascular flow simulation is a complex problem that requires extensive research and analysis time, as well as significant computational effort to solve equations. Other sources of difficulty, in addition to the geometric properties of arteries, veins, and other components related to blood flow, include selecting the mathematical models that best match the reality of the proposed problem. Moreover, the geometric domain in especial, that may or may not have iteration between its components and the flowing fluid, as in the case of the aorta with blood or only the aortic valve with blood.

Tang *et al* (2012) evaluated the stress field in an aorta with dissection in the aortic arch numerically using the $\kappa - \varepsilon$ turbulence model. They have outlined the relevance that low-stress values may have in atherosclerosis development. Later on, Simao *et al.* (2017) discussed the numerical results such as: The relationships between vortex formation, low levels of wall shear stresses, and its interaction with the atherosclerosis process and aortic wall remodeling, pointing to identify hemodynamic patterns in aneurysmal aortas.

Two recent studies (Gelio, 2021; Perocco *et al.*, 2021) analyzed the impact in the flow inside the aorta of a specific patient after a Transcatheter Aortic Valve Implantation whilst considering different simplified models of the aortic valve. While Perocco *et al.* (2021), numerically studied the flow during the peak of systole, that is, with the valve fully open, Gelio (2021) analyzed five moments of different times, varying the opening of the valve according to the chosen moment. Also, in both studies, an orifice analysis was performed and compared with the result for the maximum flow instant. Even with these differences, in both cases, it was found that the flow pattern obtained with a fully opened or an orifice was very similar. According to Gelio (2021), it can be concluded that the aortic valve leaflets have the greatest influence in the aortic root region. Once blood flow is diverted away from the aortic valve region, the hemodynamic pattern begins to resemble that produced by the circular orifice

The Cardiovascular Engineering Group of the Department of Mechanical Engineering at PUC-Rio has been carrying out several numerical studies. Overall, four undergraduate final projects, 2 Master and 2 Doctoral theses were completed between 2016 and 2021. In this research group it was investigated the flow in the ascending aorta, aiming to contribute to a better understanding of the relationship between blood flow, aortic aneurysm growth and the impact of representing the aortic valve as a orifice or as a three-dimensional body. (Gelio, 2021; Goft, 2020; Almeida, 2019; Bessa, 2019; Ibanez, 2019; Kalaun, 2019; Celis, 2017; Pinho, 2016).

Gomes *et al.* (2017) performed experiments in a 3D aorta model to assess changes in velocity, shear rate, and vorticity fields in a model based on an aortic stenosis patient who underwent to valve implantation surgery. In that study, the inclination of the valve prosthesis in relation to the aortic annulus was evaluated at various angles, considering steady state. Celis (2017) and Celis *et al.* (2020) investigated numerically the same case, discussing the impact of prosthetic valve orifice positioning on the blood flow, considering different flow rates, but also at steady state. After testing different turbulence models and comparing them with the experimental measurements from Gomes *et al.* (2017), the κ-ω SST model was recommended as the more appropriate in order to reproduce experimental results. Celis *et al.* (2020) and Gomes *et al.* (2017), in their steady state studies, showed that small variations in slope angles can modify flow patterns. Celis *et al.* (2020)

discussed that the angle between the direction of the blood jet entering the ascending aorta and the brachiocephalic trunk can induce flow recirculation in the posterior area, increasing pressure level at the aortic wall, what might lead to aneurysm growth. Goft (2020), Kalaun (2019) and Almeida (2019) compared the impact of pressure levels and other turbulent quantities on aneurysm growth in the aortas of different patients with aortic aneurysm using the $\boldsymbol{\kappa} - \boldsymbol{\omega}$ -turbulence model. Gelio (2020) and Perocco *et al.* (2021) employed the same turbulence model to evaluate the impact of an aortic valve model in the hemodynamic flow patterns in the ascending aorta. It is important to note that all these authors studied the flow inside the aorta, assuming steady state at the systole peak.

Ibanez *et al.* (2020) performed a numerical study, throughout the cardiac cycle, investigating the coaxial positioning of an aortic valve prosthesis, in a patient's aorta model, considered the movement interaction between the aortic wall and blood flow. The κ-ω SST turbulence model was employed, and Fluid Structure Simulation (FSI) were performed. In this study, the aortic valve was considered as a circular orifice. Based on the results, it was suggested that an optimal position for the valve prosthesis is when it faces the aortic left wall with an inclination of 4°. An experimental study concerning valve positioning, in the same aorta was executed Bessa *et al.* (2021) where a special configuration was designed to allow three-dimensional flow measurements at different cross-sections of the aorta. The velocimetry technique was implemented to generate instantaneous and average turbulent flow information for the variables of interest.

From the literature review, it is observed that the aortic valve is frequently modeled as a simple orifice. However, the influence of the leaflets is also discussed in the literature (Asri *et al.*, 2014; Becsek *et al.*, 2020; Borazjani *et al.*, 2010; Johnson *et al.*, 2020; Gelio, 2021; Perocco *et al.*, 2021).

Cardiovascular flow depends on the definition of the flow's inlet and outlet conditions. However, those boundary conditions are complicated to measure and there is a high cost involved. Furthermore, different patients have different cardiac cycle periods, and different variation of pressure and flow rate entering the aorta during the cycle (Brown *et al.*, 2012; Alastruey *et al.*, 2016; Lo *et al.*; 2019; Johnson *et al.*, 2020). Beyond that, the boundary conditions of the flow leaving the aorta are even harder to measured. According to Madhavan & Kemmerling, (2018) usually researchers choose between an outflow condition, in which flowrate is specified at each outlet, and an outlet with a Windkessel model, which describes the hemodynamics of an arterial system in terms of resistance, compliance and impedance (Westerhof *et al.,* 2009). Thus, it is important to determine the amount of uncertainty introduced by specification of the boundary conditions, in order to evaluate the degree to which cardiovascular flow simulations are accurate. Both Brown *et al.* (2012) and Alastruey *et al.* (2016) applied the Windkessel model to the outputs of an aortic model and considered a flow rate profile as the input condition. While the former, investigated the effects of changing the boundary conditions at the outlets, the latter analyzed and compared the results considering a FSI simulation, comparing the results between compressible and incompressible blood fluid model. Lo *et al.* (2019) also used the Windkessel model of the coronary exits in a model extracted from computed tomography images. Madhavan & Kemmerling (2018) investigated the impact of changing the inlet and outlets boundaries conditions in the aorta, the author used different inlet profiles of velocity while matching each one with the outlet conditions of flow rate and Windkessel. Finally, Ibanez *et al.* (2020) took into account a time-varying inlet pressure profile combined with a single flow profile multiplied by the outflow percentages at each of the aortic outlets according to recommendation of Alastruey *et al.* (2016).

2.3 Flow Regime in the Ascending Aorta

When inertia dominates, the flow can be classified as turbulent. Generally, the blood flow is laminar, since most of the arteries and veins in the human body are very small. However, the aorta is a large diameter vase, and at the systole peak, the flow behaves as turbulent. As mentioned at the introduction, during the cardiac cycle, approximately 1/3 of the period correspond to the systole, which is associated with high flow rate, and 2/3 of the period is the diastole, when the aortic valve is closed, corresponding to very small flow rate. Thus, the turbulent the regime can be disrupted and become laminar due to mass flow rate variations (Klabunde, 2018).

Turbulence modeling is still a challenge for engineers who want to predict fluid flow. Turbulent flow presents many eddies, that always varies in time with high frequency, and to capture all the scales and fluctuations without any further simplification, Direct Numerical Simulation (DNS) simulation can be used. But it requires a significant amount of computational processing, making its application in certain engineering fields impractical. Besides DNS, the flow can be modelled with large eddy simulation (LES), and with RANS-based turbulence models. DNS is thought to be the gold standard because it provides numerical solutions to the Navier–Stokes equation at all spatial and temporal scales. LES predicts the large eddies and models the small eddies, smaller than the computational mesh. LES also requires a refine mesh and time step, but it is not as restrictive as DNS. Since DNS and LES have high computational costs, RANS-based turbulence models have been tested as potential alternatives for aortic flow modeling but in many cases this approach fails to predict the flow behavior such as transition from laminar to turbulent (Drešar *et al.*, 2018).

In most cases of industrial interest, the engineer's interest is focused on medium-term values. This need, summed with the shortest amount of time and money has compelled the use of RANS (Reynolds-Averaged Navier-Stokes) approach the most widely used in the industry. Most models used in the industry assume that the flow is turbulent in the entire domain, yet there may be region where the flow is laminar. So, using classic turbulence models may result in significant errors to predict the required quantities. To overcome this problem, the development of RANS turbulence models that take into account the laminar-turbulent transition process has been a priority in various research groups (Menter *et al.*, 2006).

Tan *et al.* (2008) investigated different turbulence models (κ-ε/κ-ω; Transitional SST Hybrid κ-ε/κ-ω; Scale Adaptive Simulation (SAS)) to assess blood flow in a carotid artery disease. Comparing experimental data, they concluded that neither the transitional nor the fully turbulent model were superior to another, although, slightly better results were predicted with the transitional models. Singh *et al.* (2016) compared the flow characteristics and hemodynamic indices in the aorta before and after the insertion of personalized external aortic root support using combined cardiovascular magnetic resonance imaging and CFD, employing the Transition SST turbulence model. Later on, Drešar *et al.* (2018) evaluated blood flow in a mechanical bomb, employing two turbulence models, SAS SST and κ–ω SST, and compared them to experimental data. They concluded that due to the flow intermittency, the SAS-SST was the model that best approximated to the experimental data.

Concerning the LES simulation in the human aorta, Lantz *et al.* (2012) calculated the distributed flow field and the shear stress (WSS) in a subject specific human aorta wall, and Vergara *et al.* (2017) using large-eddy simulations, analyzed the effects of transition to turbulence in abdominal aortic aneurysms. Large-eddy simulation (LES) was once again used to simulate the flow through a patient-specific aorta with aortic valve stenosis (Manchester *et al.*, 2021).

Despite the existence of theories and models that explain a large portion of these phenomena, there is no single theory that provides predictability to a variety of situations involving turbulent flow. So, choosing the best turbulence model is one of the first steps that should be taken before analyzing a flow.

2.4 Conclusion

Cardiac diseases are one of the leading causes of death today. Furthermore, the aorta is a critical component for the proper functioning of the human heart, as noted in the preceding literature review.

In terms of numerical simulation of blood in the aorta, there are few studies in the literature that model the blood flow and the valve in coupled form employing FSI. Most work neglect the aortic compliance, due to the complexity of solving an FSI simulation, as well as the extra computational cost and time required for its resolution. Thus, one alternative is to only use the CFD technique to analyze blood flow, neglecting the aortic compliance, and eliminating the presence of the valve, treating the valve as a circular orifice.

Although the flow through the aorta is periodic in time, several authors only analyzed the flow at the systole peak, and/or compared different points in the cardiac cycle with and without the aortic valve. From the works examined, the impact of boundary conditions during the cardiac cycle on hemodynamic parameters in the wall is not well understood.

Finally, choosing the best turbulence model to simulate blood flow in the aorta is critical. The authors must choose the turbulence model that best fits the flow under consideration while also producing the most realistic results and being numerically solvable given the available hardware and time constraints. Due to the transition of regimes during the cardiac cycle, LES models are very attractive. However, due to the high simulation costs, URANS models, which incorporated the ability to capture transition are a very attractive alternative.

From the review presented, one can assess that there are still a few gaps to be fulfilled with regards to the prediction of the flow field inside the aorta to assist physicians in the diagnosis of potential cardiovascular diseases as well as the development of solutions to avoid them. Searching for an accurate, fast and with low-cost prediction, the representation of the valve as an orifice seems to be reasonable. The most adequate turbulence model is not a consensus with the different authors, and the availability of high-quality experimental data can aid in this selection. Although several works focus on the systole peak, it is important to evaluate the impact of different cycles period and inlet flow/pressure condition in the pressure and stress at the aortic wall.

3 CASE STUDY MODELING

The present study is based on the study of the blood flow inside the aorta of a particular patient who had a Transcatheter Aortic Valve Implantation (TAVI). This research was approved by the ethics committee of the National Institute of Cardiology, INC/MS.

The first step to determine the flow is to define the domain of interest, which was determined from a computed tomography angiography (CTA) exam of the patient selected for this analysis (Figure 3.1). In the sequence, a mathematical model must be selected, and the desired numerical investigation of the flow of blood within the aorta during a cardiac cycle can be carried on. In this manner, pressure and shear distributions, velocities, and other auxiliary quantities described throughout the work can be analyzed.

In the next section, the steps for obtaining the domain of interest will be presented, followed by the mathematical and numerical model to determine the blood flow inside the aorta.

3.1 Modeling the patient´s aorta

From a series of CTA slices, obtained from the patient exam, the DICOM (Digital Imaging and Communication in Medicine) images were transferred to the software Mimics (Materialise, Belgium). shows the orthogonal views related to the patient's computed tomography angiography (CTA) exam.

The first step of the pre-processing process consists of segmentation of the aortic region, which implies separating the object of interest from the image provided by the exam, which in this case is the aorta. After excluding organs such as the heart, ribs, end of the thoracic aorta, among others, a three-dimensional model of the aorta is generated. Image processing was performed using two software: i) FIJI (open-source image processing software based on ImageJ), and ii) Mimics (Materialise, Belgium).

Figure 3.2 presents the resulting computational domain, corresponding to the three-dimensional model of the aorta of the patient under study (Ibanez, 2019). It is important to mention that patient's aorta and the aortic valve diameter were obtained via the tomography.

Figure 3.1 – Orthogonal views of the computed tomography of the chosen patient (Ibanez, 2019).

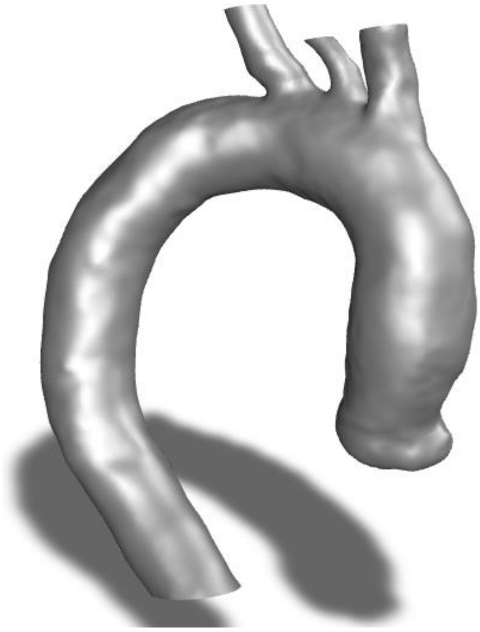

Figure 3.2 – Aorta computational domain generated.

3.2 Conservation Equations for the Fluid (Blood)

According to Pope (2001) flows can be classified based on the level of turbulence. Different levels of turbulence can directly impact the velocity and temperature and consequently the wall shear stress and pressure. The flow regimes are defined as follows and illustrated in Figure 3.3 in the same order are presented.

- Laminar: is characterized by particles moving in parallel layers, or sheets, without interfering with the path of other particles.
- Transitional: the fluid fluctuates intermittently in a laminar flow, but this is insufficient to characterize turbulent flow.
- Turbulent: A flow in which there are constant fluctuations in the flow and particles invade the path of adjacent particles, mixing and moving randomly.

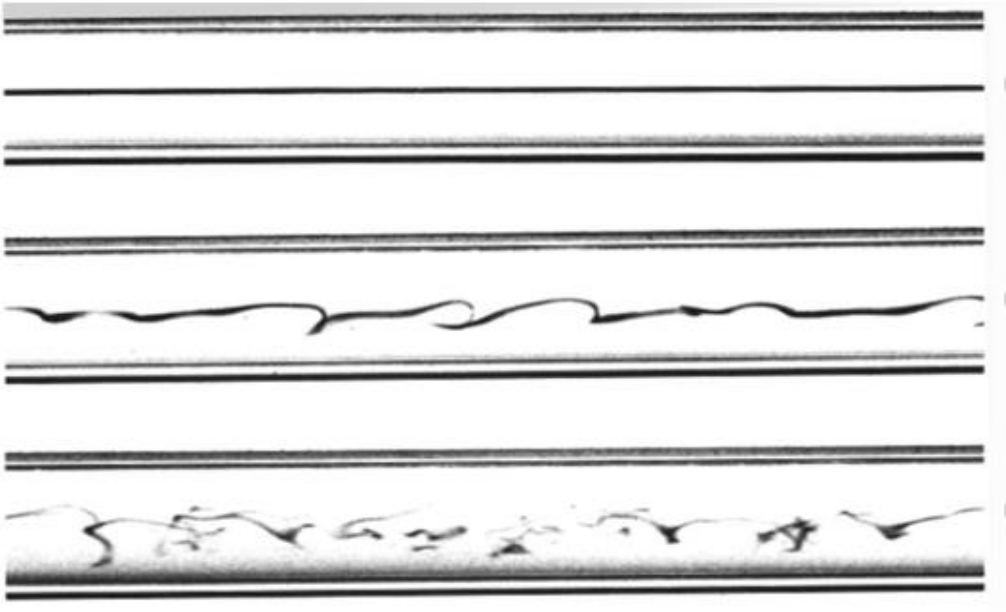

Figure 3.3 – Laminar, Transitional and Turbulent flow in (Abraham *et al.*, 2010)

The flow field through the aorta is governed by its geometry and by flow regime, which depends on the Reynolds number, defined as the ratio of inertial forces to viscous forces.

$$Re = \frac{\rho \, V_{in} \, D}{\mu} = \frac{4 \, \dot{m}}{\pi \, D \, \mu} \tag{3.1}$$

where V_{in} is the average inlet velocity in the cross section with area A_t, $\dot{m}$ is the mass flow rate, ρ and μ are the density and dynamic viscosity. D_h is the hydraulic diameter, and P_m is the wetted perimeter. $D_h = D$ for a circular cross section pipe.

To determine the flow, several hypotheses were defined, which are described below:

- Negligible gravitational force: assumed that they are very small when compared to pressure forces.
- Crossflow transition due to crossflow vortices was neglected.
- Negligible vascular compliance: variations in the diameter of the aorta were neglected due to its small variation (Ibanez, 2019).
- Incompressible fluid within operating conditions, that is, it was considered that blood density ρ is constant (Feijó, 2007).
- Blood is modeled as a Newtonian fluid (Crowley & Pizziconi, 2005; Almeida *et al.*, 2021), and the viscosity μ was also considered as a constant.
- Since body temperature is approximately constant the flow was modeled as isothermal (Hao, 2010).

To determine the flow field, considering the hypothesis listed, the following conservation equations of mass and momentum must be solved:

$$\frac{\partial\, u_j^*}{\partial x_j} = 0 \tag{3.2}$$

$$\frac{\partial\, \rho\, u_i^*}{\partial t} + \frac{\partial\, \rho\, u_i^*\, u_j^*}{\partial x_j} = -\frac{\partial\, p^*}{\partial x_i} + \mu \frac{\partial^2 u_i^*}{\partial x_j^2} \tag{3.3}$$

where x_j represents each of the coordinate axes and u_j^* the components of the velocity vector and p^* is the pressure.

According to Celis, (2017); Davies *et al.*(1986) and Gomes *et al.* (2017), the flow in the ascending aorta at the systole peak is turbulent. However, during the diastole, the flow rate is very low corresponding to laminar flow, therefore during the cardiac cycle a transition between regimes occurs.

Turbulent flow is characterized by multiple scales which fluctuates in times. Further, the size of the scales is inversely proportional to the Reynolds number. Thus, to predict a turbulent flow, small time step and very fine meshes are necessary, which very often is not practical. Therefore, to model the blood turbulent flow, it is convenient to solve in an approximate way. Here, it was chosen the approach based on the Reynolds average methodology, which consists of considering that all variables can be decomposed into an average variable over time Φ and its fluctuation ϕ', where the time interval Δt to be considered must be large enough to eliminate fluctuations, but small enough to capture the temporal variables of the average flow.

$$\phi^* = \Phi + \phi' \quad ; \quad \Phi = \frac{1}{\Delta t}\int_{\Delta t} \phi \, dt \tag{3.4}$$

The conservation equations for the mean flow are obtained through the temporal average of each equation, resulting in the URANS methodology (Pope, 2001). The time-average mass conservation equation or continuity equation, is analogous to the instantaneous equation

$$\frac{\partial \, u_j}{\partial x_j} = 0 \tag{3.5}$$

where u_j are the components of the time average velocity vector. Using the aforesaid hypotheses, the time-average linear momentum conservation equation is

$$\frac{\partial \, \rho \, u_i}{\partial t} + \frac{\partial \, \rho \, u_j \, u_i}{\partial x_j} = -\frac{\partial \, p}{\partial x_i} + \mu \frac{\partial^2 u_i}{\partial x_j^2} - \frac{\partial \, \rho \, \overline{u_j' \, u_i'}}{\partial x_j} \tag{3.6}$$

In this equation, $-\rho \, \overline{u_j' \, u_i'}$ is the turbulent tensor, also called the Reynolds stress tensor. Using the Boussinesq approximation (Schmitt, 2008; Pope, 2001; Wilcox, 1993), the deviator part of the Reynolds tensor (trace-free) can be modeled based an analogy with the viscous stress tensor, the coefficient of proportionality being the turbulent viscosity $\mu_t$which depends on the flow, such as

$$-\rho \, \overline{u_j' \, u_i'} + \frac{2}{3} \rho \, \kappa \, \delta_{ij} = \mu_t \, 2 \, S_{ij} \tag{3.7}$$

Here, S_{ij} is the strain rate tensor, corresponding to the symmetric part of the velocity gradient tensor

$$S_{ij} = \frac{1}{2}\left[\frac{\partial u_i}{\partial x_j} + \frac{\partial u_j}{\partial x_i}\right] \tag{3.8}$$

In the Eq. (3.7), the second term, proportional to the turbulent kinetic energy of the flow, can be interpreted as a turbulent dynamic pressure

$$\kappa = \frac{1}{2}\,\overline{u'_k\,u'_k} \tag{3.9}$$

Substituting the Reynolds stress tensor model in the momentum equation, we obtain

$$\frac{\partial\,\rho\,u_i}{\partial t} + \frac{\partial\,\rho\,u_j\,u_i}{\partial x_j} = -\frac{\partial\,\hat{p}}{\partial x_i} + \frac{\partial}{\partial x_j}\left[(\mu +\ \mu_t)\left(\frac{\partial u_i}{\partial x_j} + \frac{\partial u_j}{\partial x_i}\right)\right] \tag{3.10}$$

where $\hat{p}$ is a modified pressure that includes the turbulent dynamic pressure and is given by

$$\hat{p} = p + \frac{2}{3}\rho\,\kappa \tag{3.11}$$

The URANS methodology presents a large variety of turbulence models, depending on the definition of the turbulent viscosity, which is based on a characteristic velocity and length, as

$$\mu_t \approx \rho\,V_c\,L_c \tag{3.12}$$

The different models differ by the definition of these characteristic variables. Several models employ the turbulent kinetic energy κ to determine the characteristic velocity ($V_c = \sqrt{\kappa}$). The selection of the characteristic length is more difficult, giving rise to a large variety of turbulence models. For example, for the κ-ε (turbulent kinetic energy and its dissipation rate) model, the characteristic length is $L_c \approx \varepsilon/\kappa^{3/2}$, where ε can be interpreted as the power dissipated by an eddy, per unit mass ($\rho\ \varepsilon = 2\ \mu\ \overline{s_{ij}\ s_{ij}}$; s_{ij} is the deformation rate of the fluctuation field). For the model κ-ω (turbulent kinetic energy and specific dissipation), the characteristic length is $L_c \approx \omega/\kappa^{1/2}$ ($\omega\ =\ \varepsilon/\kappa$).

Celis *et al.* (2020), who compared the velocity field obtained inside an aorta with experimental data of Gomes *et al.* (2017) recommended the κ-ω SST (κ-ω Shear Stress Transport) turbulence model proposed by Menter (1994). This model combines the κ-ε (turbulent kinetic energy and the rate of dissipation of turbulent kinetic energy respectively) and κ-ω (turbulent kinetic energy and specific turbulent dissipation rate respectively) models. The κ-ε model is used for regions far from the walls and the κ-ω model close to the walls. The turbulent viscosity for the κ-ω SST model is given by:

$$\mu_t = \frac{\rho\,\kappa}{\omega}\,\xi_{\kappa-\omega} \tag{3.13}$$

where $\xi_{\kappa-\omega}$ refers to a blending factor between the κ-ω and κ-ε turbulence models. To determine the turbulent viscosity, it is necessary to solve the transport equation for the turbulent kinetic energy κ and the specific turbulent dissipation rate ω.

The κ-ω SST model was designed for turbulent flow, i.e., it is not able to capture the transition from laminar to turbulent regime. Therefore, it is going to investigate the performance of two additional models, based on the κ-ω SST, designed to capture the transition between flow regimes: Transition SST, and SST-SAS model. These two transitional methods differ among themselves and from the κ-ω SST by source terms in the turbulent kinetic energy transport equation.

The κ-ω SST model blending function is given by

$$\xi_{\kappa-\omega} = \frac{1}{\max\,(1/\alpha^*\,,\ S\ F_2/\,(a_{t1}\ \omega)} \tag{3.14}$$

where the term S represents the magnitude of the strain rate.

$$S = \sqrt{2\,S_{ij}\,S_{ij}} \tag{3.15}$$

and the empirical function and variables are

$$\alpha^* = \alpha^*_\infty\left(\frac{\alpha^*_0 + Re_t/Re_\kappa}{1 + Re_t/Re_\kappa}\right) \quad ; \ Re_t = \frac{\rho\,\kappa}{\mu\,\omega} \tag{3.16}$$

$$\alpha^*_\infty = 1 \ \ ; \ \ \alpha^*_0 = \frac{\beta_i}{3} \quad ; \quad Re_\kappa = 6 \ ; \ \ \alpha_{t1} = 0.31 \tag{3.17}$$

$$\beta_i = F_1\beta_{i,1} + (1 - F_1)\beta_{i,2} \quad ; \quad \beta_{i,1} = 0.075 \ \ ; \quad \beta_{i,2} = 0.0828 \tag{3.18}$$

F_1 and F_2 are damping functions, based on the wall distance y and are used to define which model to use

$$F_2 = \tanh(\Phi_2^2) \quad ; \quad \Phi_2 = \max\left[2\frac{\sqrt{k}}{0.09\,\omega\,y}\,, \qquad \frac{500\,\mu}{\rho\,y^2\,\omega}\right] \qquad (3.19)$$

$$F_1 = \tanh(\Phi_1^4) \quad ; \quad \Phi_1 = \min\left\{\max\left[\frac{\sqrt{\kappa}}{0.09\,\omega\,y}, \frac{500\,\mu}{\rho\,y^2\omega}\right], \frac{4\,\rho\,\kappa}{\sigma_{\omega,2}\,D_\omega^+\,y^2}\right\} \qquad (3.20)$$

$$D_\omega^+ = \max\left[\frac{2\,\rho}{\omega\,\sigma_{\omega,2}}\frac{\partial\,\kappa}{\partial x_j}\frac{\partial\omega}{\partial x_j}, 10^{-10}\right] \quad ; \quad \sigma_{\omega,2} = 1.168 \qquad (3.21)$$

The conservation equations for κ and ω are obtained manipulating the instantaneous and time-average momentum equations combined with the continuity equations, resulting in

$$\frac{\partial\,\rho\,\kappa}{\partial\,t} + \frac{\partial\,\rho\,u_j\,\kappa}{\partial x_j} = \frac{\partial}{\partial x_j}\left[(\mu + \frac{\mu_t}{\sigma_k})\left(\frac{\partial\kappa}{\partial x_j}\right)\right] + G_\kappa - D_\kappa \qquad (3.22)$$

$$\begin{aligned} &\frac{\partial\,\rho\,\omega}{\partial t} + \frac{\partial\,\rho\,u_j\,\omega}{\partial x_j} = \\ &= \frac{\partial}{\partial x_j}\left[\left(\mu + \frac{\mu_t}{\sigma_\omega}\right)\left(\frac{\partial\omega}{\partial x_j}\right)\right] + G_\omega - D_\omega + 2(1 - F_1)\frac{\rho\,\sigma_{\omega 2}}{\omega}\frac{\partial\,\kappa}{\partial x_j}\frac{\partial\omega}{\partial x_j} \end{aligned} \qquad (3.23)$$

where σ_κ and σ_ω are empirical κ and ω Prandtl numbers, given by

$$\sigma_k = \left[\frac{F_1}{\sigma_{\kappa,1}} + \frac{(1 - F_1)}{\sigma_{\kappa,2}}\right]^{-1} \quad ; \quad \sigma_\omega = \left[\frac{F_1}{\sigma_{\omega,1}} + \frac{(1 - F_1)}{\sigma_{\omega,2}}\right]^{-1} \qquad (3.24)$$

where $\sigma_{\kappa,1} = 1.176$; $\sigma_{\kappa,2} = 1.0$; $\sigma_{\omega,1} = 2.0$; $\sigma_{\omega,2} = 1.168$.

G_κ and G_ω are generation terms of κ and ω and D_κ and D_ω are destrution terms of κ and ω, respectively. These variables depend on the approximations employed in the derivation of different models. The source terms of the turbulent transport variables of all three models are described next sub-sections.

3.2.1 $\kappa - \omega$ SST Model

The generation and destruction of the turbulent kinetic energy are

$$G_\kappa = \tilde{P}_k = \min(P_k; 10\,\rho\,\beta_i^*\,\omega\,\kappa) \quad ; \quad D_\kappa = Y_\kappa = \rho\,\beta_i^*\,\omega\,\kappa \qquad (3.25)$$

where

$$P_k = -\rho\, \overline{u_j'\, u_i'}\, \frac{\partial u_i}{\partial x_j} = \mu_t\, 2\, S_{ij}\, \frac{\partial u_i}{\partial x_j} = \mu_t\, S^2 \qquad (3.26)$$

$$\beta_i^* = \beta_\infty^* \left(\frac{4/15 + \left(Re_t \,/\, Re_\beta \right)^4}{1 + \left(Re_t \,/\, Re_\beta \right)^4} \right) \qquad (3.27)$$

The generation and destruction of the turbulent specific dissipation are

$$G_\omega = \frac{\rho\, \alpha}{\mu_t} P_k \quad ; \quad D_\omega = \rho\, \beta_i\, \omega^2 \qquad (3.28)$$

with

$$\alpha = \frac{\alpha_\infty}{\alpha^*} \left(\frac{\alpha_0 + Re_t \,/\, R_\omega}{1 + Re_t \,/\, R_\omega} \right) \qquad (3.29)$$

$$\alpha_\infty = F_1 \alpha_{\infty,1} + (1 - F_1)\alpha_{\infty,2} \qquad (3.30)$$

$$\alpha_{\infty,1} = \frac{\beta_{i,1}}{\beta^*_{\infty,}} - \frac{\mathrm{k}^2}{\sigma_{\omega,1}\sqrt{\beta^*_{\infty,}}} \; ; \quad \alpha_{\infty,2} = \frac{\beta_{\mathrm{i},2}}{\beta^*_{\infty,}} - \frac{\mathrm{k}^2}{\sigma_{\omega,2}\sqrt{\beta^*_{\infty,}}} \qquad (3.31)$$

$$\beta^*_\infty = 0.09 \quad ; \quad Re_\beta = 8 \;\; ; \; \mathrm{k} = 0.41 \, ; \; R_\omega = 2.95; \;\; \alpha_0 = 1/9 \qquad (3.32)$$

3.2.2 Transition SST Model

The Transition SST model is based on a modification of the turbulent kinetic generation and destruction terms (Eq. 3.25) to account the transition between regimes. The generation term is given by

$$G_\kappa = \gamma_{eff}\, \tilde{P}_k \quad ; \quad \gamma_{eff} = \max(\gamma, \gamma_{sep}) \qquad (3.33)$$

where γ is the flow intermittency, and it is obtain by the solution of its transport equation. γ_{sep} is introduced to improve the predictions of separated flow transition

$$\gamma_{sep} = \min\left(C_{s1} \max\left[\left(\frac{Re_V}{3.235\, Re_{\theta c}}\right) - 1\right] F_{reattach}, 2\right) F_{\theta t} \qquad (3.34)$$

$$C_{s1} = 2 \quad ; \quad Re_V = \frac{\rho\, y^2 S}{\mu} \quad ; \quad F_{reattach} = \mathrm{e}^{-\left(\frac{Re_t}{20}\right)^4} \qquad (3.35)$$

$Re_{\theta c}$ is the critical Reynolds number where the intermittency first starts to increase in the boundary layer and it can be calculated from the empirical correlation provided by Menter *et al.* (2006), based on the transition momentum thickness Reynolds number of $\widetilde{Re}_{\theta t}$, which is obtained by the solution of its transport equation. $Re_{\theta c}$ can be determined by

$$Re_{\theta c} = \begin{cases} \widetilde{Re}_{\theta t} - 396.035 \times\ 10^{-2} - 120.656 \times 10^{-4}\widetilde{Re}_{\theta t} \\ + 868.230 \times 10^{-6}\widetilde{Re}_{\theta t}{}^{2} - 696.506 \times 10^{-9}\widetilde{Re}_{\theta t}{}^{3} \\ +174.105 \times 10^{-12}\widetilde{Re}_{\theta t}{}^{4},\ \widetilde{Re}_{\theta t} \le 1870 \\ \widetilde{Re}_{\theta t} - \\ \big(593.11 + (\widetilde{Re}_{\theta t} - 1870.0\big)\, 0.482),\ \ \widetilde{Re}_{\theta t} > 1870 \end{cases} \tag{3.36}$$

The destruction of the turbulent kinetic energy is given by

$$D_{\kappa} = \min\big(max\big(\gamma_{eff}, 0.1\big), 1.0\big)\, Y_{\kappa} \tag{3.37}$$

As described in the previous lines, to determine the source of κ, it is necessary to solve two additional transport equations. A transport equation for the intermittency γ and for the momentum thicknesses Reynolds number ($\widetilde{Re}_{\theta t}$). The intermittency determines the percentage of time the flow is turbulent (0 = fully laminar, 1 = fully turbulent) and acts on the production term of the turbulent kinetic energy transport equation in the SST model to simulate laminar/turbulence flows. Its transport equation is

$$\frac{\partial\, \rho\, \gamma}{\partial\, t} + \frac{\partial\, \rho\, u_j\, \gamma}{\partial x_j} = P_{\gamma^1} - E_{\gamma^1} + P_{\gamma^2} - E_{\gamma^1} + \frac{\partial}{\partial x_j}\left[(\mu + \frac{\mu_t}{\sigma_\gamma})\left(\frac{\partial \gamma}{\partial x_j}\right)\right] \tag{3.38}$$

where, $P_{\gamma^1} - E_{\gamma^1}$ are the transition sources defined as:

$$P_{\gamma^1} =\ C_{a1} F_{lenght}\, \rho\, S\, [\gamma\, F_{onset}]^{\,C_{\gamma 3}} \quad ; \quad E_{\gamma^1} =\ C_{e1}\, P_{\gamma^1}\, \gamma \tag{3.39}$$

where S is the strain rate magnitude, $C_{a1} = 2$; $C_{\gamma 3} = 0.5$; $C_{e1} = 1$; and F_{lenght} is an empirical correlation that controls the length of the transition region.

$$F_{lenght} = \begin{cases} 398.189 \times 10^{-1} - 119.270 \times 10^{-2}\widetilde{Re}_{\theta t} - \\ 132.567 \times 10^{-6}\widetilde{Re}_{\theta t}{}^{2}, \widetilde{Re}_{\theta t} < 400 \\ 263.404 - 123.939 \times 10^{-2}\widetilde{Re}_{\theta t} + 194.548 \times 10^{-5}\widetilde{Re}_{\theta t}{}^{2} - \\ -101.695 \times 10^{-8}\widetilde{Re}_{\theta t}{}^{3}, 400 \le \widetilde{Re}_{\theta t} < 596 \\ 0.5 - (\widetilde{Re}_{\theta t} - 596.0) \times\ 3.0.10^{-4}, 596 \le \widetilde{Re}_{\theta t} < 1200 \\ 0.3188, \widetilde{Re}_{\theta t} \le 1200 \end{cases} \tag{3.40}$$

$$F_{onset} = \max(F_{onset2} - F_{onset3}, 0) \;\; ; \;\; F_{onset3} = max\left(1 - \left(\frac{Re_t}{25}\right)^3, 0\right) \tag{3.41}$$

$$F_{onset2} = \min(\max(F_{onset1}, F^4{}_{onset1}), 2.0) \;\; ; \;\; F_{onset1} = \frac{Re_V}{2193\, Re_{\theta c}} \tag{3.42}$$

$P_{\gamma^2} - E_{\gamma^2}$ are the destruction and relaminarization sources defined as:

$$P_{\gamma^2} = C_{a2}\, \rho\, \Omega\, \gamma\, F_{turb} \quad ; \quad E_{\gamma^2} = C_{e2} P_{\gamma^2}\, \gamma \tag{3.43}$$

where Ω is the vorticity magnitude

$$\Omega = \sqrt{2\, \Omega_{ij} \Omega_{ij}} \qquad ; \qquad \Omega_{ij} = \frac{1}{2}\left[\frac{\partial u_i}{\partial x_j} - \frac{\partial u_j}{\partial x_i}\right] \tag{3.44}$$

$$F_{turb} = e^{-\left(\frac{Re_t}{4}\right)^4} \tag{3.45}$$

The values for the empirical constants are: $C_{a2} = 0.06$; $C_{e2} = 50$; $\sigma_\gamma = 1$.

The transport equation for $\widetilde{Re}_{\theta t}$ is:

$$\frac{\partial\, \rho\, \widetilde{Re}_{\theta t}}{\partial t} + \frac{\partial\, \rho\, u_j\, \widetilde{Re}_{\theta t}}{\partial x_j} = P_{\theta t} + \frac{\partial}{\partial x_j}\left[\sigma_{\theta t}(\mu + \mu_t)\left(\frac{\partial \widetilde{Re}_{\theta t}}{\partial x_j}\right)\right] \tag{3.46}$$

where the source term $P_{\theta t}$ is based on the streamwise velocity U:

$$P_{\theta t} = c_{\theta t}{}^{\frac{\rho}{t}(Re_{\theta t} - \widetilde{Re}_{\theta t})(1 - F_{\theta t})} \;\; ; \;\; t = \frac{500\mu}{\rho\, U^2} \tag{3.47}$$

$$F_{\theta t} = min\left(max\left(F_{wake} e^{\left(-\frac{y}{\delta}\right)^4}, 1.0 - \left(\frac{\gamma - 1/50}{1.0 - 1/50}\right)^2\right), 1.0\right) \tag{3.48}$$

$$\delta = \frac{500\, \Omega\, y}{U} \delta_{BL} \;\; ; \;\; \delta_{BL} = \frac{15}{2}\, \theta_{BL} \;\; ; \;\; \theta_{BL} = \frac{\widetilde{Re}_{\theta t}\, \mu}{\rho\, U} \tag{3.49}$$

$$F_{wake} = e^{-\left(\frac{Re_\omega}{10^5}\right)^2} \;\; ; \;\; Re_\omega = \frac{\rho \omega y^2}{\mu} \tag{3.50}$$

and the constants for the $\widetilde{Re}_{\theta t}$ are $c_{\theta t} = 0.03$; $\sigma_{\theta t} = 2.0$. The transition onset depends on $Re_{\theta t}$, defied by empirical correlation, $Re_{\theta t} = f(Tu, \lambda_\theta)$, where Tu is local turbulence intensity and λ is Thwaites´s pressure gradient coefficient, based on the momentum thickness θ and acceleration dU/ds in the streamwise direction.

$$Tu = \frac{100}{U}\sqrt{\frac{2}{3}\kappa} \quad ; \quad \lambda_\theta = \left(\frac{\theta^2}{\mu/\rho}\right)\frac{dU}{ds} \tag{3.51}$$

According to Langtry & Menter (2009), at the wall, the boundary condition for $\widetilde{Re}_{\theta t}$ is zero flux.

3.2.3 SAS − SST Model

The Scale-Adaptive Simulation model is an improved URANS formulation, which allows the resolution of the turbulent spectrum in unstable flow conditions.

The SAS concept is based on the introduction of the von Karman length scale into the turbulence scale equation. The information provided by the von Karman length scale allows SAS model to dynamically adjust to resolved structures in a URANS simulation, which results in a LES-like behavior in unsteady regions of the flow field. At the same time, the model provides standard URANS capabilities in stable flow regions (Younsi *et al.*, 2008). A more detailed derivation can be found in (Egorov *et al.*, 2010). The source terms of the κ and ω transport equations for the SST-SAS model as implemented in ANSYS Fluent 2021 manual are:

$$G_\kappa = P_\kappa \quad ; \quad D_\kappa = \rho\, c_\mu\ \omega\, \kappa \tag{3.52}$$

$$G_\omega = \alpha\frac{\omega}{k}G_k + Q_{SAS} \quad ; \quad D_\omega = \rho\,\beta\,\omega^2 \tag{3.53}$$

The additional source term Q_{SAS} is

$$Q_{SAS} = \max\left[\rho\,\eta_2\,k\,S^2\left(\frac{L}{L_{V\kappa}}\right)^2 - C\frac{2\,\rho\,\kappa}{\sigma_\phi}\max\left(\frac{1}{\omega^2}\frac{\partial\omega}{\partial x_j}\frac{\partial\omega}{\partial x_j},\frac{1}{\kappa^2}\frac{\partial\kappa}{\partial x_j}\frac{\partial\kappa}{\partial x_j}\right),0\right] \tag{3.54}$$

where η_2 = 3.51, σ_ϕ =2/3 and C = 2 are empirical constants. $k = 0.41$ is the von Kármán constant. L is the length scale of the modeled turbulence and $L_{V\kappa}$ is a three-dimensional generalization of the classic boundary layer definition.

$$L = \frac{\sqrt{\kappa}}{\left({c_\mu}^{1/4}\,\omega\right)} \tag{3.55}$$

$$L_{V\kappa} = max\left(k\left|\frac{U'}{U''}\right|, C_s\sqrt{\frac{k\,\eta_2}{(\beta/c_\mu - \alpha}\,\Delta}\right) \quad ;\Delta = \Omega_{\mathrm{CV}}^{1/3} \tag{3.56}$$

$$U' = S \ \ ; \ U'' = \sqrt{\frac{\partial^2 U}{\partial\, x_k^2}\,\frac{\partial^2 U}{\partial\, x_j^2}} \tag{3.57}$$

Δ is mesh spacing, Ω_{CV} is the control volume size. $c_\mu = 0.09$.

A transition model can be combined with the SAS model to simulate the transitional. In this case, the transport equation for intermittency is the following:

$$\frac{\partial\,\rho\,\gamma}{\partial\,t} + \frac{\partial\,\rho\,u_j\,\gamma}{\partial x_j} = P_\gamma \ - E_\gamma \ + \frac{\partial}{\partial x_j}\left[(\mu + \frac{\mu_t}{\sigma_\gamma})\left(\frac{\partial\gamma}{\partial x_j}\right)\right] \tag{3.58}$$

where the transitions source term is

$$P_\gamma \ = F_{lenght}\,\rho\,S\gamma\,(1-\gamma)F_{onset} \tag{3.59}$$

S is the strain rate magnitude and $F_{lenght} = 100$.

The destruction source term is

$$E_\gamma \ = C_{a2}\,\rho\,\Omega\,\gamma\,F_{turb}(C_{e2}\,\gamma - 1) \ \ ; \ F_{turb} \ = e^{-\left(\frac{Re_t}{2}\right)^4} \tag{3.60}$$

where Ω is the vorticity magnitude, $C_{a2} = 0.06, C_{e2} = 50$ and $\Omega\gamma = 1.0$. F_{onset} is controlled by the following functions

$$F_{onset1} = \frac{Re_V}{2.2\,Re_{\theta c}}; \ F_{onset2} = \min\,(F_{onset1}, 2.0) \tag{3.61}$$

$$F_{onset3} = \ max\,(1 - \left(\frac{Re_t}{25}\right)^3, 0) \tag{3.62}$$

$$F_{onset} = \ max\,(\,F_{onset2} - F_{onset3}, 0) \tag{3.63}$$

$$Re_t \ = \frac{\rho\kappa}{\mu\omega} \ \ ; \ \ Re_v \ = \frac{\rho\,{d_w}^2 S}{\mu} \tag{3.64}$$

d_w is the wall distance and $\widetilde{Re}_{\theta c}$ is a correlation used to trigger the transition model.

$$\widetilde{Re}_{\theta c}(Tu_L, \lambda_{\theta L}) = C_{TU1} + \ C_{TU2}\exp[-C_{TU3}Tu_L F_{PG}(\lambda_{\theta L})] \tag{3.65}$$

In this correlation, $\widetilde{Re}_{\theta c}$ is the critical momentum thickness Reynolds number. Tu_L and $\lambda_{\theta L}$ are variables defined that approximate the freestream turbulence intensity and the pressure gradient parameter, respectively, defined as

$$Tu_L = \min\left(\frac{100}{\omega\, d_w}\sqrt{\frac{2\kappa}{3}}, 100\right) \tag{3.66}$$

$$\lambda_{\theta L} = -0.1111\frac{dV}{dy}\frac{{d_w}^2}{\upsilon} + 0.1875 \tag{3.67}$$

For numerical robustness, $\lambda_{\theta L}$ was bounded as follows

$$\lambda_{\theta L} = min\left(\max(\lambda_{\theta L}, -10.0), 10.0\right) \tag{3.68}$$

$$F_{PG}(\lambda_{\theta L}) = \begin{cases} \min(1 + C_{PG1}, \lambda_{\theta L}, {C_{PG1}}^{lim}), \lambda_{\theta L} \geq 0 \\ \min\left(1 + C_{PG2}\lambda_{\theta L} + C_{PG3}\min[\lambda_{\theta L} + 1.0, 0\,], {C_{PG2}}^{lim}\right), \lambda_{\theta L} < 0 \end{cases} \tag{3.69}$$

With the following constants: $C_{TU1} = 100$; $C_{TU2} = 1000$; $C_{TU3} = 1.0$; $C_{PG1} = 1.0$; $C_{PG1} = -0.5$; $C_{PG3} = 0.0$; ${C_{PG1}}^{lim} = 1.5$; ${C_{PG2}}^{lim} = 3.0$; $C_{SEP} = 1.0$; $C_{RSF} = 1.0$.

3.3 Boundary and Initial Conditions

Figure 3.4 indicates the three types of boundary conditions considered for the aorta under study: i) input; ii) outlets and iii) surface of the aorta (wall). To solve the conservation equations appropriate boundary and initial conditions must be defined at the domain boundaries. To solve the conservation equations appropriate boundary and initial conditions must be defined at the domain boundaries.

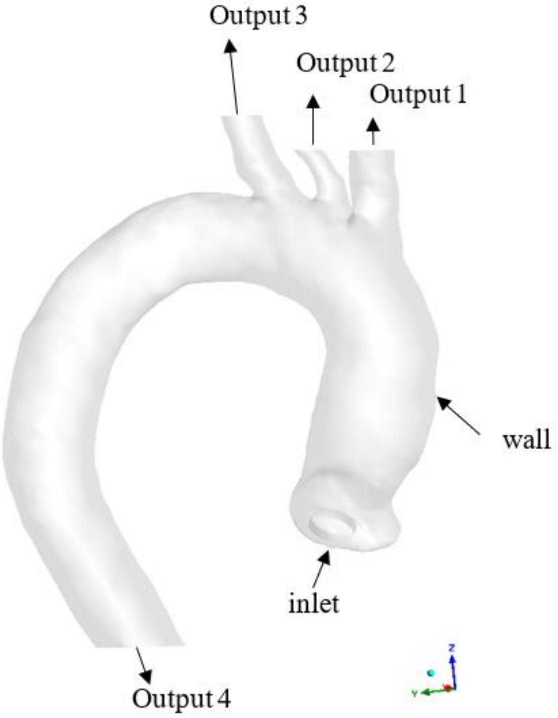

Figure 3.4 – Boundary types

3.3.1 Inlet

At the inlet, it is possible to impose along the cardiac cycle mass flow rate or pressure, with similar profiles as shown in Figure 1.2 and Figure 1.3. As already mentioned, different patients will have different cycles period as well as different inlet profiles. When mass flow rate is imposed, the velocity profile is uniform along the inlet.

In this study the same coordinate axis as employed in the experimental setup of Bessa (2019) was adopted. It is located at output 1, which is parallel to the to the $x - y$ plane and perpendicular to the axial z coordinate.

At the aorta inlet plane, the plane's normal velocity component, based on the mass flow rate, is imposed

$$V_{in} = \frac{4\,\dot{m}}{\rho\,\pi\,D^2} \tag{3.70}$$

The turbulent quantities, κ and ω are also considered uniform. The turbulent kinetic energy κ_{in} is based on the inlet mean flow kinetic energy (or inlet mean velocity V_{in}) and the turbulent intensity I

$$\kappa_{in} = \frac{3}{2}(V_{in}\, I)^2 \tag{3.71}$$

The specific dissipation ω is based on the empirical constant $C_\mu = 0.09$ and a length scale l defined equal to the inlet diameter $l = D$.

$$\omega_{in} = \frac{\sqrt{\kappa_{in}}}{{C_\mu}^{1/4} l} \tag{3.72}$$

3.3.2 Outlet

At each outlet, it possible to impose, during the cardiac cycle, the time variation of mass flow rate or pressure. With respect to the turbulent quantities, a null diffusive flow condition was applied

$$\frac{\partial}{\partial x_n} = 0 \tag{3.73}$$

where n is the direction normal to the outlets.

3.3.3 Wall

The surface of the aorta is modeled as a “wall”, i.e., no slip condition is imposed for the velocities.

$$u = v = w = 0 \tag{3.74}$$

At the aorta wall, κ is also zero. However, Menter (1994) states that the boundary condition for specific dissipation ω in the walls is given as a function of its dimensionless value defined as:

$$\omega^+ = \frac{\omega_{wall}\mu}{\rho\, u^*} \tag{3.75}$$

being u^* the friction velocity defined as follows:

$$u^* = \sqrt{\frac{\tau_{wall}}{\rho}} \tag{3.76}$$

where τ_{wall} is the the normal tangential gradient to the wall and ρ is the density of the fluid.

The dimensionless specific turbulent dissipation rate can be evaluated considering the thickness of the molecular sub layer, characterized as:

$$\omega^{+} = \min\left(2500, \frac{6}{\beta_{\infty}^{*}(y^{+})^{2}}\right) \tag{3.77}$$

being y^{+} the dimensionless wall distance

$$y^{+} = \frac{\rho u^{*} y}{\mu} \tag{3.78}$$

The fluid was defined as being incompressible, hence the pressure level is not relevant. The solution is obtained in relation to a reference pressure, defined at the inlet.

3.3.4 Initial condition

Since the represent study is concerned with a cardiac cycle, which is periodic, the initial numerical condition doesn´t affect the overall results after a stable solution is reached. Thus, to analyze the solution, a periodic solution must have been attained.

In all simulations performed in this study, the initial values for Pressure, Velocity components, turbulent kinetic energy and specific dissipation rate were computed from the inlet plane values. The intermittency (γ) value chosen was 0.5 and turbulent intensity (I) was 0.5.

3.4 Auxiliary Quantities

In this section, some auxiliary quantities will be defined. These will be a useful tool to evaluate the results of this project.

- Wall shear stress (WSS):

$$\tau_{w} = \mu \left.\frac{\partial\, u_{t}}{\partial x_{n}}\right|_{w} \tag{3.79}$$

where u_t is the tangential to the wall velocity component and x_n is the coordinate normal to the wall.

- Vorticity Magnitude (ξ_ω):

$$\xi_\omega = \sqrt{2\,\Omega_{ij}\Omega_{ij}} \tag{3.80}$$

where Ω_{ij} is the vorticity tensor defined as:

$$\Omega_{ij} = \frac{1}{2}\left(\frac{\partial u_i}{\partial x_j} - \frac{\partial u_j}{\partial x_i}\right) \tag{3.81}$$

- Q Criterion; (Hunt et al., 1988) defined as:

$$Q = \frac{1}{2}\left(\Omega_{ij}\Omega_{ij} - \mathrm{S}_{ij}\mathrm{S}_{ij}\right) \tag{3.82}$$

where S_{ij} is the strain rate tensor defined in Equation (3.8)

- Normalized Helicity:

$$H = \xi_i \frac{u_i}{\left(\sqrt{\xi_k\xi_k}\sqrt{u_l u_l}\right)} \; ; \; \xi_i = \epsilon_{ijk}\frac{\partial u_j}{\partial x_i} \tag{3.83}$$

where ξ_i is the vorticity, u_l is the velocity and ϵ_{ijk} is the Levi-Civita symbol.

To aid the analysis of the solution along the aorta an area average in a selected region A_ζ can be useful

$$\langle\phi\rangle = \frac{1}{A_\zeta}\int_{A_\zeta} \phi \, dA \tag{3.84}$$

where ϕ is any variable of interest.

Time average during the cardiac cycle is also a useful measure to evaluate the solution. The most important are:

- Time Average Pressure (TAP, *Time Average Pressure*):

$$TAP = \frac{1}{T}\int_0^T p \, dt \tag{3.85}$$

- Time Average WSS (TAWSS)

$$TAWSS = \frac{1}{T}\int_0^T |\tau_w|\mathrm{dt} \tag{3.86}$$

where T is the cardiac cycle period.

- Oscillatory Shear Index (OSI) (Ku *et al.*, 1985)

$$OSI = 0.5\left(1 - \frac{\left|\frac{1}{T}\int_0^T \tau_w \mathrm{dt}\right|}{\frac{1}{T}\int_0^T |\tau_w|\mathrm{dt}}\right) \tag{3.87}$$

3.5 Numerical Modeling

In the present work, the blood flow in the ascending aorta was determined with ANSYS tools, from pre-processing, through processing and finally post-processing. Paraview was also used for post-processing some results.

To solve numerically the flow field, after the creation of the computational domain as describe in section 3.1, the first step is the definition of the mesh distribution, which is presented in the next sub-section. Then the methods used to discretize the conservation equations are described and finally the convergence criteria.

3.5.1 Mesh

The computational mesh was created by using identical construction parameters for all simulation’s cases. The Patch Conforming algorithm was chosen alongside the Tetrahedrons method for refinement and control. As a result, the 3D inflation technique could be applied for refining the wall region to better capture pressure and velocity variations in the boundary layer.

The mesh used for all cases was refined near the walls and had an average skewness of 0.8 and an element quality above 0.85. Figure 3.5 illustrates an example of the generated mesh.

The mesh for the steady state case was defined based on the mesh study performed used by Ibanez (2019) and it consisted on approximately 1.5 million elements. However, for the transient cases, following ANSYS Fluent Manual 2021 recommendation, to capture the laminar and transitional boundary layers correctly, the mesh must have a dimensionless wall distance for the first internal nodal point, y^+ smaller than 1. Thus, in the present work, for the transient cases, the mesh was refined, and 4 million points were employed.

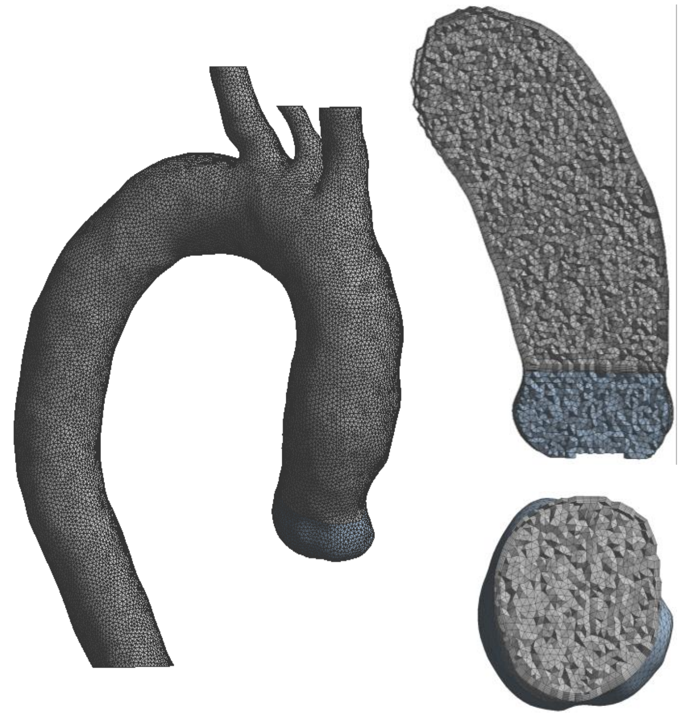

Figure 3.5 – Aorta generated mesh.

The time-step for the transient cases was set equal to 0.01 s, guaranteeing a maximum Courant number (Co) of 0.03, defined as

$$Co = \frac{U\Delta t}{\Delta x} \tag{3.88}$$

where U is the maximum characteristic velocity of the system, Δt is the time-step of the numerical model, and Δx is the average the grid spacing (Courant *et al.*, 1928).

3.5.2 Discretization method

The conservation equations implemented in ANSYS-Fluent were discretized based on the finite volume method (Patankar, 1980). The method entails dividing the computational domain into small control volumes. A node is a reference point within each control volume. The conservation equations are integrated over space in each control volume, yielding global balance of each variable of interest.

All conservation equation can be represented by

$$\frac{\partial\rho\phi}{\partial t} + \mathbf{div}\,(\boldsymbol{J}) = Sc + Sp\,\phi \quad ; \quad \boldsymbol{J} = \rho\,\boldsymbol{u}\,\phi - \Gamma_{\phi}\,\mathbf{grad}\,\phi \tag{3.89}$$

where ϕ is a variable quantity, $\boldsymbol{J}$ is formed by the convective ($\rho\,\boldsymbol{u}\,\phi$) and diffusive flux of ϕ ($-\Gamma_{\phi}\,\mathbf{grad}\,\phi$), where Γ_{ϕ} is the diffusion coefficient. $Sc_{\phi} + Sp_{\phi}\,\phi$ is the volumetric source term of ϕ.

A second-order approximation was used to treat the transient term (first term of Eq. (3.89), where n represents the current time instant, the previous instant ($n - 1$), and the new time step ($n + 1$) (Burden & Faires, 2008).

$$\int_{d\,\forall} \frac{\partial\,\rho\,\phi}{\partial\,t}\,d\,\forall = \frac{\partial}{\partial\,t}\int_{d\,\forall} \rho\,\phi\,d\,\forall = \frac{3(\rho\,\phi\,\forall)^{n+1} \;-\; 4(\rho\,\phi\,\forall)^{n} + (\rho\,\phi\,\forall)^{n-1}}{2\,\Delta t} \tag{3.90}$$

The Gauss divergence theorem and the fully implicit discretization scheme are employed to integrate the liquid flux term, second term of Eq. (3.90)

$$\int_{\Delta\forall} \mathbf{div}\boldsymbol{J}\,d\,\forall = \int_{A_f} \boldsymbol{J}\,\cdot\boldsymbol{n_f}\,dA_f = \sum_{nf} J_{nf}\,d\,A_f \tag{3. 91}$$

where $\boldsymbol{n_f}$ corresponds to the unit normal to the faces. All conservation equations were discretized with the Second-order Upwind scheme, apart from SST-SAS turbulent model.

According to recommendation of ANSYS-Fluent manual, for SST-SAS turbulent model, the Bounded Central Differencing Scheme was selected for the momentum equation with the bounded second order implicit method.

The Pressure-Velocity Coupling was solved using the Coupled scheme. The full implicit coupling is achieved by implicitly discretizing the pressure gradient terms in the momentum equations, as well as the face mass flux, including the Rhie-Chow pressure dissipation terms.

Since the conservation equations are non-linear, sub-relaxation was used to decrease the variables variation during the iterative process and guarantee convergence. The sub-relaxation parameters considered were: *i)* pressure (0.5) *ii)* momentum (0.5); *iii)* turbulent kinetic energy (0,.6); *iv)* specific dissipation rate (0.6). *v)* turbulent viscosity (0.75); *vi)* intermittency (0.6) (when needed).

The convergence criteria for all cases, consisted in enforcing the residual of all discretized equations below 10^{-6}.

4 TURBULENCE MODEL EVALUATION

This chapter presents an evaluation of three turbulence models to predict the flow inside the aorta at steady state, with flow rate corresponding to the systole peak. For this situation, a high quality data was obtained by Bessa *et al.* (2021) and Bessa (2019), who used the PIV technique to measure the velocity field inside the same model employed here of a 3D model of the human aorta. The aorta has the following geometrical parameters: aorta average curvature radius, $Rc \approx 57.4$ mm, and average radius of the aorta $Ra \approx$19.4 mm, aortic valve diameter aortic D = 16 mm.

The first turbulence models selected was $\kappa - \omega$ SST, because it was the model employed by Ibanez (2019), who compared his predictions with Bessa (2019) measurements. The other two models were selected to predict the regime transition: Transition – SST and SAS – SST. However, since in this section the flow is in steady state, to save computing time, the intermittence solution was not included in the SAS-SST model.

The aortic model was built using polydimethylsiloxane polymer, with a minimum wall thickness of 15 mm, ensuring rigidity of the aortic wall. In the experiment, a pipe with 1 meter of length was introduced connected to the aorta inlet, to ensure fully developed velocity profile at the inlet (Figure 4.1). Therefore, to allow comparison between the numerical results and experimental measurements, exactly the same domain as Bessa (2019) and Ibanez (2019) was employed, i.e.: *i)* the aortic wall was considered as rigid wall and ii) a 1 meter pipe connected to the aorta inlet was introduced in the computational domain.. Further, as already mentioned, the same mesh employed by Ibanez (2019) was defined here.

To compare the results both qualitatively and quantitatively, six planes were created parallel to the brachiocephalic artery ($x - y$ plane), where the system's origin is located, exactly as defined in the experiment. These planes are illustrated in Figure 4.1b. The first plane is located 124 mm below the origin, similarly, planes 2; 3; 4; 5 and 6 are located 109 mm; 94 mm; 84 mm; 74 mm and 64 mm below the coordinate axis origin and parallel to $x - y$ plane, respectively.

The same fluid used in the experiment was employed in the simulations: density ($\rho = 1157.4\ \mathrm{kg/m^3}$) and dynamic viscosity of ($\mu = 0.00878$ Pa s). The study was developed at steady state, with imposed volumetric flow rate at the inlet corresponding to the systolic peak ($\dot{\forall}_{in}$= 25 lt/min).

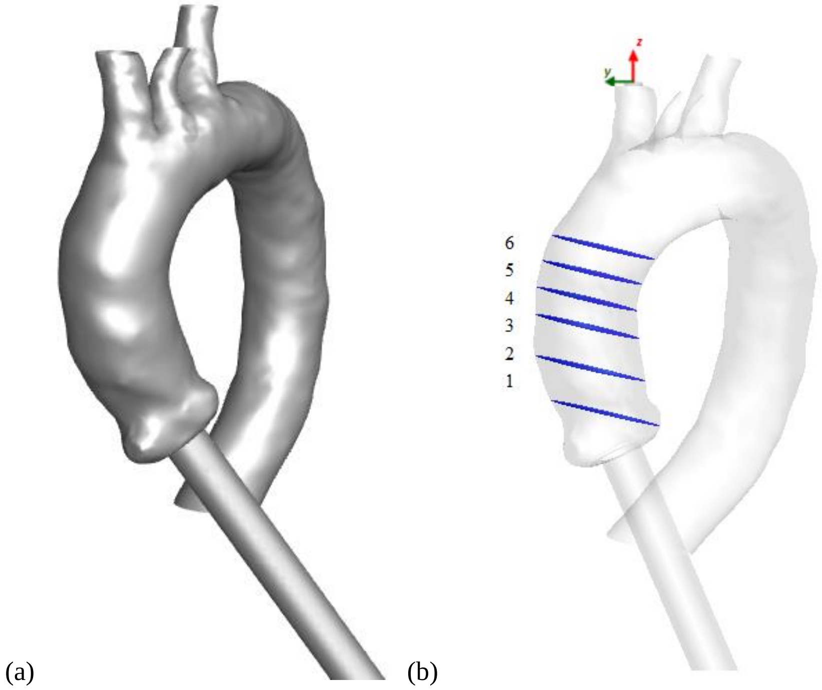

Figure 4.1 – (a) Aorta numerical domain. (b) Six planes created for the numerical-experimental comparison

For the aorta outputs (Figure 3.4), diffusion was neglected at each one of them, and a percentage of the mass inflow was imposed at each one, based on Alastrue*y et al*. (2016); Ibanez (2019) and Ibanez et al (2020) as follows: Descending aorta (output 1 – 75,0%), brachiocephalic artery (output 2 – 15%), left carotid artery (output 3 - 4%) and left subclavian artery (output 4 – 6%). In the following subsections, comparison of turbulence models' predictions and experimental measurements is shown. Bessa (2019) also guaranteed these percentage of the mass flow at each outlet in the experiment conducted by him.

4.1 Velocity (w) component

The z velocity component, w (normal to the selected planes) are examined here. Figure 4.2 shows the contours of w at all six planes selected. Qualitatively, all numerical results are like the experimental measurements. Moreover, the highest w value can be seen near the center of Plane 1, which is located close to the aortic inlet and root. For the other five planes, as one moves to the superior planes, due to the curvature of the aorta, the center of the jet approaches the aortic wall, with very similar contours shape in all numerical and experimental results. Furthermore, the order of magnitude of w was consistent across all cases with respect to maximum and minimum values. However, experimentally higher velocities w were measured. Among the turbulent models, the SAS model was the closest to the experimental data, followed by the $\kappa - \omega$, and Transition SST model.

Similar results were obtained in all cases, indicating that qualitatively the results of all analyzed turbulent models agree with the experimental measurements.

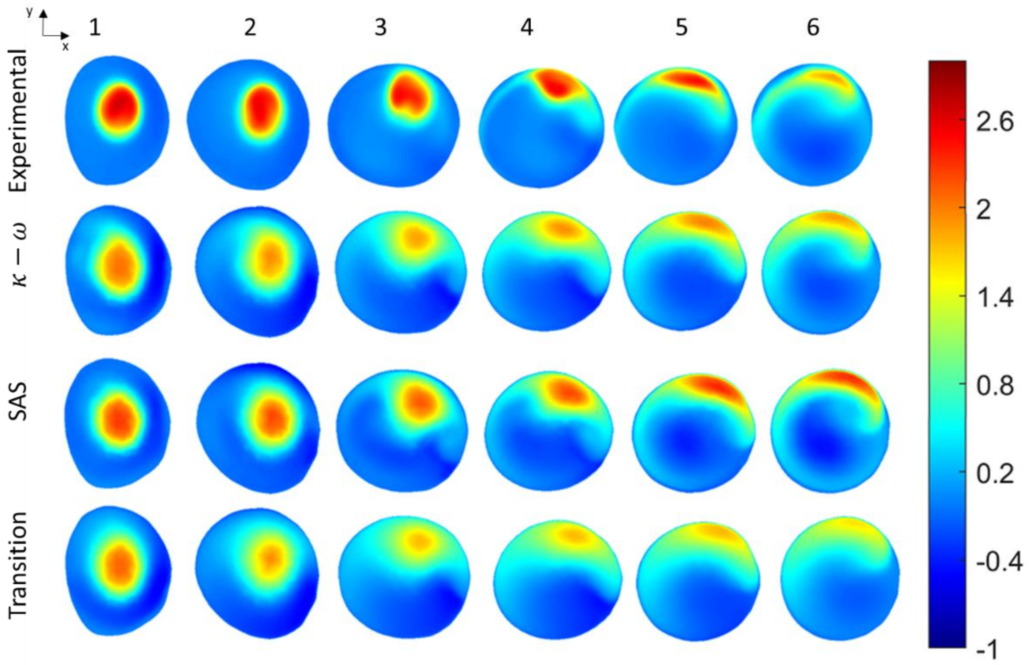

Figure 4.2 –Velocity w (m/s) component contours

A quantitative comparison was performed to better evaluate the results obtained for the z-component of velocity, w. In this analysis, the z-velocity component profiles were compared along lines parallel to the x and y axes of each plane Figure 4.3 and Figure 4.4). In the top of each figure, a cross section of the corresponding plane is indicated. Figure 4.3 – w velocity profiles along the x and y axes for Planes 1-3. Figure 4.3 corresponds to the first three planes created, and Figure 4.4 illustrates the results for planes 4-6.

Analyzing the profiles in Figure 4.3 and Figure 4.4, it can be seen very similar predictions of $\kappa - \omega$ SST and Transitional SST in all planes and both axes, since the present test corresponds to a turbulent steady state case. In all cases, SAS also predicted similar results to the other two turbulence models, but with higher maximum z-velocity than the other two turbulent models, although smaller than the measured experimental value. Smaller velocities are observed along the x-axis for planes 3 through 6, and as a result larger difference between the solutions can be seen.

Very good agreement was predicted by all models in Plane 1 (closer to the aorta´s inlet) along the x-axis, however, a displacement of the velocity peak occurred along the y-axis (Figure 4.3). As one moves away from the inlet (planes 2 and 3 in Figure 4.3 and planes 4 to 6 in Figure 4.4), the positioning of the velocity peak was reasonable well predicted by all models. Significant lower velocities are seen along the x-axis, for Planes 3 through 6, with a slightly larger difference between the prediction, but with a good prediction of the reverse flow direction.

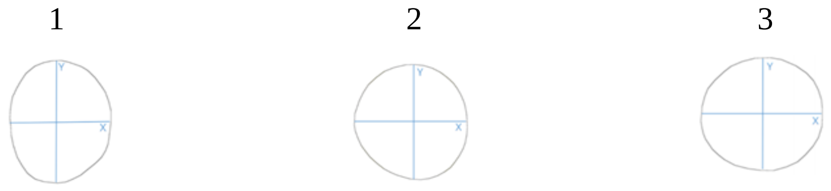

a) Reference planes

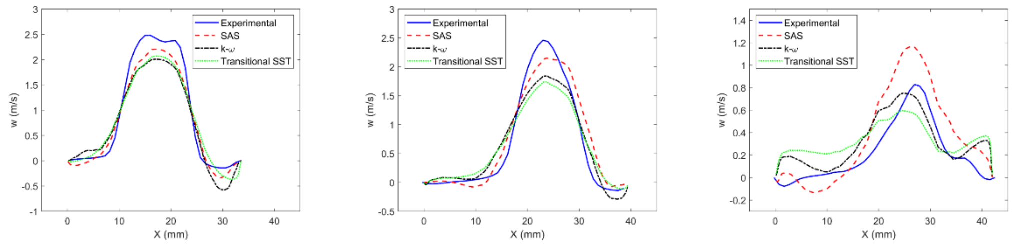

b) Profile along the x axis

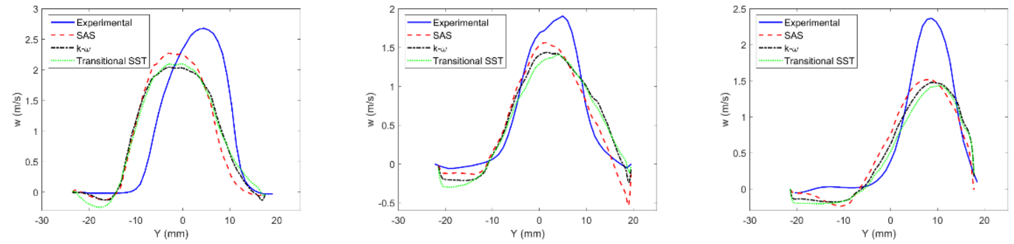

c) Profile along the y axis

Figure 4.3 – w velocity profiles along the x and y axes for Planes 1-3.

Analyzing the qualitative results, it can also be said that all three numerical results were very close to each other, mainly in y direction at all planes, where it is possible to observe a geometric correspondence in all cases, regarding the location of the jet. It is important to emphasize that there is some uncertainty about the precise location of the local x and y axes used in the experiments and numerical model, due to the data interpolation process to obtain a precise correspondence in terms of the location of each axis (numerical and experimental). However, with respect to the z-velocity component, it can be said that the prediction of SAS model was closer to the experimental data than the other two models.

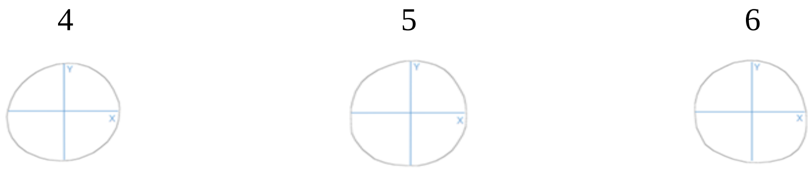

a) Reference planes

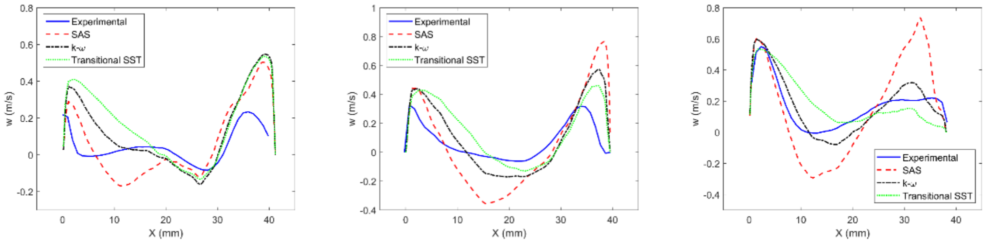

b) Profile along the x axis

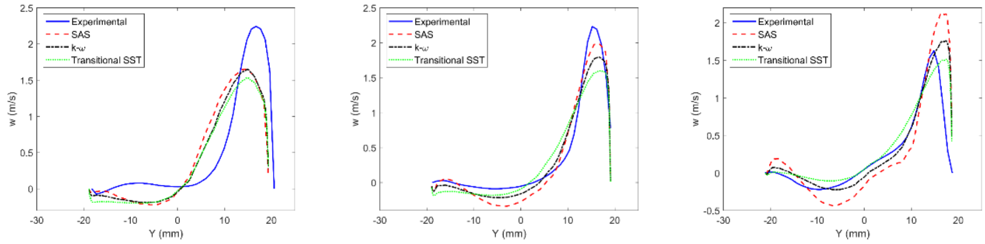

c) Profile along the y axis

Figure 4.4 - w velocity profiles along the x and y axes for planes 4-6.

4.2 Velocity components in the transversal planes ($\boldsymbol{u}$ & $\boldsymbol{v}$)

To complete the evaluation of the prediction of the velocity field with all three turbulence models, both velocity components in the transversal plane (x-component

u and y-component v) are examined in this section.

Figure 4.5 shows the comparison of the turbulence models and experimental data of the contours for the $x-$velocity component u and $y-$velocity component v. Due to the inclination of the planes in relation to the inlet jet (Figure 4.1), the x-component is smaller and the y-component is like the z-component (Figure 4.2). Once again, similar results were predicted by all models, with a greater similarity between $\kappa - \omega$ SST and Transition SST. As already mentioned, since the flow is steady, there is no transition, therefore, fully turbulent flow is predicted by all models.

Good agreement was obtained of all models with the experimental data, for the y-velocity component, with a slightly superior result of SAS model, since it presented higher velocities than the other two models, closer to the experimental values. Also, due to the smaller velocities, larger differences between the numerical and experimental data are seen for the x-velocity component, although it is possible to observe similarities among the results, like the location and size of regions with positive and negative values.

Besides the contours, it was possible to plot the values for u and v velocities components for six planes along the x and y axis. Figure 4.6 shows these results for the $x-$velocity component u in all planes, while Figure 4.7 presents the profiles for $y-$velocity component v.

Analyzing the $x-$velocity component u profiles in Figure 4.6 along the y axis, a good adherence to the numerical predictions with the experimental data is observed, with a larger discrepancy along the x-axis, but with the correct trends, i.e., with a reasonable prediction of the reverse flow direction, except for Plane 4. Better agreement is seen along the y-direction, with a small superiority of SAS prediction.

Figure 4.7 shows better agreement, for the y-velocity component v, between the three turbulence models and the experimental data, indicating that the models were able to capture the reverse direction of the flow, although larger peak velocities were measured

The larger disagreement between prediction and models, can be attributed to small differences in the location of the center of the inlet jet, which can anticipate and delay the position of velocity reverse flow.

All models are similar among themselves, with greater similarity between the two SST models (traditional and transitional). Further, as already mentioned, better agreement is seen for the y-velocity component, with a better representation with the SAS model.

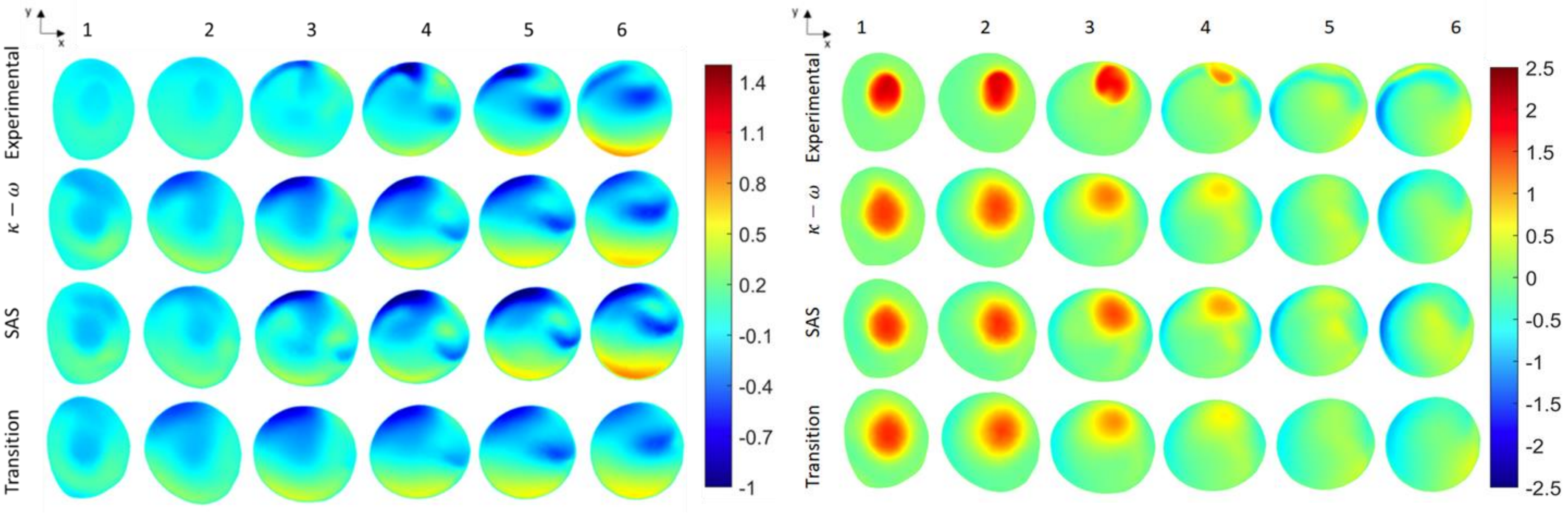

a) x-velocity component, u b) y-velocity component, v

Figure 4.5 – Transversal planes with velocities x and y components contours

a) Reference Planes

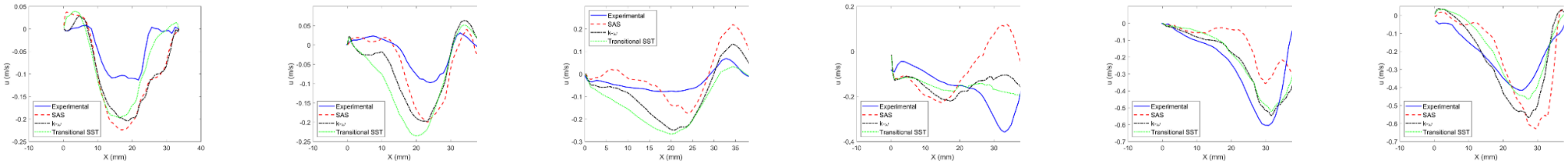

b) Profile along the x axis

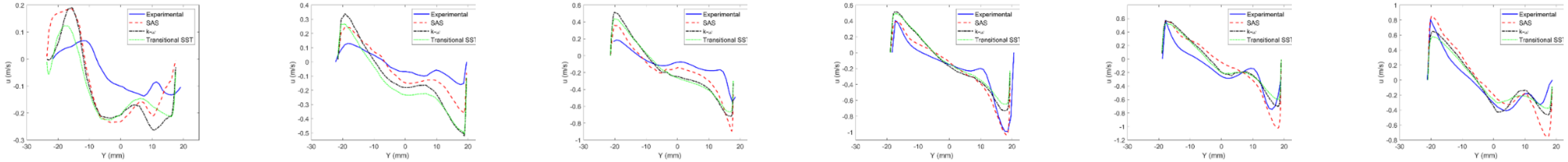

c) Profile along the y axis

Figure 4.6 - $x-$velocity component u profiles along the x and y axes for planes 1-6.

a) Reference Planes

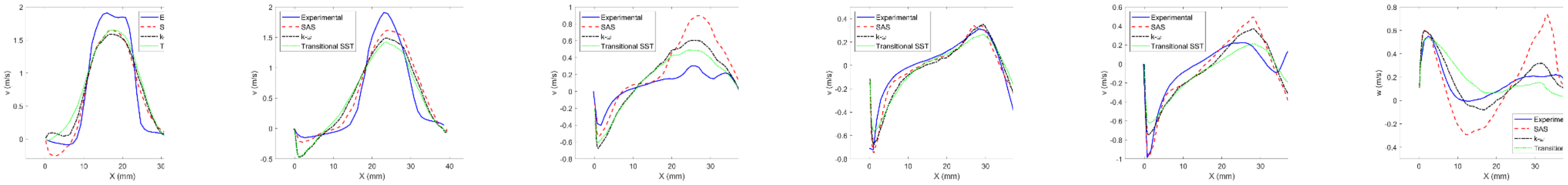

b) Profile along the x axis

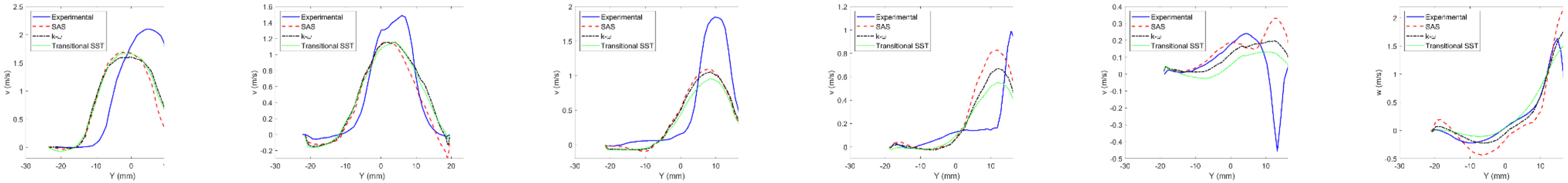

c) Profile along the y axis

Figure 4.7 - y velocity component v profiles along the x and y axes for planes 1-6.

4.3 Turbulent Kinetic Energy (κ)

The turbulent kinetic energy contour in the six planes is examined in Figure 4.8, which shows the experiment data and the prediction of the three tested turbulence models.

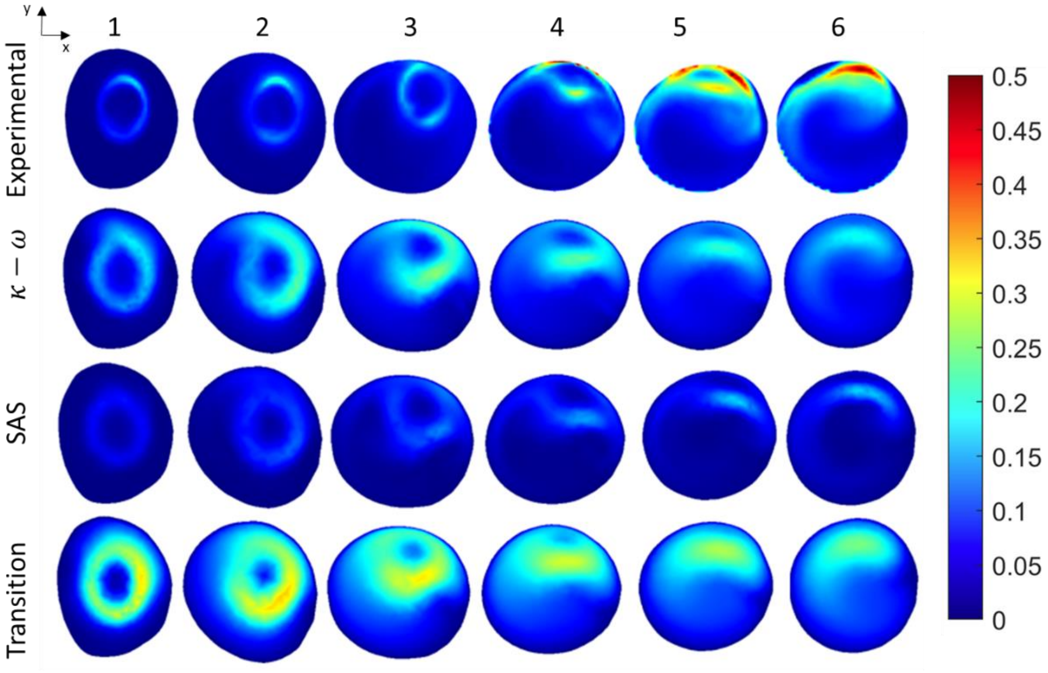

Figure 4.8 -Contours of turbulent kinetic energy κ (m^2/s^2)

Observing the contours, it is seen similar κ levels between the experimental measurements and SAS prediction in the lower planes (Planes 1 – 3), where both SST models, over-estimate κ values, especially the Transitional SST. On the other hand, for the planes further apart from the entrance (Planes 4 – 6), both SST models results presented a closer agreement with the experimental data then SAS model.

However, qualitatively the numerical results had a reasonable relationship with the experimental results, i.e., the highest value of κ occurs around the inlet jet, at the lower planes. For planes further apart from the inlet, since the jet´s center moves closer to the aortic wall, due to the aorta curvature, κ increases near the wall regions.

As a result, based on the κ results and the discussion, it is still not possible to determine which turbulence model best approximated the experimental result.

4.4 Tangential Components of the Reynolds Stress Tensor

To completely evaluate the Reynolds stress tensor, the tangential components $\overline{u'v'}$, $\overline{u'w'}$ e $\overline{v'w'}$ predicted by the three turbulence models and the experimental data are presented in Figure 4.9 to Figure 4.11 at all six planes.

As expected, based on the previous results, both SST once again presented very similar results among themselves for the three components, with higher values than predicted by SAS in the first planes.

SAS model predicted a similar $\overline{u'v'}$ distribution to the experimental data for the three first planes, but it did not capture the increase in its intensity near the impinging region at the upper planes (Figure 4.9). Although the SST models predicted an increase in $\overline{u'v'}$ at the upper planes, its distribution was not satisfactory.

By examining Figure 4.10 and Figure 4.11, one can conclude that no model was able to adequately predict the shear Reynolds stress components $\overline{u'w'}$ and $\overline{v'w'}$.

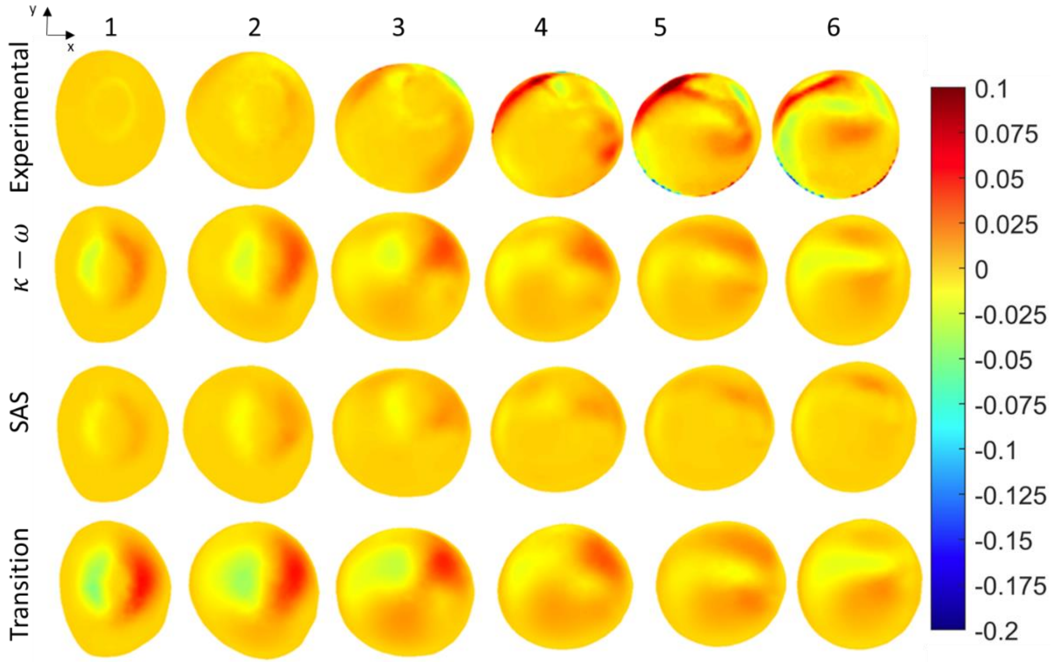

Figure 4.9 – $\overline{u'v'}$ (m^2/s^2) contours at the six planes.

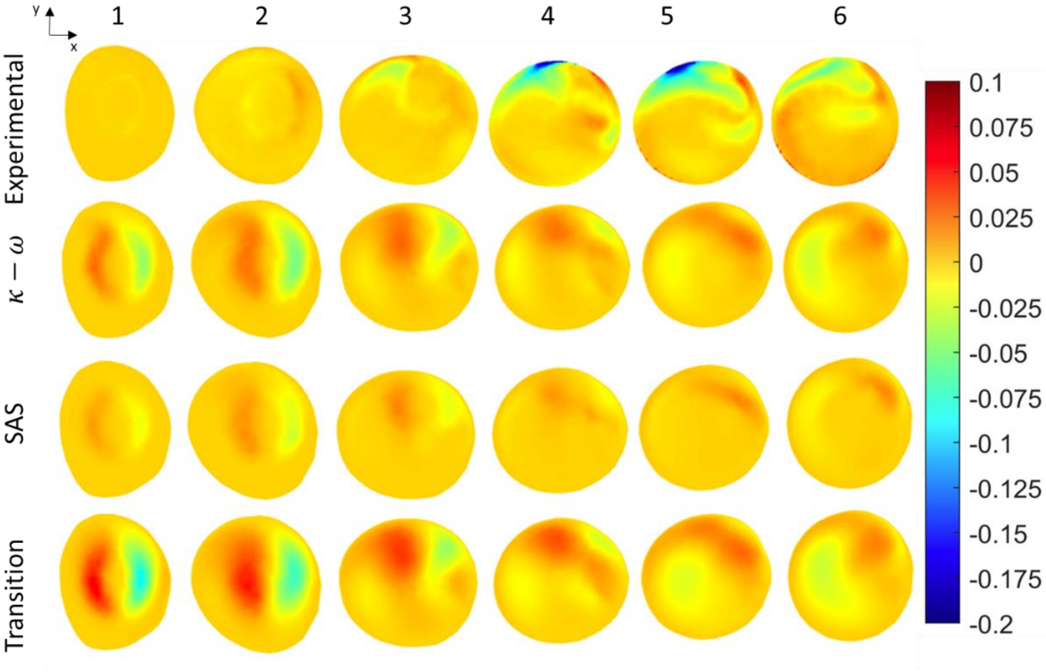

Figure 4.10 – $\overline{u'w'}$ (m²/s²) contours at the six planes.

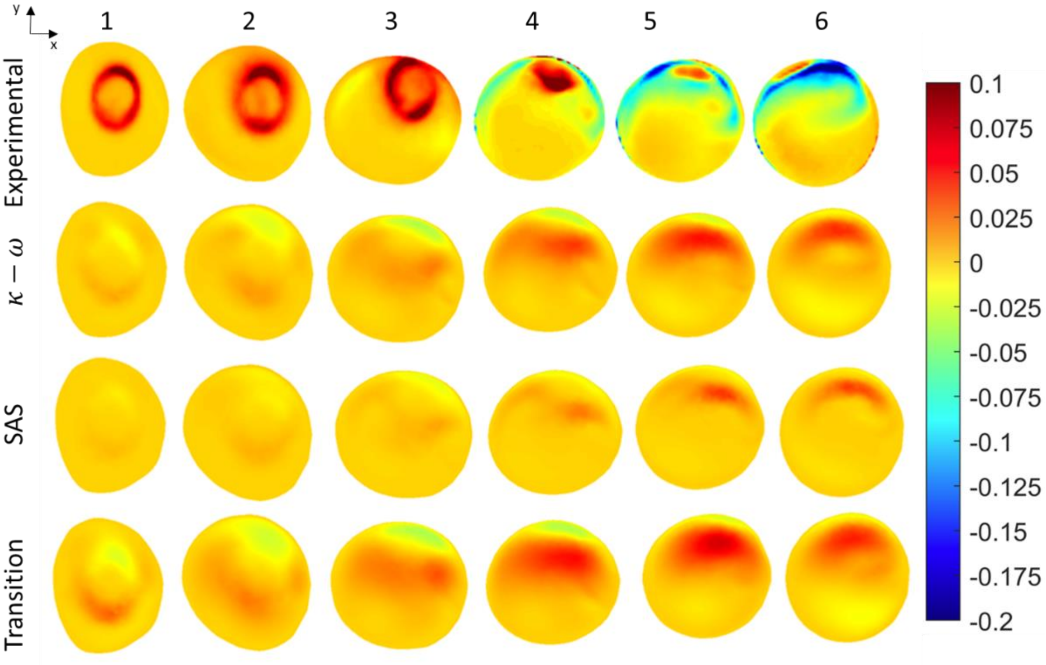

Figure 4.11 – $\overline{v'w'}$ (m²/s²) contours at the six planes.

4.5 Complementary analysis of the turbulence models results

From the analysis of the velocity components, turbulent kinetic energy, and tangential components of the Reynolds Stress, the best model that came closest to the experimental result could not be qualified. Aiming to explore the identification of the position of the peak of the z-velocity component (w) was addressed. To this end, a straight line was created passing through the point of maximum value of the z-velocity component and the centroid for each of the six selected planes.

Figure 4.12 illustrates these lines created for all turbulence models at all six planes and Table 4.1 show the measured angles between each model's line and the experimental line. Line blue refers to the experimental data, whilst lines red, black and green refers to the SAS, $\kappa - \omega$ and Transitional SST numerical lines, respectively Analyzing these values, the portion of maximum w velocity of all numerical data is shifted in the same direction in relation to the experimental data, with a deviation smaller than $\sim 10^{\circ}$. Some models present a larger deviation than others in some planes and other models in subsequent planes. The measured deviation obtained in Plane 1 is clearly wrong, since as seen in Figure 4.2, the iso-contour lines of w are almost concentric and all models present similar result as the experimental data. The reason is due to the uncertainty of defining the center of maximum velocity. Since it is too close to the centroid position, very small changes can lead to significant angles differences.

Table 4.1 – Deviation of line between maximum w velocity and centroid

Model	**Plane 1**	**Plane 2**	**Plane 3**
κ-ω SST	81.87°	5.71°	13.24°
Transition SST	63.45°	2.98°	7.12°
SAS SST	90°	2.98°	10.30°
	Plane 4	**Plane 5**	**Plane 6**
κ-ω SST	7.08°	5.14°	2.00°
Transition SST	0.64°	0.50°	5.78°
SAS SST	4.79°	0.00	8.80°

The z-velocity component profiles along these lines were determined for each model in the six planes and are plotted in Figure 4.13. Figure 4.14 shows the w velocity profile along the lines orthogonal to the centroid-maximum w lines, shown in Figure 4.12. Once again, all turbulence model prediction were very close to each other, particularly in the first three planes. Furthermore, it is possible to identify a similarity in the location of the jet for all six planes. In planes 1-3, the $\kappa - \omega$ SST model outperformed the other two because its higher velocities values allowed it to match the experimental data. SAS and Transition SST had a slightly better agreement with the experimental data in Planes 4-6, because those had lower velocity values that approximated to the experimental profile. Overall, with respect to the z-velocity component along the lines that passes through the point of maximum value of w, it can be said that no model was closer to the experimental data than the other two models. Figure 4.14 shows that in the first two planes, all models are very close to each other, as is the location of the jet. As they approached the experimental data in planes 1 and 2, the $\kappa - \omega$ and SAS models stood out. The SAS model differed significantly from the other models in the upper planes, indicating that it was unable to predict well the values of w along these lines. When analyzing the profiles of w along the orthogonal lines (Figure 4.14), it was not possible to clearly identify which model $\kappa - \omega$ SST or Transition SST stood out in the upper planes, making it difficult to pinpoint the best turbulence model.

To complement the present analysis, the maximum, minimum and average value of each velocity component and turbulent quantities predicted by each model at each of the six planes are shown in

Table 4.2 through Table 4.5, where a significant deviation between all models can be seen, alternating variable and plane, where one particular property is better predicted. At the appendix the mean relative and absolute error of each variable in relation to the experimental data at each plane is also listed. From the present comparison, it was not possible to identify a superiority in the prediction of any model. This conclusion is similar to the one presented by Tan *et al.* (2008), who also could not identify which model is superior in the prediction of the turbulent flow.

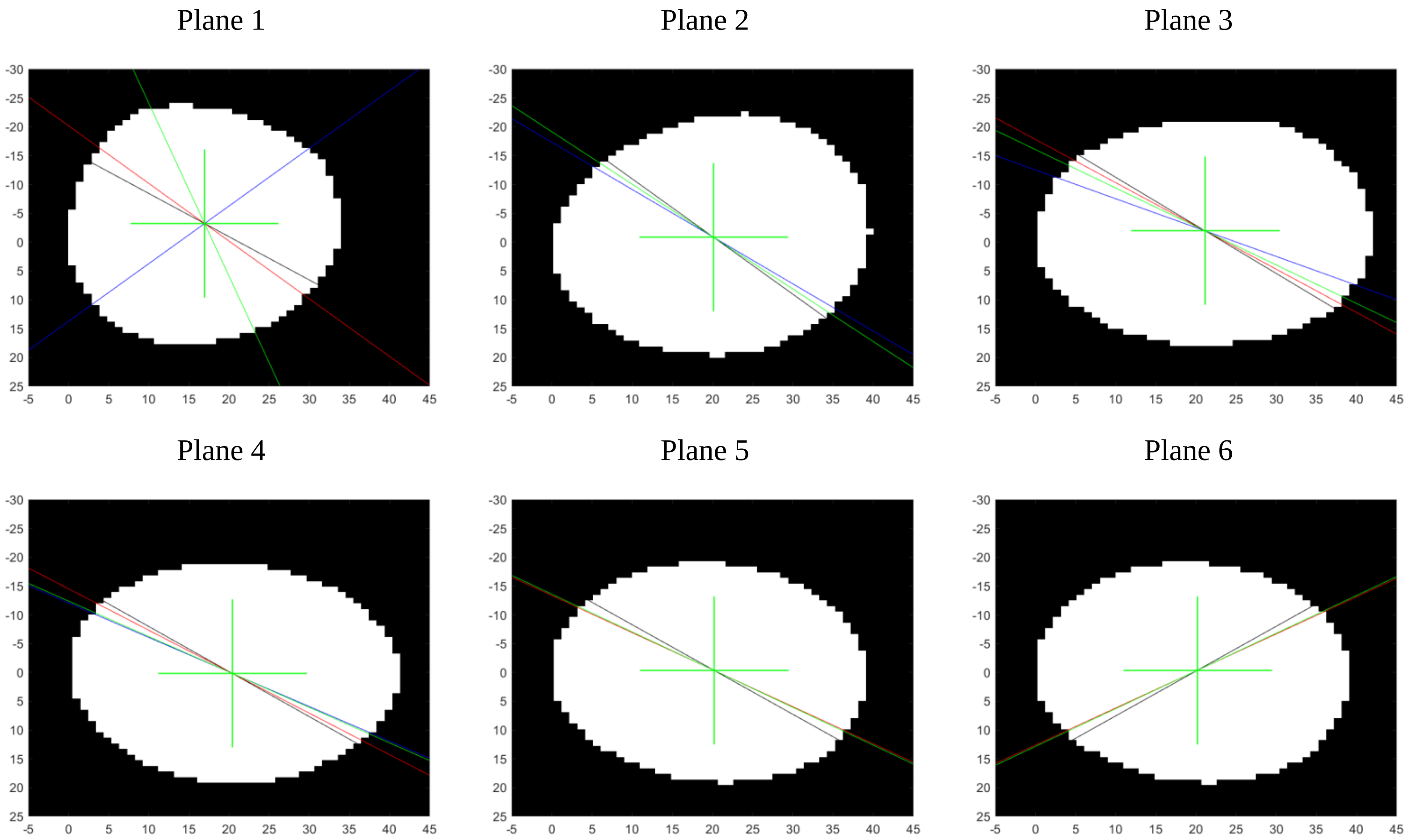

Figure 4.12 – Lines from plane centroid and maximum w position, for all six planes and turbulence models.

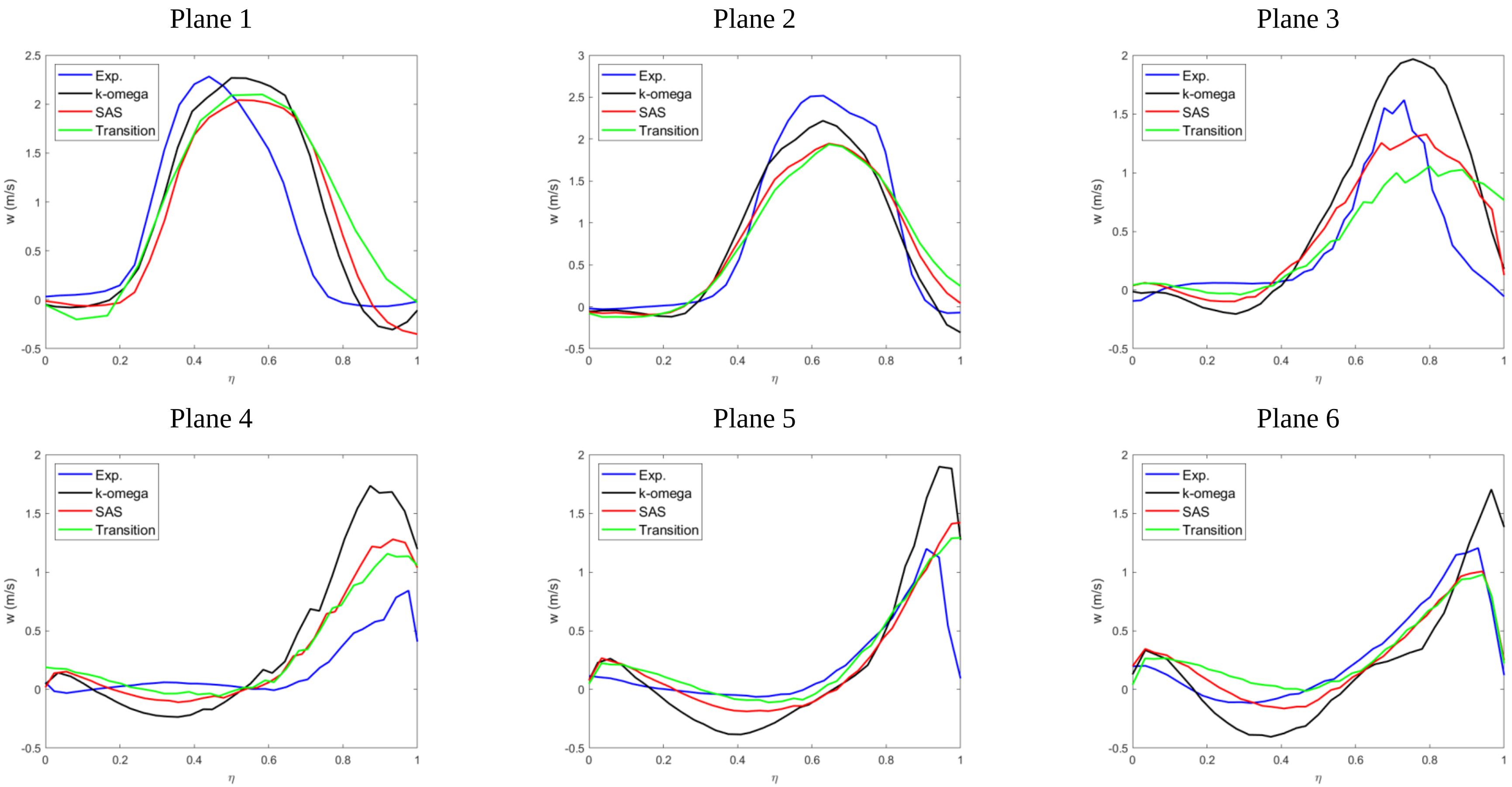

Figure 4.13 – *w* component velocity profiles along the lines of maximum and centroid for planes 1-6.

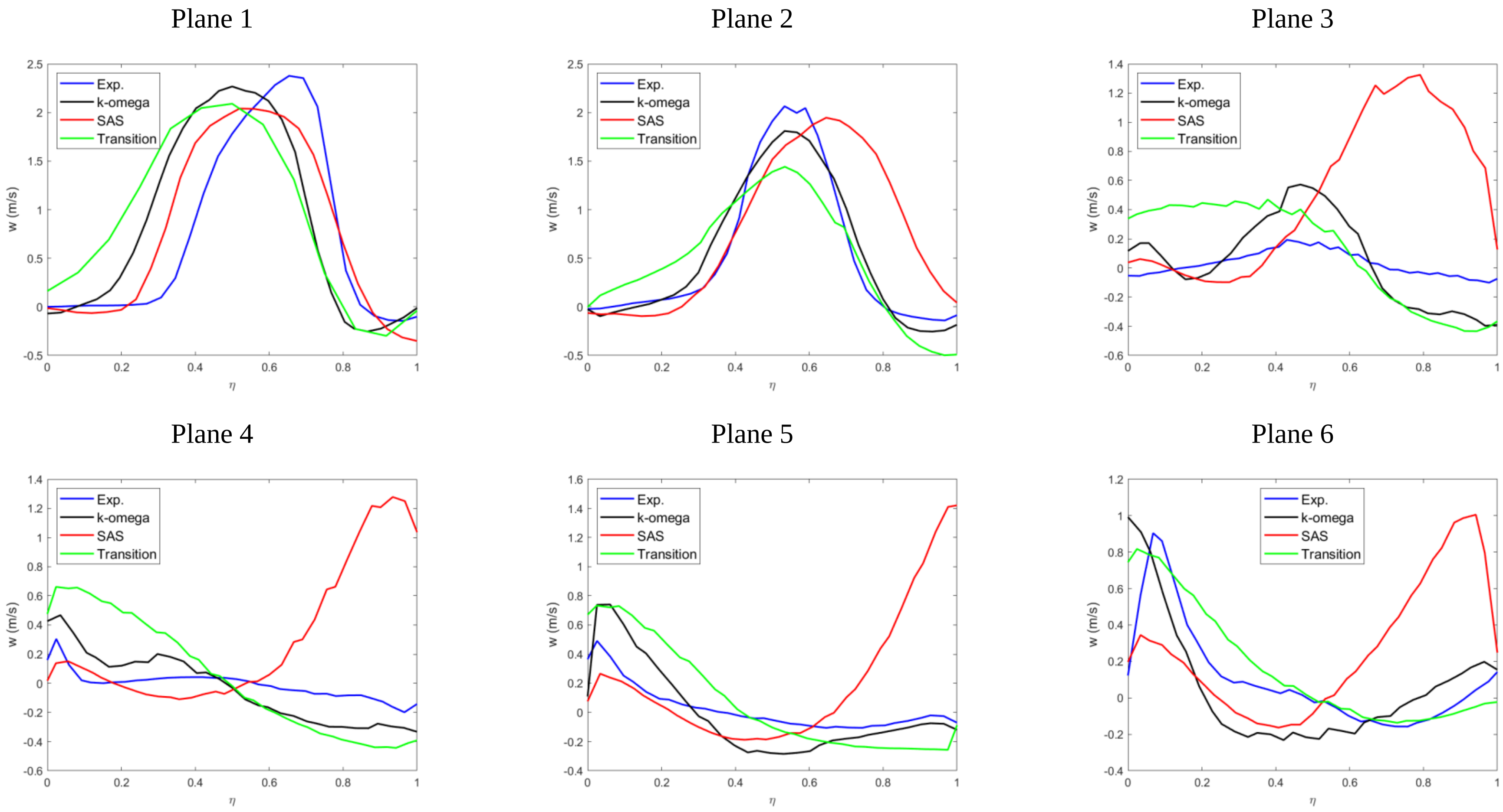

Figure 4.14 – *w* component velocity profiles along the lines orthogonal to the lines of maximum and centroid for planes 1-6.

Table 4.2 – Velocity and turbulent kinetic energy data for planes 1-3.

		Plane 1				**Plane 2**				**Plane 3**			
		Experimental	**SAS**	$\kappa-\omega$	**Transitional**	**Experimental**	**SAS**	$\kappa-\omega$	**Transitional**	**Experimental**	**SAS**	$\kappa-\omega$	**Transitional**
max	u	0.0699	0.2418	0.2470	0.1537	0.1307	0.2588	0.3406	0.2843	0.3336	0.3733	0.5172	0.4513
	v	2.1076	1.6896	1.6000	1.6724	2.0643	1.6624	1.5694	1.5883	1.9302	1.5196	1.2841	1.1659
	w	2.6783	2.2714	2.0412	2.0989	2.5713	2.2181	1.9494	1.9435	2.4848	2.1366	1.8500	1.7473
mean	u	-0.0209	-0.0127	-0.0354	-0.0268	-0.0018	-0.0076	-0.0335	-0.0568	-0.0264	-0.0417	-0.0405	-0.0578
	v	0.3111	0.2300	0.3070	0.3111	0.2589	0.1930	0.1760	0.1686	0.2563	0.1054	0.0589	0.0488
	w	0.3111	0.2643	0.2616	0.2559	0.2589	0.2258	0.2248	0.2343	0.2563	0.2680	0.2872	0.2937
min	u	-0.1392	-0.2346	-0.2658	-0.2335	-0.1606	-0.3726	-0.5911	-0.5478	-0.5625	-1.0571	-0.9278	-0.7944
	v	-0.1481	-0.2608	-0.1027	-0.1494	-0.1529	-0.3261	-0.5062	-0.4834	-0.1579	-0.5720	-0.6622	-0.5920
	w	-0.1481	-0.3491	-0.5694	-0.5421	-0.1529	-0.5565	-0.5310	-0.5310	-0.1579	-0.3967	-0.4575	-0.4827
max	κ	0.1903	0.0694	0.1806	0.3241	0.2202	0.1090	0.2304	0.3348	0.2094	0.1279	0.2542	0.3211
mean	κ	0.0106	0.0153	0.0478	0.0967	0.0190	0.0295	0.0736	0.1200	0.0282	0.0341	0.0836	0.1208

Table 4.3– Velocity and turbulent kinetic energy data for planes 4-6.

		Plane 1				Plane 2				Plane 3			
		Experi-mental	**SAS**	$\kappa-\omega$	**Transi-tional**	**Experi-mental**	**SAS**	$\kappa-\omega$	**Transi-tional**	**Experi-mental**	**SAS**	$\kappa-\omega$	**Transi-tional**
max	u	0.4067	0.4219	0.5184	0.4875	0.6155	0.6050	0.5618	0.5282	0.8184	0.8614	0.6479	0.5749
	v	1.2421	1.0772	0.8026	0.6620	0.5339	0.4933	0.3716	0.3361	0.7604	0.4299	0.4729	0.4511
	w	2.5423	2.2150	1.9358	1.7674	2.4606	2.3574	1.9790	1.7603	1.8675	2.3119	1.8532	1.5909
mean	u	-0.0844	-0.1078	-0.0836	-0.0757	-0.0944	-0.0758	-0.0727	-0.0684	-0.0102	0.0079	-0.0045	-0.0036
	v	0.2822	-0.0146	-0.0328	-0.0267	0.3075	-0.1217	-0.1108	-0.1104	0.2756	-0.2082	-0.1878	-0.1973
	w	0.2822	0.3404	0.3469	0.3483	0.3075	0.3908	0.3780	0.3676	0.2756	0.3735	0.3575	0.3449
min	u	-1.2112	-1.2807	-0.9453	-0.7854	-1.0584	-1.3129	-0.9056	-0.7373	-0.5768	-1.0057	-0.6195	-0.5203
	v	-0.2153	-0.8476	-0.7154	-0.5841	-0.1251	-1.0215	-0.7554	-0.6218	-0.2369	-1.4343	-1.0271	-0.8500
	w	-0.2153	-0.3558	-0.4105	-0.4511	-0.1251	-0.3864	-0.2243	-0.2684	-0.2369	-0.4473	-0.2275	-0.1533
max	κ	1.3763	0.1418	0.2349	0.2922	0.5719	0.1638	0.2116	0.2720	0.4928	0.1681	0.1928	0.2460
mean	κ	0.0566	0.0327	0.0806	0.1134	0.0780	0.0313	0.0781	0.1089	0.0704	0.0317	0.0758	0.0987

Table 4.4 – Reynolds stress components data for planes 1-3.

		Plane 1				Plane 2				Plane 3			
		Experimental	**SAS**	$\kappa - \omega$	**Transitional**	**Experimental**	**SAS**	$\kappa - \omega$	**Transitional**	**Experimental**	**SAS**	$\kappa - \omega$	**Transitional**
R12	**max**	0.0025	0.0099	0.0265	0.0585	0.0100	0.0186	0.0388	0.0579	0.0488	0.0194	0.0409	0.0516
	mean	-0.0003	0.0000	0.0009	0.0029	-0.0004	0.0006	0.0018	0.0014	0.0002	0.0009	0.0020	0.0022
R23	**max**	0.1458	0.0069	0.0120	0.0324	0.1749	0.0093	0.0162	0.0253	0.1488	0.0122	0.0249	0.0382
	mean	0.0057	0.0000	0.0000	0.0007	0.0085	0.0001	0.0001	0.0020	0.0083	-0.0001	0.0021	0.0052
R13	**max**	0.0058	0.0157	0.0306	0.0635	0.0161	0.0197	0.0285	0.0573	0.0298	0.0224	0.0319	0.0462
	mean	0.0057	0.0000	0.0000	0.0007	0.0085	0.0001	0.0001	0.0020	0.0083	-0.0001	0.0021	0.0052
R11	**max**	0.0150	0.0472	0.1209	0.2022	0.0420	0.0663	0.1424	0.2069	0.2289	0.0784	0.1462	0.1891
	mean	0.0023	0.0102	0.0318	0.0642	0.0058	0.0194	0.0481	0.0795	0.0118	0.0219	0.0540	0.0789
R22	**max**	0.2756	0.0669	0.1677	0.2521	0.3097	0.0837	0.1994	0.2427	0.2682	0.1115	0.2130	0.2169
	mean	0.0132	0.0106	0.0340	0.0653	0.0187	0.0204	0.0500	0.0775	0.0254	0.0228	0.0541	0.0765
R33	**max**	0.1020	0.0559	0.1293	0.2921	0.1190	0.1064	0.2147	0.3298	0.1281	0.1192	0.2540	0.3201
	mean	0.0057	0.0097	0.0299	0.0637	0.0136	0.0191	0.0493	0.0830	0.0192	0.0235	0.0592	0.0862

Table 4.5 – Reynolds stress components data for planes 4-6.

		Plane 1				Plane 2				Plane 3			
		Experi-mental	**SAS**	$\kappa-\omega$	**Transi-tional**	**Experi-mental**	**SAS**	$\kappa-\omega$	**Transi-tional**	**Experi-mental**	**SAS**	$\kappa-\omega$	**Transi-tional**
R12	**max**	0.1069	0.0157	0.0332	0.0366	0.1745	0.0179	0.0239	0.0233	0.2607	0.0186	0.0154	0.0197
	mean	0.0029	0.0009	0.0023	0.0036	0.0036	0.0011	0.0024	0.0033	0.0013	-0.0001	-0.0014	-0.0013
R23	**max**	0.9435	0.0261	0.0466	0.0603	0.0806	0.0452	0.0583	0.0746	0.1261	0.0452	0.0499	0.0535
	mean	0.0012	0.0014	0.0058	0.0105	-0.0200	0.0029	0.0076	0.0116	-0.0183	0.0022	0.0040	0.0057
R13	**max**	0.0860	0.0163	0.0276	0.0386	0.0632	0.0220	0.0281	0.0315	0.0895	0.0203	0.0244	0.0238
	mean	0.0012	0.0014	0.0058	0.0105	-0.0200	0.0029	0.0076	0.0116	-0.0183	0.0022	0.0040	0.0057
R11	**max**	0.3222	0.0913	0.1413	0.1760	0.4834	0.1097	0.1326	0.1679	0.7360	0.1101	0.1235	0.1560
	mean	0.0211	0.0209	0.0516	0.0727	0.0318	0.0203	0.0505	0.0711	0.0324	0.0207	0.0507	0.0669
R22	**max**	0.7927	0.0786	0.1495	0.1740	0.7126	0.0956	0.1358	0.1800	0.6767	0.1362	0.1629	0.2040
	mean	0.0470	0.0215	0.0530	0.0739	0.0701	0.0212	0.0543	0.0754	0.0676	0.0231	0.0560	0.0737
R33	**max**	1.9374	0.1355	0.2134	0.2647	0.6320	0.1271	0.1569	0.1992	0.4815	0.0969	0.1076	0.1397
	mean	0.0450	0.0230	0.0566	0.0803	0.0541	0.0210	0.0514	0.0713	0.0408	0.0195	0.0448	0.0568

4.6 Conclusion

The comparison of the prediction of $\kappa - \omega$ SST, Transitional SST and SAS turbulence model with experimental data obtained in the same configurations, for steady state conditions did not indicate a clear superiority of one model in relation to the other.

Since during the cardiac cycle, there are transition from laminar to turbulent regime, models that capture the transition are welcome. Further, due to the slight better agreement obtained with the SAS model, this model was selected for further investigations of the cardiac cycle.

5 CARDIAC CYCLE ANALYSIS

This chapter presents an analysis of the blood flow inside the ascending aorta during the cardiac cycle. The impact of employing a turbulence model that incorporates transition modeling is addressed. Based on the analysis presented in Chapter 4, the transition model SAS-SST was selected, coupled with the intermittence variable, to better predict the transition flow regime during the cardiac cycle.

The aortic model chosen for the study is based on the studies developed by Ibanez (2019) and Ibanez et al. (2020), who evaluated the blood flow in a transient regime with and without fluid-structure interaction. The model is basically the same as in Chapter 4, but without the 1 m extension at the inlet, as shown in Figure 5.1. The aortic valve was considered as a circular orifice. In the present analysis, the actual blood properties were defined as: Density $\rho = 1054$ kg/m³ and dynamic viscosity μ = 0.0035 Pa. s (Gao *et al.*, 2006).

The prediction of the transition model SAS-SST is compared with the results of Ibanez et al. (2020), who employed the $\kappa - \omega$ SST model, neglecting compliance of the aorta structure, since this effect was not include in the present model.

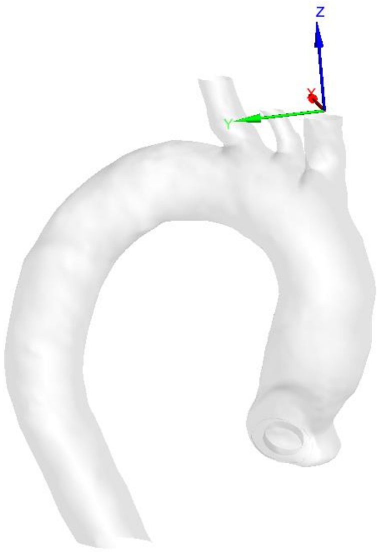

Figure 5.1 – Aorta and coordinate axis origin

To visualize the internal velocity fields and evaluate the results qualitatively and quantitatively, a plane perpendicular to the inlet was created. (Figure 5.2 a) Furthermore, three planes were created parallel to the brachiocephalic artery ($x-y$ plane) where the system's origin is defined. The first plane is located 124 mm below the origin, similarly, the other planes are located 94 mm and 74 mm below the coordinate axis origin and parallel to $x-y$ plane, respectively. Additionally, a region of interest was defined in the aorta, precisely where the jet impacts the aortic wall, which is the region where there is a greater chance for the development of an aneurysm because of the blood impact. Figure 5.2 illustrates the aorta with all the planes mentioned, as well as the region of interest.

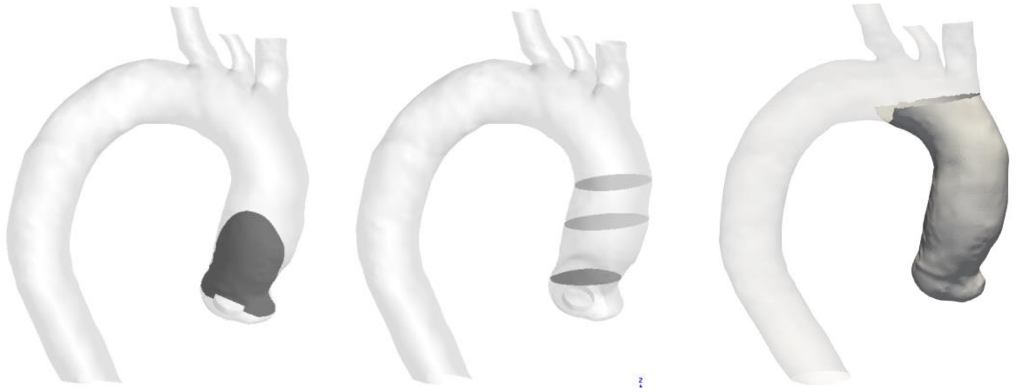

a)Plane perpendicular to inlet b) Planes parallel to $x-y$ plane c) Region of interest

Figure 5.2 - Planes and region of interest

5.1 Case studies

To represent different patients with different heart beats, two different boundary conditions were considerate:

- Case 1: refers to the boundary conditions employed by Ibanez (2019) and Ibanez et al. (2020), corresponding to a cycle with period of 1 s.
- Case 2: refer to the boundary conditions employed here, based on the work of Johnson *et al.* (2020), considering a cardiac cycle with 0.86 s of duration.

The boundary conditions selected for this study are based on physiological pressure and mass flow rate profiles. At the inlet, pressure profiles were defined while for the four outlets in the aorta, total flow rate profiles were imposed, and percentage of the total flow rate at each outlet was defined based on recommendation of Alastruey *et al*. (2016), and employed by Ibanez (2019). These values are shown in Figure 5.3: Descending aorta (output 1 – 69.1%), brachiocephalic artery (output 2 – 19.3%), left carotid artery (output 3 - 5.2%) and left subclavian artery (output 4 – 6.4%). The origin is located on Output 1, where the z-component is perpendicular to its plane, as seen in Figure 5.1.

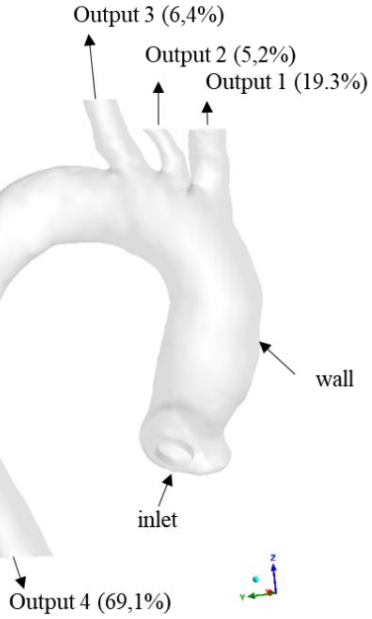

Figure 5.3 - Percentages of blood flow

5.1.1 Inlet boundary conditions

The pressure profile at the inlet of Case 1 was developed by Ibanez (2019), based on Crosetto *et al.* (2011) and Reymond *et al.* (2013). It is illustrated in Figure 5.4, and described by:

$$p_{in}(Pa) = 10^3(10,8 - 37,4\,t + 837\,t^2 - 3952\,t^3 + 7643\,t^4 - 6642\,t^5 + 2151\,t^6) \quad (5.1)$$

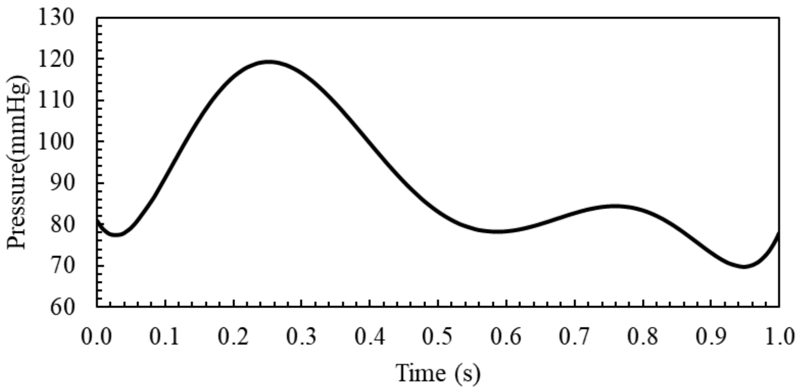

Figure 5.4 – Case 1 inlet pressure profile. Ibanez (2019).

Case 2 corresponds to the pressure profile, $p_{in}(t)$, proposed here, based on the work of Johnson *et al.* (2020), whose the cardiac cycle has a duration of 0.86 s. The profile is described by the eight-degree Fourier Series equation using MATLAB as an auxiliary.

$$F = a_0 + \sum_{i=1}^{n} a_i \cos(i\,\alpha\,x) + b_i \sin(i\,\alpha\,x) \tag{5.2}$$

where a_0 models a constant (intercept) term in the data and is associated with the $i = 0$ cosine term, α is the fundamental frequency of the signal, n is the number of terms (harmonics) in the series, and $1 \leq n \leq 8$. The constant values for the Fourier series with 8 terms are shown in Table 5.1.

To evaluate how well the chosen model fits the data. the following quantities were evaluated: Sum of Squares Error, SSE=2.053; Root Mean Squared Error, RMSE=0.325 and Coefficient of Determination, $R^2 = 0.997$. The small values of SSE and RMSE and R^2 closer to 1 indicate a good fit. Thus, the values obtained indicate that a good fit was achieved. The graph of the adjusted Fourier equation is shown in Figure 5.5.

Table 5.1 – Case 2 - constant values for the Fourier Series for pressure profile.

Fourier Coefficients for pressure profile	
a0	13140
a1	-769.1
b1	673.9
a2	-1351
b2	-378.3
a3	720.2
b3	-595.1
a4	-129
b4	141.7
a5	211.7
b5	-1.87
a6	-44.73
b6	40.77
a7	24.14
b7	9.378
a8	-21.14

b8	44.78
w	7.546

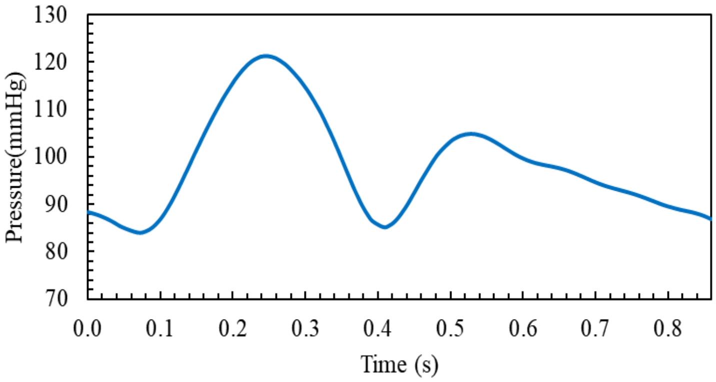

Figure 5.5 - Case 2 inlet pressure profile, based on Johnson *et al.* (2020).

5.1.2 Outlet boundary conditions

For Case 1, the total mass flow rate profile imposed by Ibanez (2019) is given by Eq. (5.3), and it is shown in Figure 5.6.

$$\dot{m}_{ref} = 56.6\,t^6 - 150.8\,t^5 + 132.9\,t^4 - 33.2\,t^3 - 9.8\,t^2 + 4{,}4\,t - 0{,}05 \qquad (5.3)$$

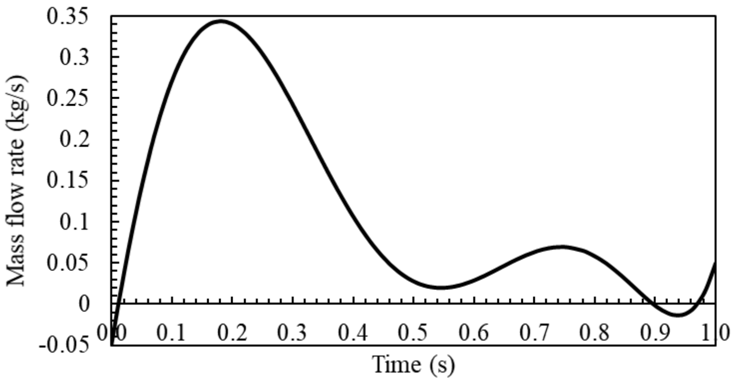

Figure 5.6 – Case 1 mass flow rate profile during cardiac cycle

The total mass flow rate proposed here, for Case 2, was based on the work of Lo *et al.* (2019), who presented the total volumetric flow rate. Using the density value employed in here, it was possible to obtain the total mass flow rate. Also, the maximum mass flow rate value was adjusted in order to match as close as possible the value from Ibanez *et al.* (2020). To develop and adjusted profile, the same process used for the pressure was used here, so an eight-degree Fourier Series equation was developed using MATLAB as an auxiliary. The constant values for the Fourier series with 8 terms are shown in Table 5.2. The quality parameters related to the adjustments are SSE=0.00150; RMSE=0.004 and R^2 =0.9996, indicating the good quality of the fit. The total mass flow rate profile can be visualized in Figure 5.7.

Table 5.2 – Case 2 - constants values for the Fourier Series for the mass flow rate profile

Fourier Coefficients for mass flow rate	
a0	0.08517
a1	-0.03443
b1	0.132
a2	-0.0636
b2	-0.02072
a3	-0.01201
b3	-0.02751
a4	0.01919
b4	-0.01905
a5	0.007674
b5	0.009546
a6	-0.0006092
b6	0.002094
a7	-0.001467
b7	-0.000723
a8	0.002205
b8	-0.000094
w	7.149

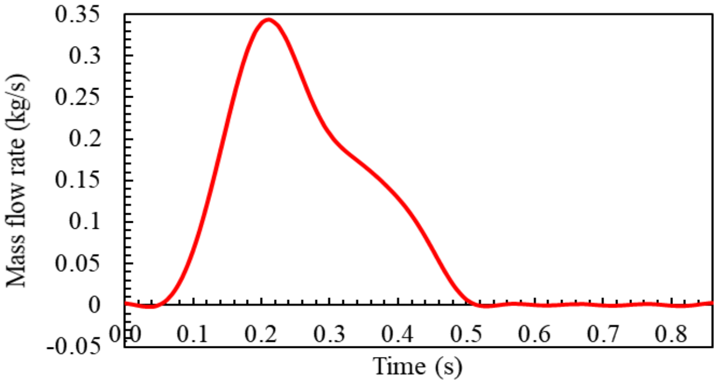

Figure 5.7 - Case 2 mass flow rate during cardiac cycle.

5.1.3 Flow regime

According to Pope, flow through pipes is classified into three main flow regimes:

i. Laminar - $Re < 2000$
ii. Transitional - $4000 > Re > 2000$
iii. Turbulent - $Re > 4000$

To evaluate the flow regime during the cardiac cycle, the inlet Reynolds number was determined. Since the flow is incompressible, the total mass flow rate profiles for Case 1 and Case 2 were employed. Figure 5.8 is produced by using Equation (3.1), blood characteristics, and the aorta diameter D. Note that the maximum Reynolds number at the inlet is approximately 8000, corresponding to turbulent regime.

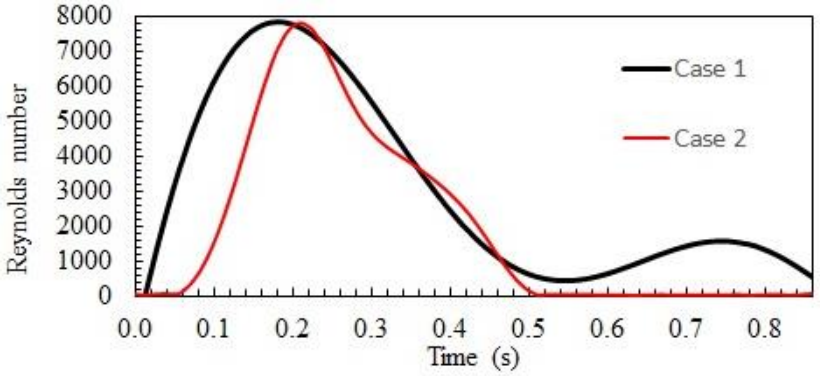

Figure 5.8 – Inlet Reynolds number.

The aorta's diameter is larger than the valve diameter (which, here is approximated as a constant and equal to the maximum patient valve opening of 16 mm). Further, the diameter of the aorta varies along its length, increasing in the ascending and decreasing in the descending regions. Thus, to estimate the Reynolds number inside the aorta, the aorta was considered as a circular pipe, and a mean diameter of the aorta equal 38.8 mm was employed. The mean aortic Reynolds number is shown in Figure 5.9, with maximum value near 3300.

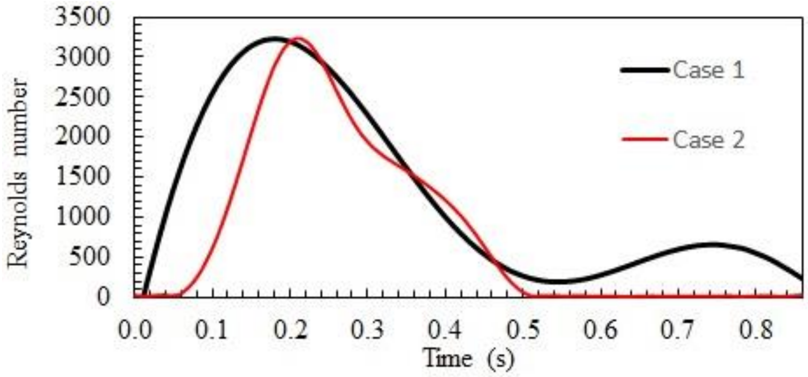

Figure 5.9 – Average Reynolds number.

Analyzing both Figure 5.8 and Figure 5.9, it can be observed that during the period of systole, the regime is turbulent at the entrance of the aorta, passing to the transition from 0.35 s onwards and remaining in the laminar regime during the remainder of the cardiac cycle. Examining Figure 5.9, it is observed that the average Reynolds value did not exceed 3300, indicating that the flow in the interior of the aorta is in the transitional regime during systole and laminar in the diastole, indicating the need of employing a turbulence model able to model the transition of regimes.

5.2 Periodic regime

Before analyzing the flow variable for the different cases, it is necessary to guarantee that a periodic regime has been numerically attained. To this end, time average values of wall pressure (TAP) and wall shear stress (TAWSS) during the cardiac cycle, Eqs. (3.85) and (3.86), were determined during different cycles, at the region of interest (Figure 5.2c). Case 1 was selected for this test with the SAS SST model.

The data of the first two cycles was discarded and the averages values of the third cycle, average of the third combined with fourth cycle and finally the average from the third to the fifth cycle were determined. These results are shown in Table 5.3. It can be seen practically identical results for the time average wall pressure and wall shear stress from the third cycle on.

To better evaluated the difference, the ratio each of these values and the three cycles average were determined and they are shown in Table 5.4 and plotted in Figure 5.10. It is possible to conclude that the number of cycles for calculating the average quantities did not impact the TAP values. On the other hand, for the average and maximum values of TAWSS, the number of cycles slightly impacted the values. Thus, for the analysis of the results, the fifth cycle was considered, and all mean values were calculated with data from the three last cardiac cycles.

Table 5.3 - TAWSS and TAP for using 1, 2 and 3 cycles

	TAWSS (Pa)			**TAP (mmHg)**		
	3° cycle	**3° and 4° cycle**	**3° to 5° cycle**	**3° cycle**	**3° and 4° cycle**	**3° to 5° cycle**
Minimum	0.02	0.02	0.02	88.47	88.38	88.44
Average	1.75	1.74	1.76	88.86	88.80	88.85
Maximum	5.16	5.31	5.34	89.59	89.52	89.59

Table 5.4 - Ratio of TAWSS and TAP

	Ratio of TAWSS (Pa)			**TAP (mmHg)**		
	Minimum	**Average**	**Maximum**	**Minimum**	**Average**	**Maximum**
1 cycle	1.00	0.99	0.97	1.00	1.00	1.00
2 cycles	1.00	0.98	0.99	1.00	1.00	1.00

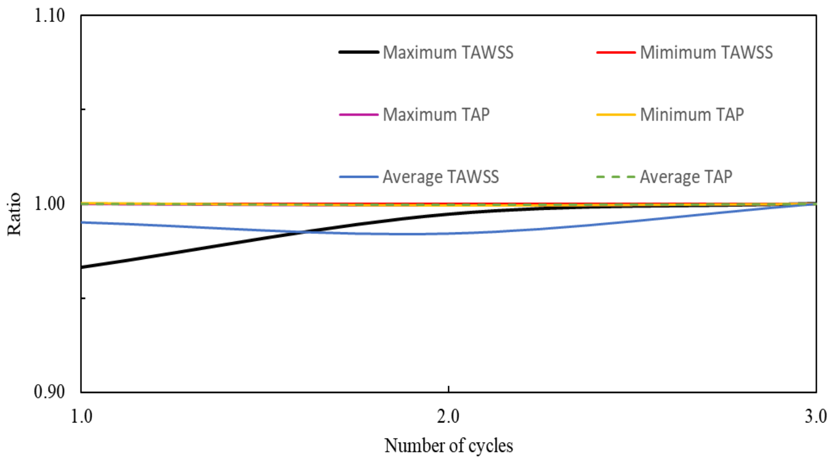

Figure 5.10 - Ratio of TAWSS and TAP determined with 1, 2 cycles in relation to 3 cycles.

5.3 Impact of turbulent model during cardiac cycle

In the previous chapter, the transition models did not present a superior prediction of the flow field variables when compared with experimental data, for steady state condition at the systole peak. However, as it was shown in section 5.1.3, during the cardiac cycle, the flow inside the aorta is in the transitional regime. Thus, in this section, the prediction of the flow variables with the selected transitional model SAS SST, with intermittency coupling, is compared with the prediction of the $\kappa - \omega$ SST, obtained with Ibanez (2019), for Case 1.

To assess the impact of the turbulence model on hemodynamic patterns during the cardiac cycle, the following strategies were used:

i. Initially, the effects of turbulence models at different moments of the cardiac cycle were analyzed, through this way it was possible to identify aspects of hemodynamic patterns in terms of turbulence models in specific points of the cardiac cycle: beginning of systole period; maximum mass flow point in the systolic period; ending of systole period; beginning of diastolic period; middle of diastolic period and ending of diastolic period.
ii. Aiming to identify general behaviors during the cardiac cycle, analyzes of temporal averages of quantities of interest were performed: $TAWSS$; TAP and OSI.

5.3.1 Flow variables at the systole peak

To begin the evaluation of the impact of the turbulence models in flow variables, the time instant corresponding to the systole peak, as illustrated in Figure 5.11, was chosen.

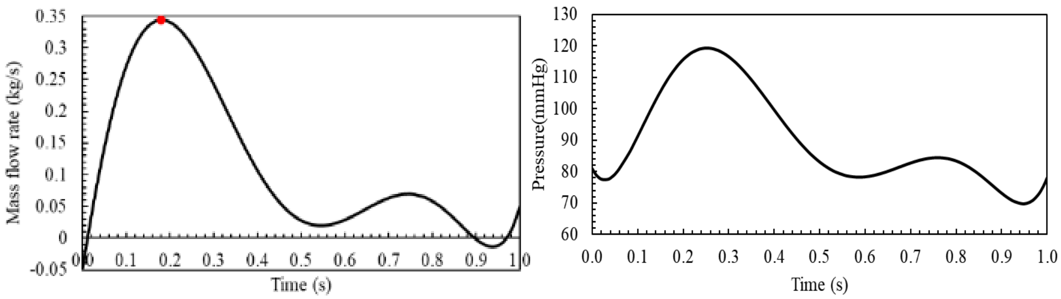

Figure 5.11 –Cardiac cycle flow rate and pressure. Case 1. Indication of time instant of systole peak (t=0.18s).

In Figure 5.12, the iso-contours of the magnitude of the velocity vector are illustrated at the central plane indicted in Figure 5.2a. Qualitatively the flow predicted by both turbulence models are similar. The inlet jet entering the aorta through the valve (circular orifice) can be clearly seen. As the jet enters the domain, with velocity V_{in}= 1.65 m/s, it is decelerated and diffused, presenting a widening of its diameter. As the jet approaches the aortic wall, a stronger deceleration can be observed. Around the jet, very low velocities can be observed, specially near the aortic root, where a flow reverse flow occurs, due to the expansion of the domain, since the aorta has a larger diameter than the inlet valve. Quantitatively, the average and maximum values of the velocity magnitude, in this central plane, in both cases were equivalent, indicating that the turbulence model had little impact on these results. This is expected, since at systole peak, the inlet flow is turbulent.

To complement the analysis, the iso-contours of the velocity vector magnitude were plotted along the transverse planes (shown in Figure 5.2b), to allow the evaluating of the jet evolution, as we move along the ascending aorta region. In Figure 5.13, it is possible to observe once again a great similarity in the two cases. At Plane 1, the circular central jet can be seen, and as one advances in the ascending region, the maximum values shift to the wall region due to the aorta´s curvature, as seen in Plane 2. In the last plane, after the impact of the jet with the aortic wall, the blood slows down, resulting in lower velocity values. Only in this plane is it possible to identify a region with slightly higher values for the $\kappa - \omega$ case, as seen by the yellow region, close to the wall.

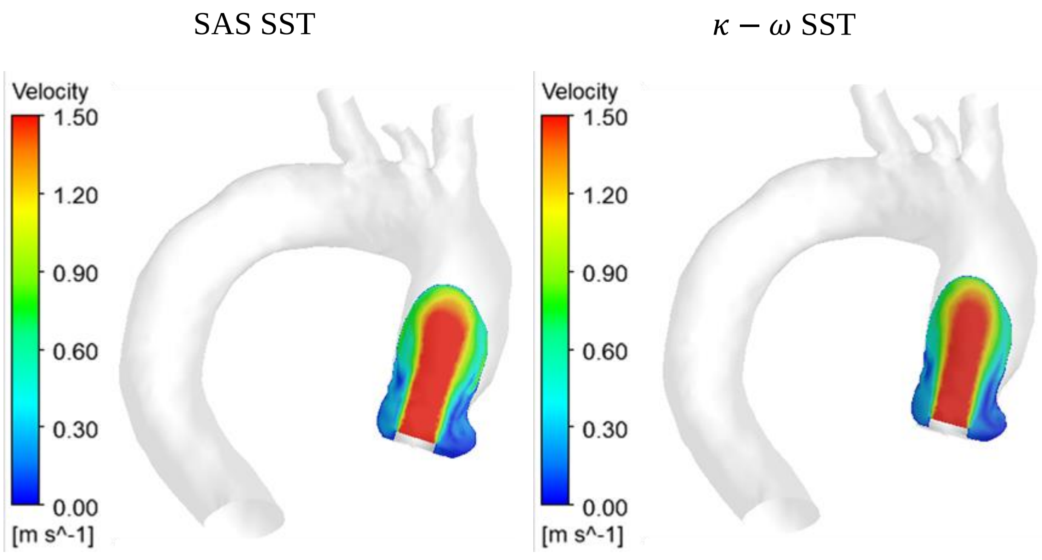

$|\vec{V}|_{mean}$=1.02 m/s $|\vec{V}|_{max}$=1.78 m/s $|\vec{V}|_{mean}$=1.00 m/s $|\vec{V}|_{max}$=1.75 m/s

Figure 5.12 – Turbulence models impact on the velocity vector magnitude on central plane perpendicular to the inlet at the systolic peak. Case 1

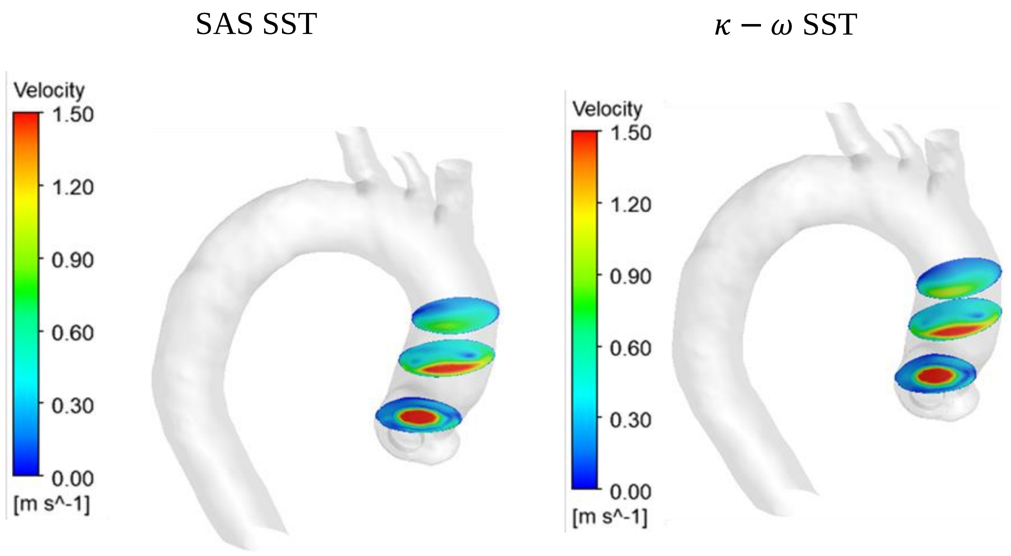

SAS SST

$\kappa - \omega$ SST

Figure 5.13 – Turbulence models impact on the velocity vector magnitude on transversal planes at the systolic peak. Case 1

Figure 5.14 illustrates streamlines, and a z-component velocity iso-surface, corresponding to $w = 0.5$ m/s obtained with the SAS SST and $\kappa - \omega$ SST turbulence models. Both variables are colored with the magnitude of the velocity vector. The iso-surface visualization is an intuitive way of visualizing the behavior of the blood jet that enters the aorta, and the streamlines illustrates the flow development along the aorta. Looking at Figure 5.14, the path taken by the blood inside the aorta is very similar for both models of turbulence. The iso-surface with a value of w = 0.5 m/s, indicates that values equal to or greater than 0.5 m/s are present inside the surface. In both cases, the iso-surface is similar, with the $\kappa - \omega$ SST model presenting a slightly wider region around the jet with velocity w = 0.5 m/s. The jet impacted the surface of the aorta at nearby points in both cases. At the point of maximum flow, the velocity field is maximum in the central region up to the point that impacts the wall, from then on it tends to spread inside the aorta until the moment it impacts the aortic wall, creating recirculation in the ascending aorta region. For the $\kappa - \omega$ SST turbulence model, larger recirculation is present, being located mainly in the aortic root region. In general, the results are in line with what was seen in Figure 5.12 and Figure 5.13.

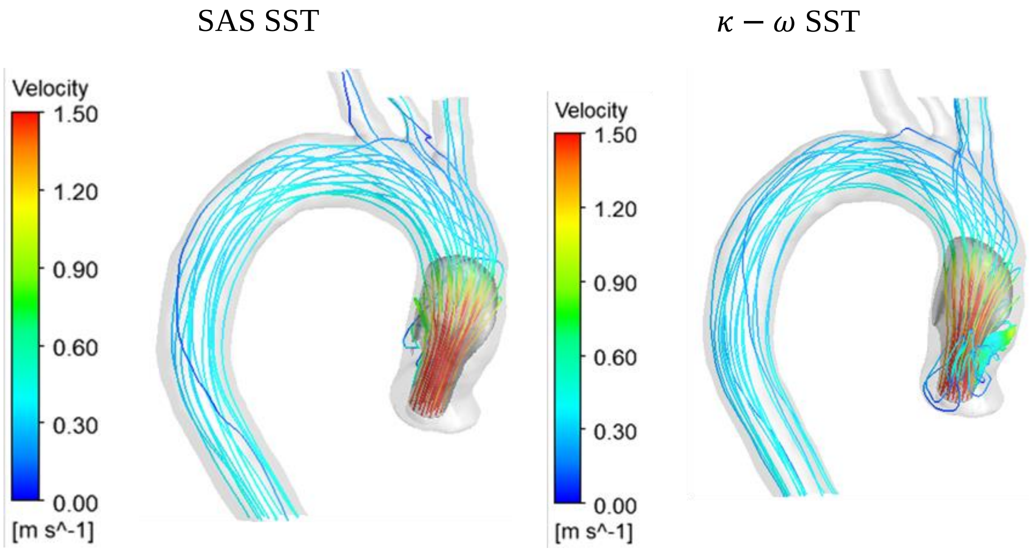

Figure 5.14 – Turbulence models impact on streamlines and iso-surface of the z-velocity component (w=0.5 m/s). Case 1

The results of the pressure field and shear stress field on the wall (Eq. 3.79), at the critical condition of maximum flow is presented in Figure 5.15 and Figure 5.16, respectively. Such quantities are fundamental to the health of a human being, and they can help in medical diagnosis, per example it can aid in identify the impact of the growth of aneurysms in the ascending aorta (Almeida *et al.*, 2021).

Figure 5.15 shows the pressure contours for Case 1, varying the turbulence model. It is noticeable that even in a transient situation, at the systole peak, there are great qualitative and quantitative similarity with both model’s prediction. Both the mean and maximum wall pressure values were identical. The lowest pressure occurs in the wall region close to the aortic root (mean pressure values are in the order of 100-103 mmHg). At the jet impact region, high pressure can be observed, decaying along the flow direction, as expected due to flow friction.

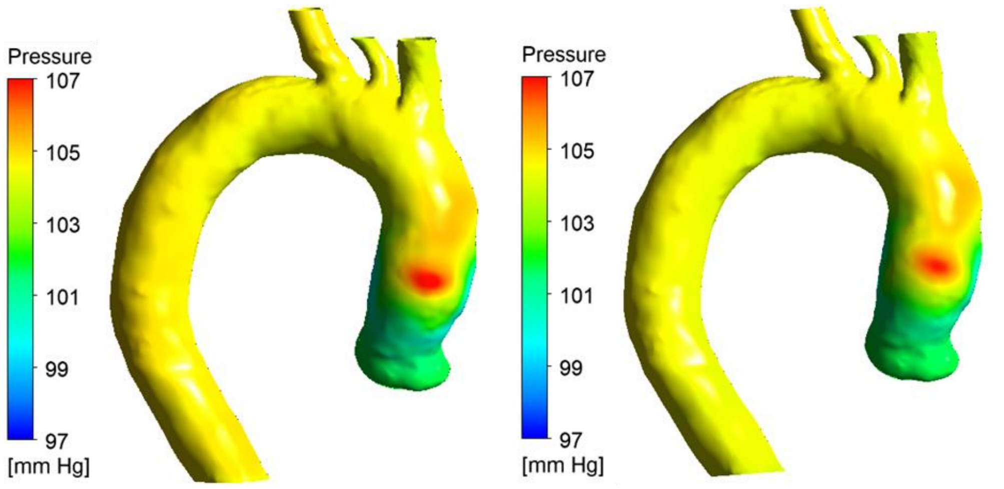

SAS SST $\kappa - \omega$ SST

P_{mean}=104 mmHg P_{max}=107 mmHg P_{mean}=104 mmHg P_{max}=107 mmHg

Figure 5.15 – Turbulence models impact on pressure contours at the systolic peak. Case 1

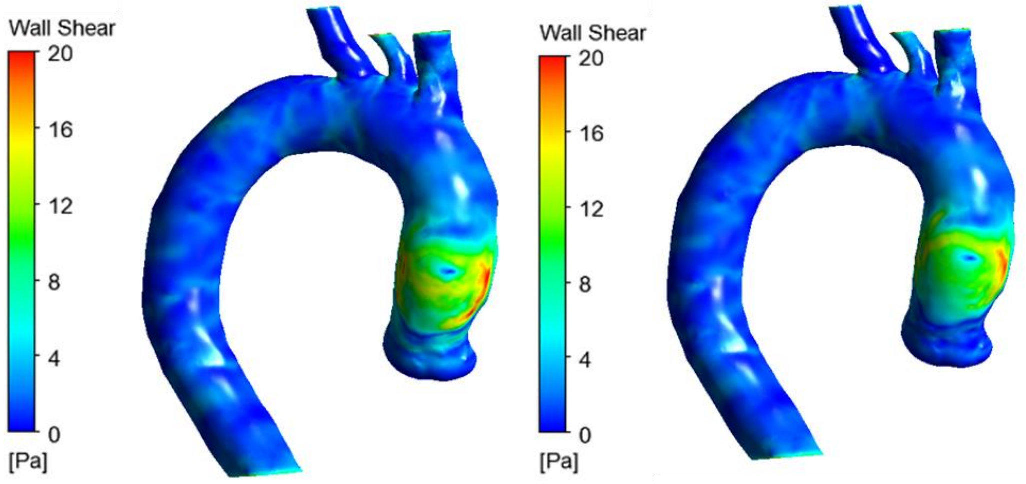

SAS SST $\kappa - \omega$ SST

SST_{mean}=2.18 Pa SST_{max}=73.41 Pa SST_{mean}=2.03 Pa SST_{max}=74.39 Pa

Figure 5.16 – Turbulence models impact on WSS contours at systolic peak. Case 1

Examining the wall shear stress distribution in Figure 5.16, obtained at systole peak, with both SAS-SST and $\kappa - \omega$ SST models, it is possible to see that qualitatively, both distributions are similar, with the highest values in the region of the ascending aorta, close to the region where the blood jet impacts the wall, and the flow must change direction to flow along the curvature of the aorta. For this variable a slight difference can be observed, SAS-SST model presents a smaller maximum WSS, but since the area with higher values is larger, high mean WSS was obtained.

Turbulent kinetic energy can be associated with the characteristic eddies' velocity, since in depends on the velocity fluctuations of all three directions (Eq. 3.9). Its distribution obtained with both models is illustrated over the streamline in Figure 5.17. Since turbulent kinetic energy is generated in the region of high shear, it is possible to observe that the highest values of κ occur around the inlet jet. For this variable, the model's selection presented an impact. Lower value of κ were obtained with the transitional SAS SST model ($\approx$ 0.015 m^2/s^2) than with the $\kappa - \omega$ SST model ($\approx$ 0.025 m^2/s^2). Although this result corresponds to the systole peak, the since the $\kappa - \omega$ model considered the entire flow as turbulent, large turbulence generation were obtained in the previous time instants, reflecting at the systole peak, while for the SAS SST model, with intermittency, transition is modeled and the turbulence is damped, when inertia is reduced along the flow.

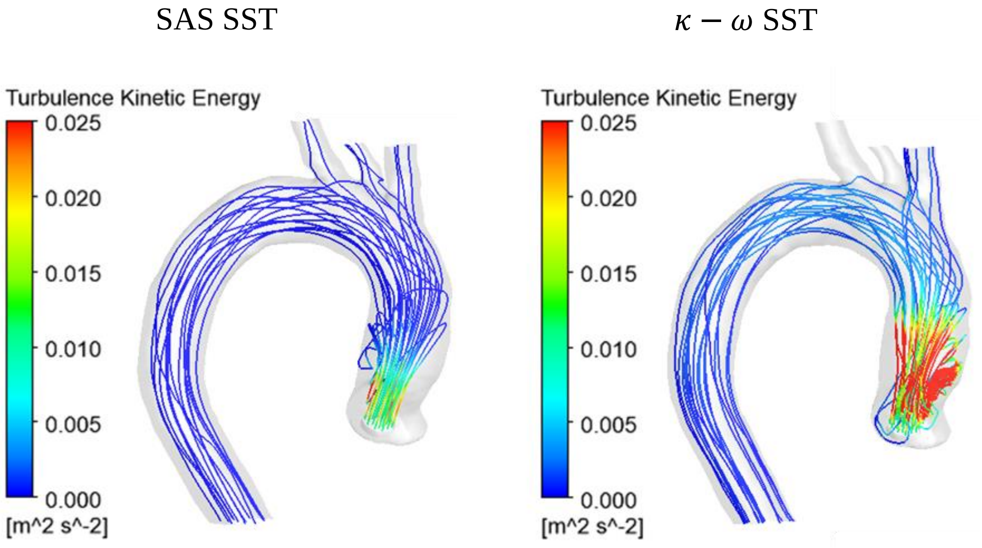
SAS SST

$\kappa - \omega$ SST

Figure 5.17 – Turbulence models impact on streamlines colored by turbulent kinetic energy at systole peak. Case 1.

Next, the Q criterion (Eq. 3.82) distribution is examined. This variable can help to identify coherent structures of the flow and vortices within the aorta. A positive value of Q means that the vorticity magnitude outweighs the strain rate. The objective of this analysis is to visualize the coherent structures and mainly the impacts of the turbulence model and boundary condition on it. Together with the Q-criterion, another important quantity is the normalized helicity normalized H (Eq. 3.83). The helicity measures the degree of connectivity between the flow's vortex lines and assesses the tendency of the flow to produce coherent vortices. Normalized helicity may help in the identification of valvar and heart problems since the helical flow may induce aortic dilatation. The vortex core, which is characterized by intense vortex winding, is represented by normalized helicity, ranging from -1.0 to 1.0. According to Levy *et al.* (1990) normalized helicity can be used to determine how the velocity vector field is oriented in relation to the vorticity vector field for a given flow field, since the normalized helicity is the cosine of the angle between the velocity and vorticity vectors. For example, the velocity and vorticity vectors tend to align parallel to each other at the center of streamwise vortices observed behind ground vehicles, ships, aerodynamic bodies at incidence, and in many other flows. As a result, the normalized helicity value at the core of the streamwise vortices will be very close to 1.0 or -1.0. This fact is used to pinpoint the center of those streamwise vortices. Yet, when velocity and vorticity vectors are parallel, the normalized helicity is exactly equal to unity and the streamline is locally straight. Therefore, the normalized helicity goes to its maximum value on a streamline of minimum curvature.

Figure 5.18 shows the Q criterion iso-surface traced with a value equal to 3.500 s^{-2}, colored by the normalized helicity, ranging from -1.0 to 1.0. This Q value was chosen until a hairpin-shaped structure was found, as interpreted by (Almeida *et al.*, 2019), it can have a correlation with growth of aortic aneurysms.

Analyzing Figure 5.18, it is possible to notice a big difference between the turbulence model's prediction. For the $\kappa - \omega$ SST model, the hairpin structure is better defined, while for the SAS SST model, the coherent structures are more like longitudinal ligaments. Note positive and negative H around each arm of the hairpin, in the $\kappa - \omega$ SST model result, indicating different rotation direction around each side. Also note the same sign of H around the two longitudinal coherent structures predicted by the SAS SST, indicating the same rotation direction around the structure. Analyzing the helicity, predicted by both models, the highest values of helicity are exactly located in regions of lesser curvature of the ascending aorta. The smallest values of helicity, on the other hand, are in the regions of greater curvature of the current lines, indicating that the vorticity and velocity are in opposite directions.

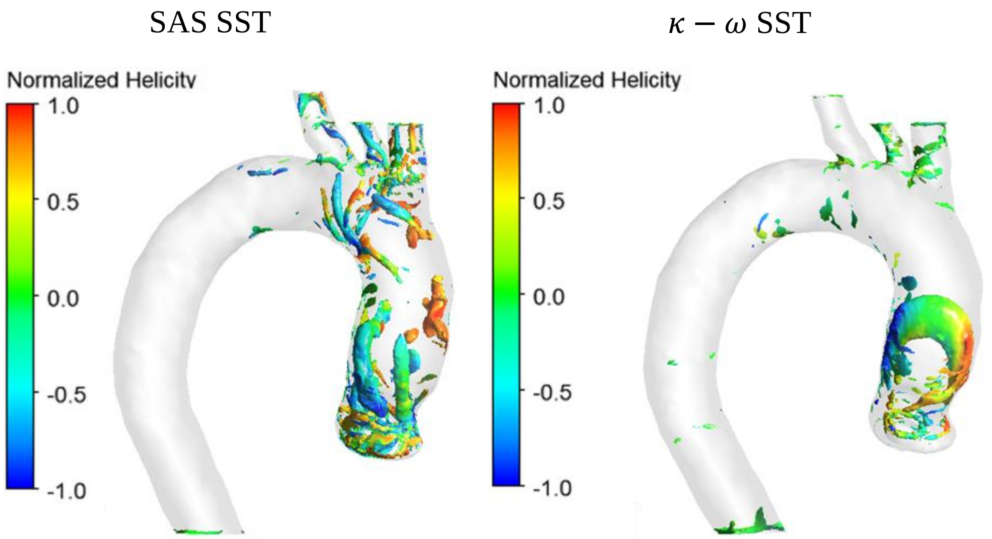
SAS SST

$\kappa - \omega$ SST

Figure 5.18 – Turbulence models impact in Q - criterion colored by normalized helicity at systole peak. Case 1.

5.3.2 Flow variables along the cardiac cycle

In this sub-section, the flow variables are analyzed at different time instants along the cardiac cycle. Three points were selected during systole and three points during diastole of the cardiac cycle. These time instants are shown Figure 5.19.

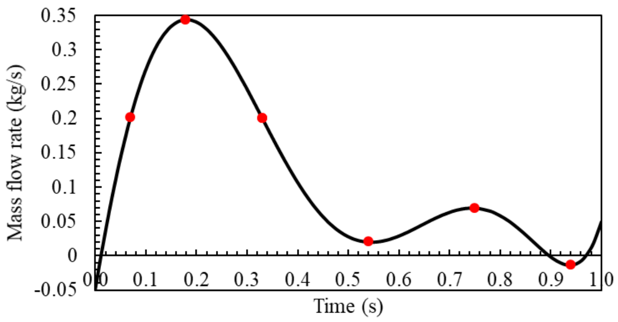

Figure 5.19 - Selected points to evaluate the cardiac cycle. Case 1.

At the first- and third-time instants, flow rate is the same, but at the first point, the fluid is accelerating, while at the other, equivalent to one third of the cycle, the fluid is being decelerated. For the rest of the points, the minimum and maximum points of diastole were selected.

Figure 5.20 illustrate the evolution of the magnitude of the velocity vector in the central plane in the six-time instants selected for Case 1. The comparison was made using the same scale and including the selected points and instants.

Analyzing Figure 5.20, it is possible to see similar behavior was predicted by both turbulence models, i.e., increase of the velocity and subsequent reduction after the systole peak. Higher velocities are observed at the decelerating period (t=0.33s), although the flow rate is the same at t = 0.07s. It can also be clearly seen the significant velocity reduction of the diastole period. Since the same velocity scale was selected, no difference between model's prediction can be observed during the diastole. Note however that, the transitional model SAS-SST predicts slightly smaller levels of velocity during the decelerating period than the $\kappa - \omega$ SST model.

Iso-surfaces of w = 0.5 m/s and streamlines are plotted colored by the velocity magnitude, obtained with each model can be visualized in Figure 5.21, along the cardiac cycle. It is worth mentioning again that within the iso-surface, the velocity values are greater than w = 0.5 m/s. In Figure 5.21, a similarity is clearly observed between the results obtained with both models, with slight differences at the systole peak, as already discussed, and at the decelerating point of the systole (t = 0.33s). Initially (t=0.07s), the jet is small, because the flow is beginning to be accelerated. As time progresses, the velocity values increase up to the maximum flow point. At the third point (0.33 s), when the fluid being pumped is being decelerated, the iso-surface equal to w = 0.5 m/s extends over the entire ascending region of the aorta, indicating significant larger velocity than instant 0.07s (with the same flow rate), when velocities greater and equal to w = 0.5 m/s are restricted to a small region near the valve inlet. This occurs because although smaller flow rate is entering the aorta, after the peak, the reflection of this reduction hasn´t reached the whole region, where faster fluid was present. At points 2 and 3 it is possible to observe some recirculation around the inlet jet. However, during the diastole, since the inlet jet is not driving the flow, the velocity is significantly reduced and a complex recirculation is observable in practically all the aorta, this being present even in the superior exits and in the exit of the descending aorta. Due to this deceleration of the fluid, there is no longer the presence of the jet with w = 0.5 m/s since the fluid velocity is on the order of 0.3 m/s, until it reaches rest at the final instant.

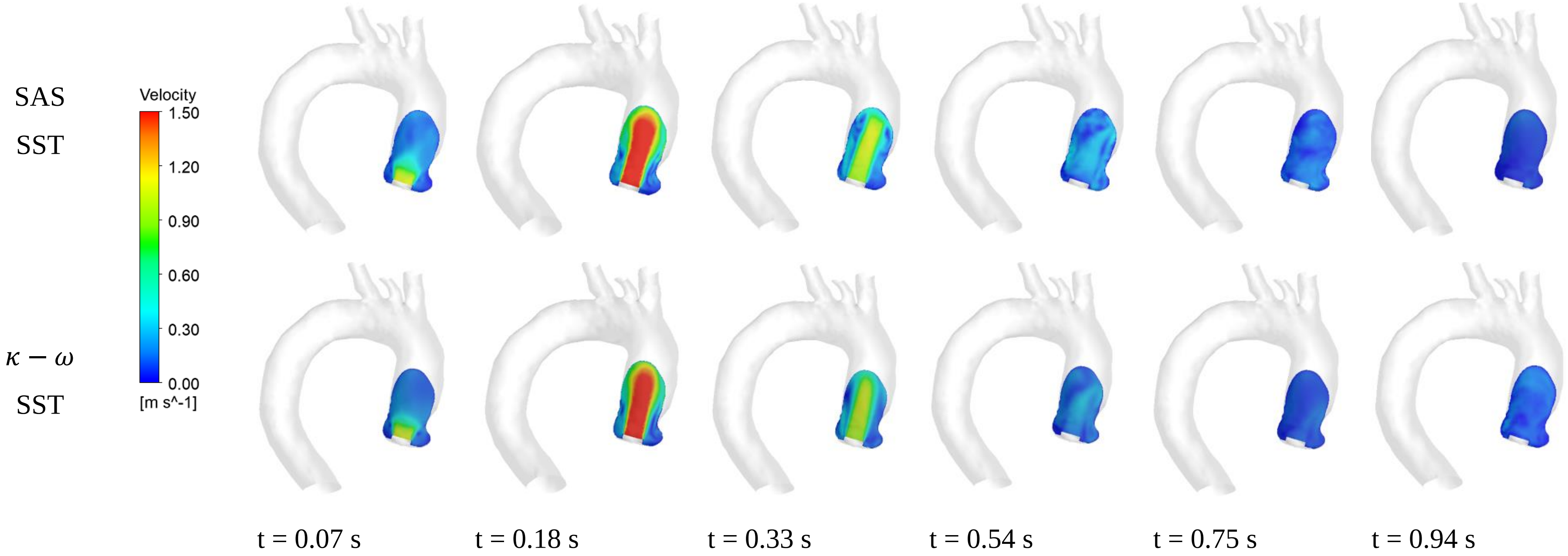

Figure 5.20 - Turbulence models impact in the velocity magnitude contours at center plane during the cardiac cycle. Case 1.

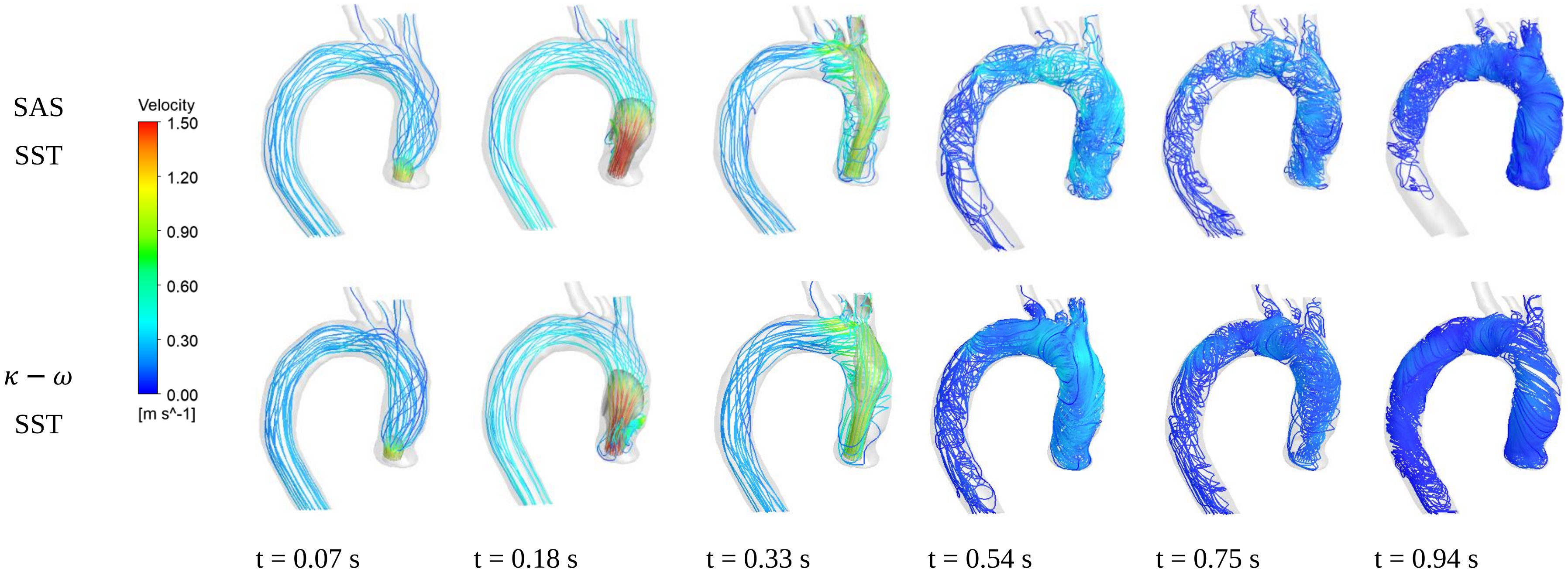

Figure 5.21 - Turbulence models impact in the streamlines and iso-surface of the z-velocity component contours at center plane during the cardiac cycle. Case 1.

To evaluate the impact of the turbulence models in the evolution of the wall pressure and wall shear stress during the cardiac cycle, only the systole time instants were selected, since during the diastole, the stress levels are lower, and it is the highest-pressure and WSS values those physicians and scientist are most concerned to assess.

The wall pressure is shown in Figure 5.22, and the same interval of 10 mmHg was defined for each time instant, however, as time increases, the pressure level also increases. The main point to be highlighted in this analysis is the qualitative similarity between the results obtained with both models, when compared at the same time. In the first instant, due to the low velocity values at the inlet, the pressure values are low, varying between 70-80 mmHg. As the velocity increases, the pressure values also increase as seen at the systole peak (0.18 s), when it is possible to clearly observe the region of maximum value, which corresponds to the region of impact of the jet on the aortic wall. Note that after the flow rate peak at the systole region at 0.18s, the inlet pressure keeps on increasing up to 0.26 s (Figure 5.11), and this will reflect in the pressure level observed at the time instant of Point 3 (0.33s), which is higher than in Point 2. It can be observed that the transitional model SAS-SST predicts larger pressure variation along the aorta, during the whole cycle, with smaller differences at the systole peak, when the flow is fully turbulent.

In Figure 5.23, the impact of the turbulence models in evolution of the shear stress distribution throughout the cardiac cycle is illustrated. Note that for both cases, the first instant the WSS values are very low, mainly due to the low-velocity values at the input. For the second instant (systole peak), the results are equivalent for both turbulence models, as already discussed. After the impact of the jet, at time 3, it is observed that the highest values of tension are in the superior region of the ascending aorta due to the spreading of the fluid after the impact on the wall. For the SAS SST model, a region with slightly higher values was observed than for the $\kappa - \omega$ SST model.

The impact of the turbulence models in the turbulence quantities during the cardiac cycle is examined in Figure 5.24 through Figure 5.26, through the turbulent kinetic energy, the turbulent viscosity and the Q −criteria.

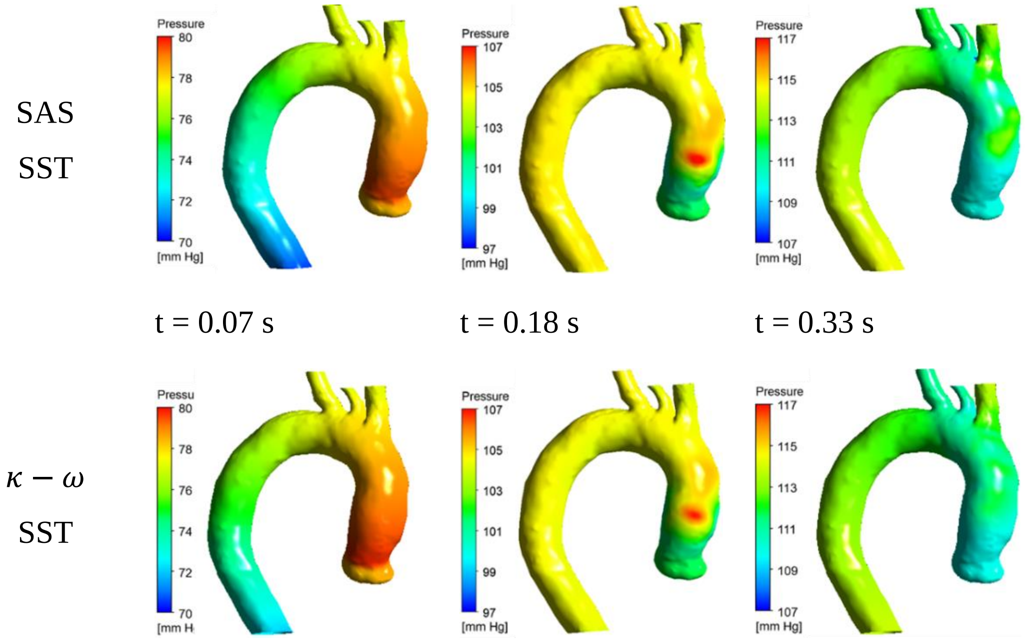

Figure 5.22 - Turbulence models impact in wall pressure for during the systole. Case 1.

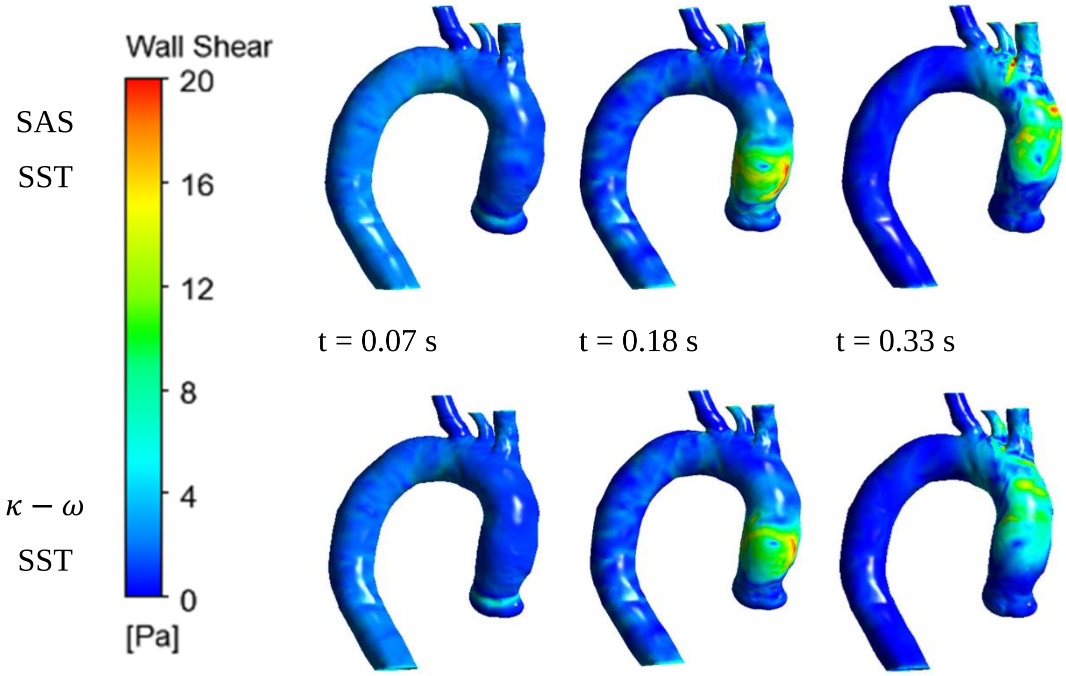

Figure 5.23 - Turbulence models impact in the WSS contours during the systole. Case 1.

In Figure 5.24 it is possible to observe that very different results were predicted from both models. It is known that the production of κ is proportional to the shear rate, so higher values of velocity are related with high shear rate, which induces higher values of κ. For both models, the value of κ increases during the cardiac cycle until the peak of systole, where its maximum is reached, then, κ decreases. It is observed that regions of higher value of κ are present in the $\kappa - \omega$ SST model solution since the turbulence is not damped in the model with the reduction of the flow velocity. With the SAS model, however, it is concluded that the effect of turbulence damping is present, because it reduced the production of κ to the point where there is no more turbulence at the end instants, and thus the formation of regions with higher values of turbulent kinetic energy is nullifying in the final instants.

Examining the turbulent viscosity distribution during the cardiac cycle in Figure 5.25, different results obtained with the two models can also be seen. The damping of the turbulence by the SAS-SST model can be clearly seen by the significant lower turbulent viscosity. The turbulent viscosity, μ_t is proportional to turbulent kinetic energy, and inversely proportional to the dissipation. The transition models act on the production and destruction of the turbulent quantities to reduce the turbulent viscosity during the relaminarization of the flow. Regions with higher values of κ will have higher values of turbulent viscosity. Thus, the results presented are equivalent to those shown in Figure 5.24. For the SAS SST model, the turbulent viscosity increases as κ increases and it decreases with decreasing velocity and κ. For the $\kappa - \omega$ SST model, there are larger regions with high turbulent viscosity, since for this model the generation of κ is not reduced. It grows along the cardiac cycle and starts to decrease during the deceleration of the flow, although still high results remain due to high values of turbulent kinetic energy.

In Figure 5.26, different Q values were selected for each time instant in order to visualize the formation of vortices and hairpin. The chosen values are indicated next to each time instant. It is noticeable that in both cases at the initial instant the number of vortices is small, in a toroidal format. For the SAS SST model, it is more difficult to identify the formation of the hairpin at the instant of maximum mass flow, while for $\kappa - \omega$ SST, it can be visualized as previously presented. At the end of the systole, beginning of the diastole (t=0.54s), no coherent structure was observed for the $\kappa - \omega$ SST model, although a few complex structures can be visualized in the results of the SAS SST model.

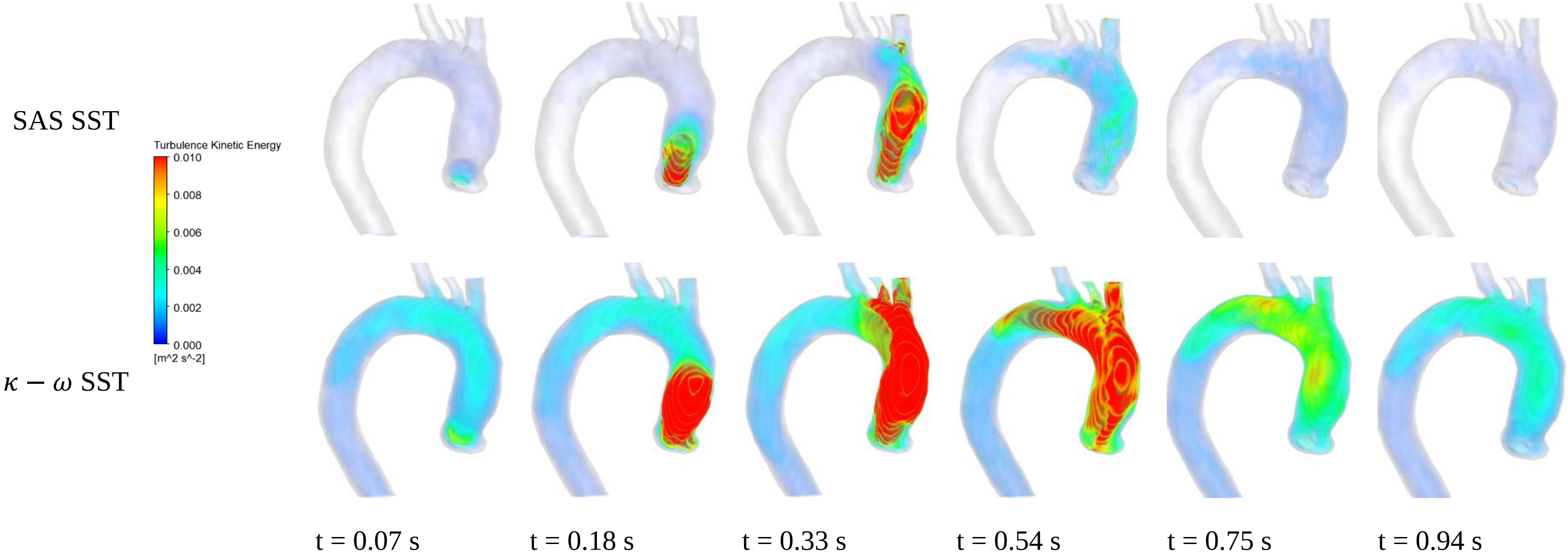

Figure 5.24 - Turbulence models impact in the turbulent kinetic energy during cardiac cycle. Case 1.

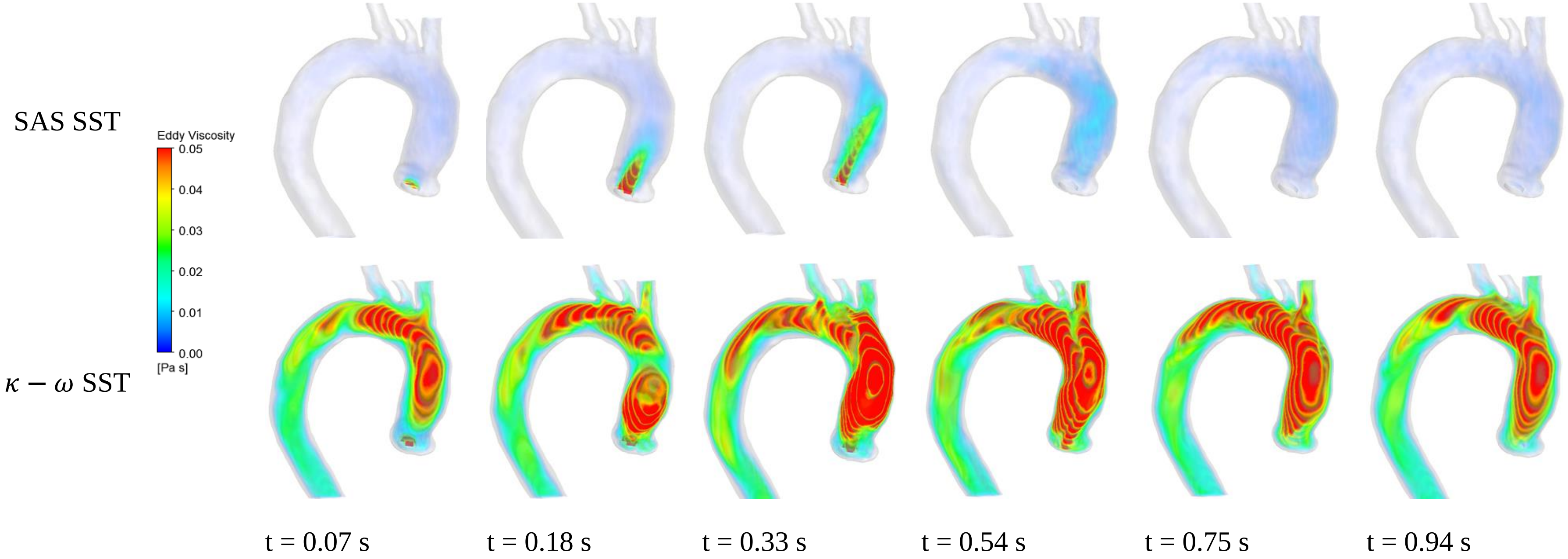

Figure 5.25 - Turbulence models impact in the turbulent viscosity during cardiac cycle. Case 1.

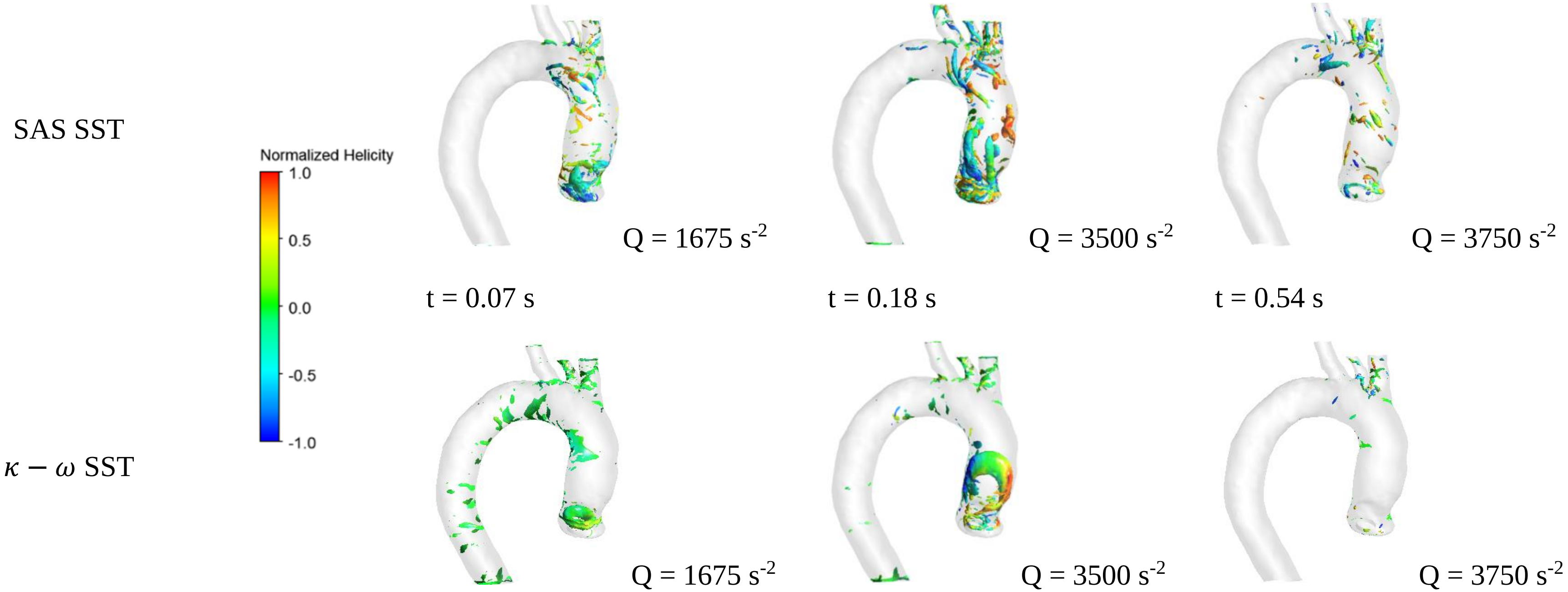

Figure 5.26 - Q - criterion evolution for Case 1

5.3.3 Time average variables

In this section, the cycle time average values of wall pressure and WSS are analyzed, as well as the oscillatory shear index, defined in section 3.4, obtained for Case 1, with both turbulence models are examined.

Figure 5.27, shows the values of TAP for Case 1 for the $\kappa - \omega$ SST and SAS SST turbulence models. It is easy to notice that both qualitatively and quantitatively the results are similar. For the $\kappa - \omega$ SST model, the average value was higher than the SAS SST, while the maximum value is higher for the SAS SST. Visibly, the region of high values is concentrated in the ascending region, close to the point of jet impact. A larger region with high values for the $\kappa - \omega$ model is consistent with the highest average value for this case. Thus, it can be concluded that the turbulence model had some impact on TAP values in the region of interest at the aortic wall.

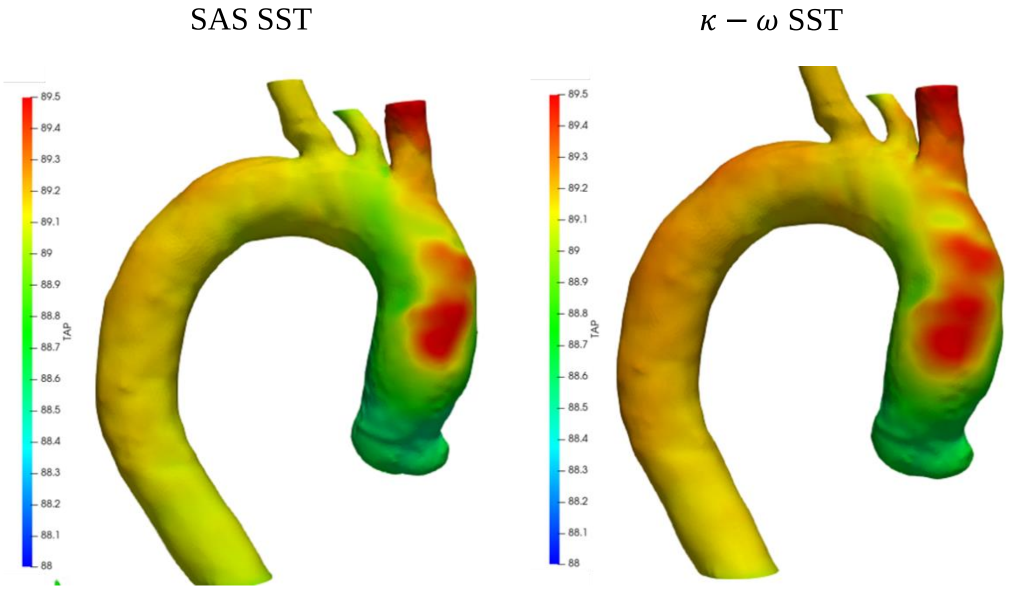

TAP_{mean}=88.85 mmHg TAP_{max}=89.59 mmHg TAP_{mean}=88.93 mmHg TAP_{max}=89.57 mmHg

Figure 5.27 – Turbulence models impact in TAP. Case 1

The impact of the turbulence model in the time-average of WSS (TAWSS), are shown in Figure 5.28, where it was observed that qualitatively there was also not much difference in the TAWSS field in the aorta, and the highest values, as in the case of TAP, were found in the region of the ascending aorta, close to the jet impact region. However, quantitatively, there were some differences in the average values and mainly in the maximum value in the region of interest. In this region the SAS turbulence model presented a maximum value higher than the $\kappa - \omega$ This fact indicates that the turbulence model does not have a negligible impact in the TAWSS values in the region of interest.

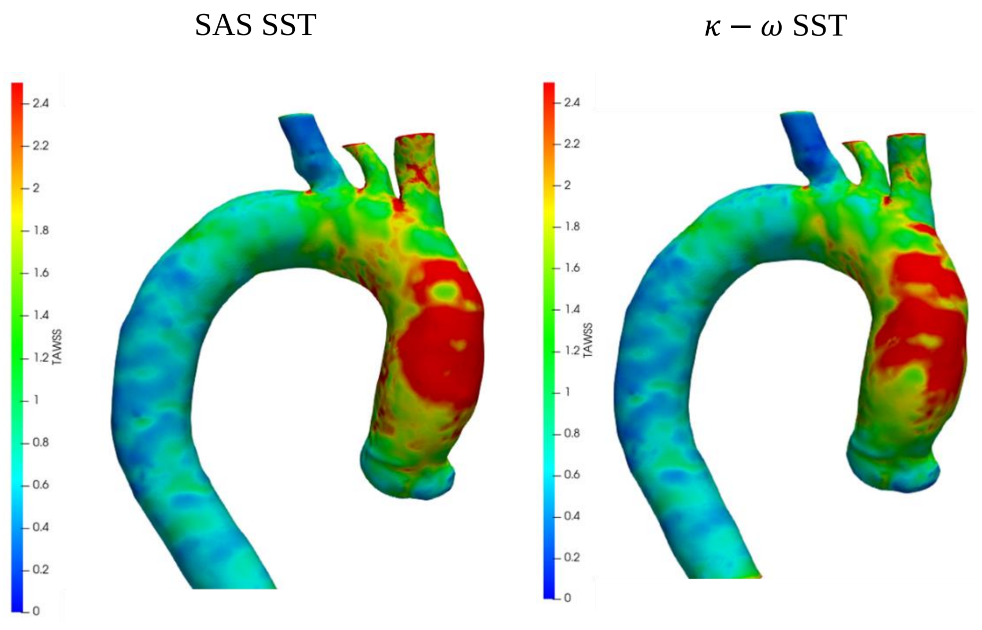
SAS SST

$\kappa - \omega$ SST

$TAWSS_{mean}$=1.76 Pa $TAWSS_{max}$=5.34 Pa

$TAWSS_{mean}$=1.56 Pa $TAWSS_{max} = 4.68$ Pa

Figure 5.28 – Turbulence models impact in TAWSS. Case 1

In addition to the quantities TAP and TAWSS, it is also interesting to evaluate the Oscillatory Shear Index (OSI) (Eq. 3.87), as shown in Figure 5.29. According to Gabriel *et al.* (2016), there is widespread use of the OSI metric spatiotemporal quantification of oscillatory flow in cardiovascular flow patterns studies. Besides that, high OSI values may facilitate the beginning of the atherosclerosis disease (Harloff *et al.*, 2010).

Examining the distribution of OSI obtained with the two turbulence models for Case 1 in Figure 5.29, it is possible to observe that for both turbulence models, high values of OSI were found in the aortic wall. These higher OSI values are in the aortic root, aortic arch and in the middle and end of the descending aorta. As described by Ibanez (2019), it is possible to observe that the TAWSS and OSI values are inversely proportional, concluding that high OSI values imply low WSS values and these can facilitate the onset of atherosclerosis.

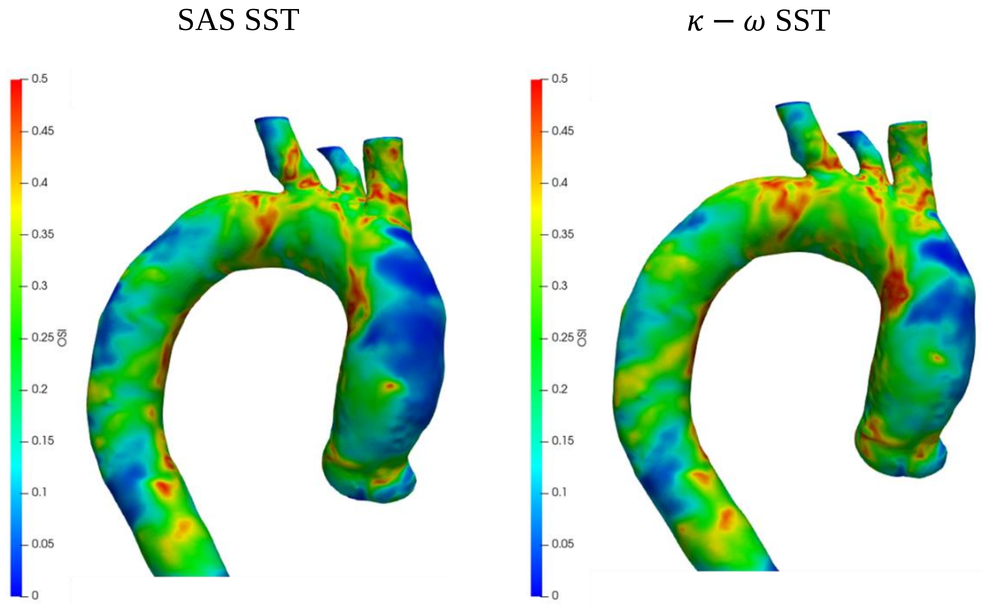

Figure 5.29 - Turbulence models impact in OSI. Case 1.

5.4 Impact of boundary conditions

The evaluate the impact of different boundary conditions during the cardiac cycles (Figure 5.30), in the flow field, representing different patients with different hear beats, corresponding to Case 1 and Case 2, the turbulence transitional model SAS SST with intermittence was selected.

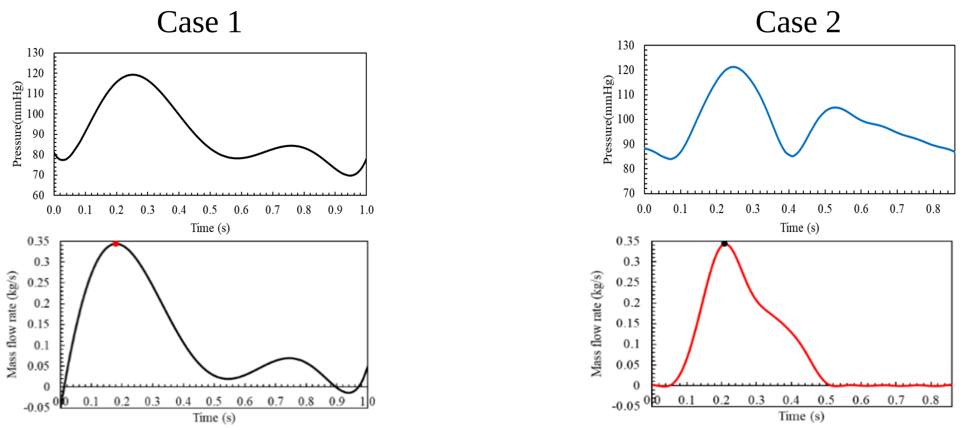

Figure 5.30 – Inlet pressure and total mass flow rate. During the cardiac cycle. Case 1 and Case 2.

Note in Figure 5.30, that although both cases present the same maximum mass flow rate and maxim inlet pressure, Case 1 remains during a long period of time with higher flow rate than Case 2. Note also, that in both cases, the pressure peak occurs at approximately at the same time instant, after the mass flow rate peak. However, the minimum pressure of Case 2 is higher, and the cycle is shorter.

In this section the same strategy presented in the previous section is employed, i. e., first, it was evaluated the impact of the boundary conditions in specific time instants of the cardiac cycle; then the mean temporal study was performed.

5.4.1 Flow variables at the systole peak. SAS-SST

Figure 5.31 presents the velocity data for Case 1 and Case 2 at systole peak. The velocity vector magnitude is shown in the central and transversal planes, as well as streamlines and the w =0.5 m/s iso-surface. Analyzing the flow in Figure 5.31, the jet is significantly longer for Case 1 than Case 2, and it also is wider. This occurs, because for Case 1 there is a long period of time with high flow rate entering the domain. However, the streamlines are similar for both cases, with a small recirculation near the inlet jet. A consequence of the shorter jet, the velocities are smaller at the upper planes.

In both cases, it is possible to notice lower values of velocity in the region of the aortic root and values of the order of 0.75 m/s in the middle of the center plane. In quantitative terms, the results of Case 1 presented the highest average value in the plane, on the other hand, Case 2 presented a higher value of maximum velocity in the central plane. Such a case indicates that the boundary condition had a strong impact on the values of this comparison.

Pressure and shear stress at the systole peak can be examined Figure 5.32 for the two cases. In case 2, the point of maximum pressure, that is, where the jet impacts the aortic wall, is much lower than in Case 1. At the same time, there is a region of low-pressure values for Case 2 in the aortic root region, a fact that occurred due to the concentration of the highest velocity values in this region. For Case 1, these lower values are more spread out in the ascending aorta, due to the greater prolongation of the jet and greater distribution of the fluid in this region. Finally, it is important to mention that Case 2 presented a much higher scale of values than Case 1, since the range of inlet pressure is higher for Case 2 than for Case 1.

Case 1 Case 2

$\left|\vec{V}\right|_{mean}$=1.02 m/s $\left|\vec{V}\right|_{max}$=1.78 m/s $\left|\vec{V}\right|_{mean}$=0.72m/s $\left|\vec{V}\right|_{max}$=1.99 m

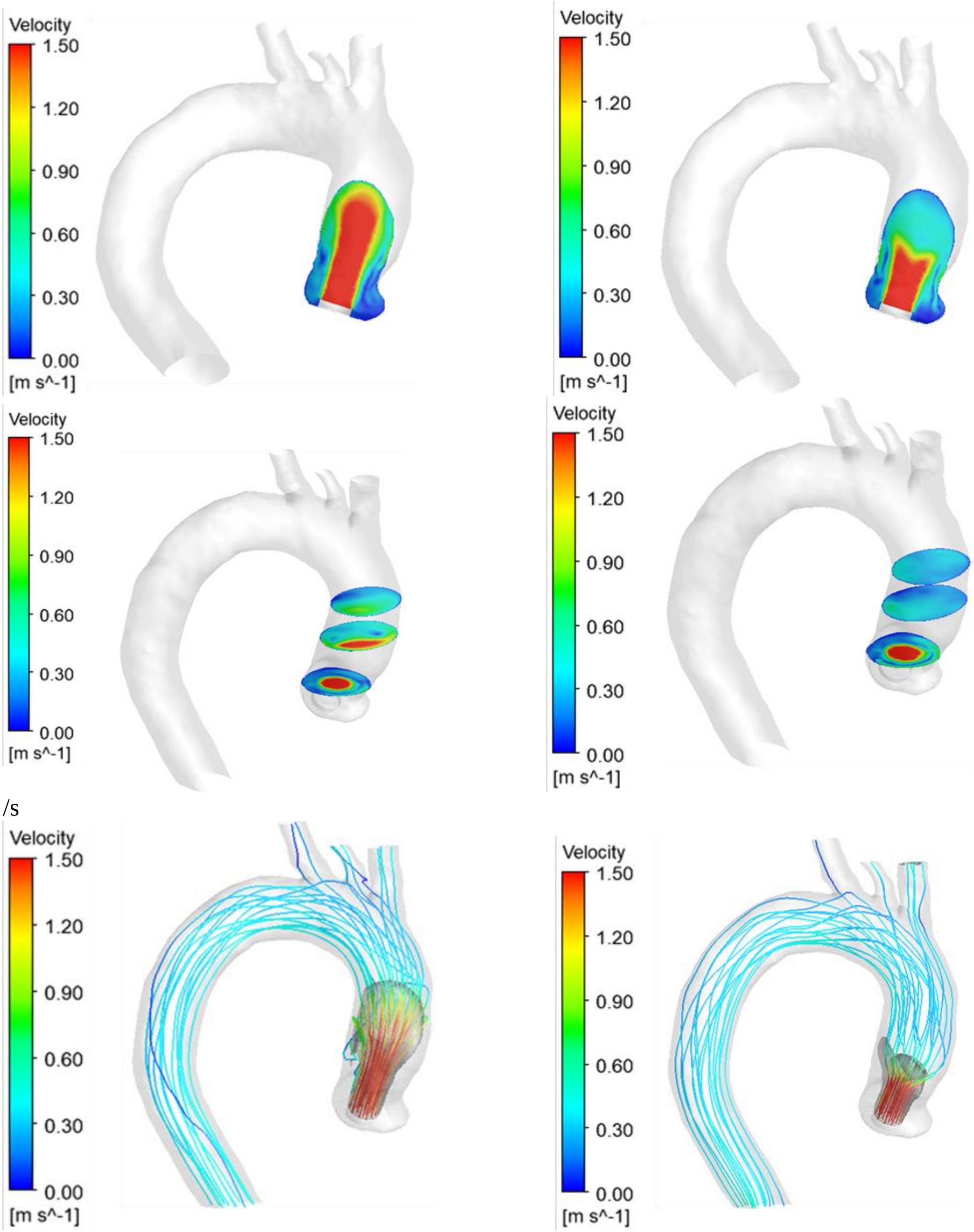

/s

Figure 5.31 – Velocity vector magnitude on central and transversal planes, w=0.5 m/s iso-surface and streamlines, at the systolic peak for Case 1 and 2. SAS-SST.

It can also be seen that the impact of the boundary condition in the WSS distribution is significant. For Case 1, as already discussed, the highest values are along the ascending aorta, close to the jet impact region. For Case 2, as for the pressure distribution, the highest values are close to the aortic root region, forming a kind of ring. This ring of high values is located exactly in the region of higher pressure, indicating that there is a correlation between these two variables and their corresponding extreme values.

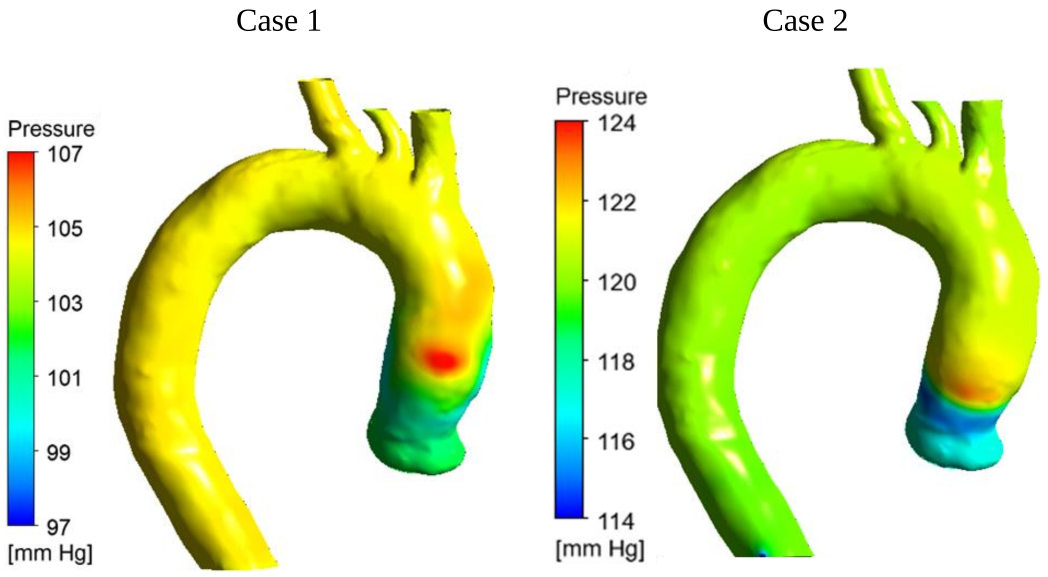

P_{mean}=104 mmHg P_{max}=107 mmHg P_{mean}=120 mmHg P_{max}=123 mmHg

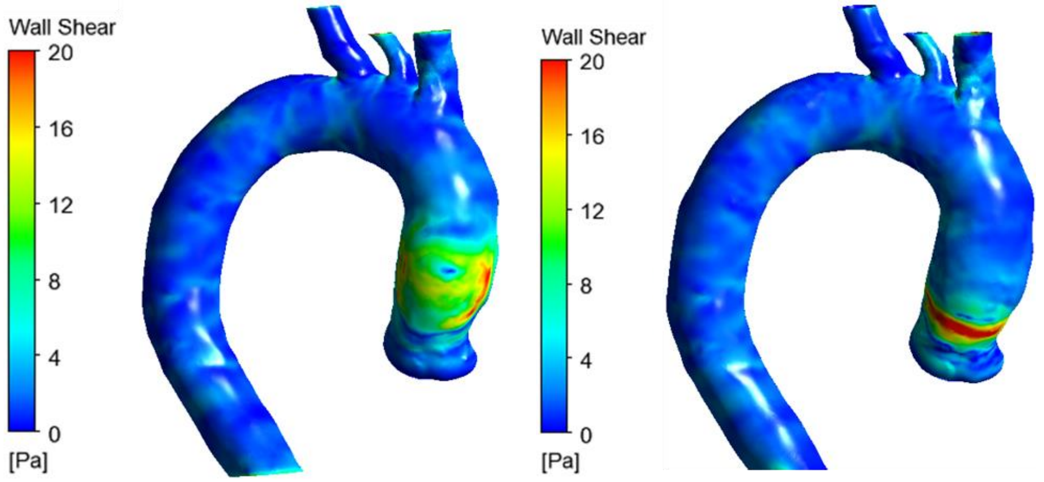

WSS_{mean}=2.18 Pa WSS_{max}=73.41 Pa WSS_{mean}=2.19 Pa $WSS_{max} = 80.20$Pa

Figure 5.32 – Wall pressure and WSS at the systolic peak for Case 1 and 2. SAS-SST.

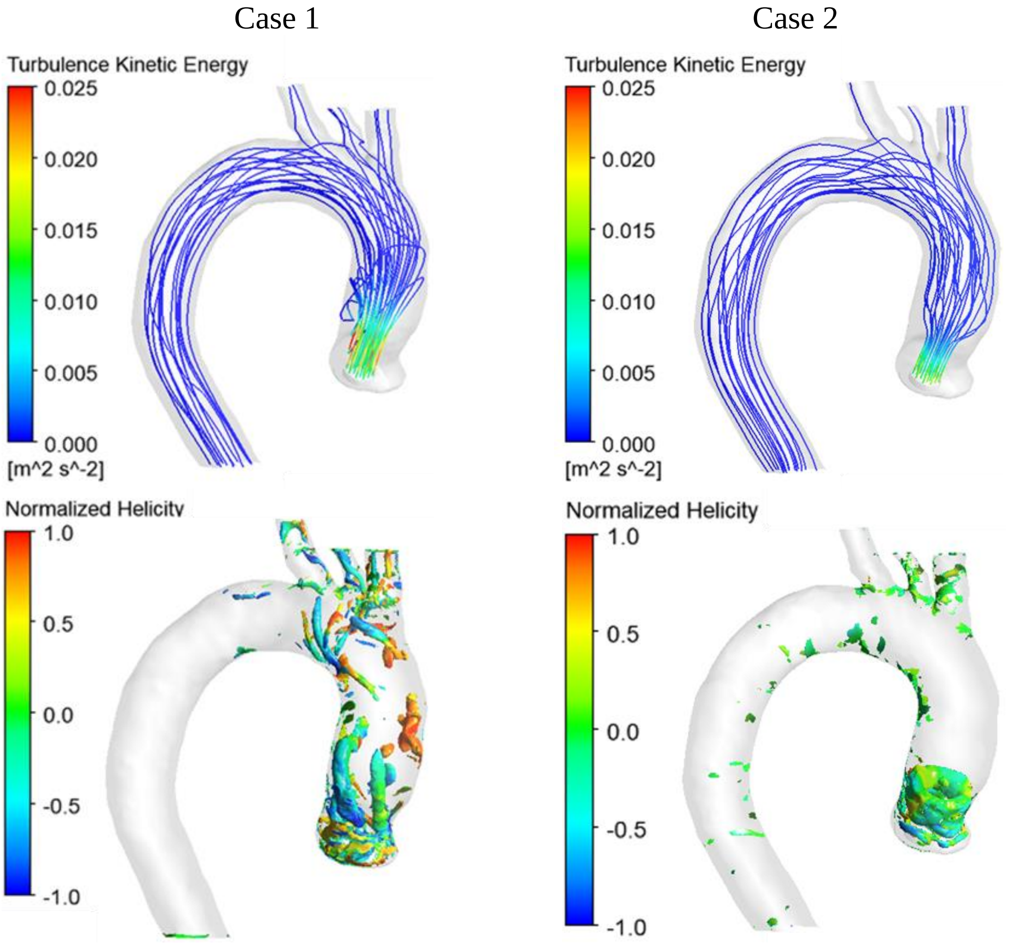

Figure 5.33 - Streamlines colored by turbulent kinetic energy and Q – criterion colored by normalized helicity for Case 1 and Case 2. SAS-SST.

Turbulent quantities can be examined in Figure 5.33, where the turbulent kinetic energy is plotted on the streamlines, and the normalized helicity is plotted with the Q – criterion. Note that for Case 2, smaller values of κ were predicted in relation to Case 1. At the same time, the values of κ in Case 2 are in a smaller region, close to the aortic root, a fact already expected due to the results presented in Figure 5.31, since the jet is concentrated at the inlet region. For Case 1, higher values are observed both in the aortic root and above it. Such results agree with the jets shown in Figure 5.31, indicating that larger values of κ are present along the respective jets. The Q - criterion predicted for Case 2 has the shape of a circular toroid, which are in the region of the aortic root. In Case 1, the structures are more spread out, not forming a hairpin. Note that the locations of these coherent structures are located exactly in the region of highest WSS values in the aortic wall for both Case 1 and Case 2. This result is expected since higher WSS values induce higher vorticity values and consequently higher helicity values. That is, where there is a greater value of WSS, there is a greater value of helicity.

5.4.2 Flow variables along the cardiac cycle. SAS-SST

Aiming to evaluate the results at different times of the cardiac cycle, Figure 5.34 shows the time instants selected for Case 1 and Case 2, employing the same strategy used in the previous analysis. In diastole, the three selected points present practically zero flow and were selected so that they are equidistant in the cycle.

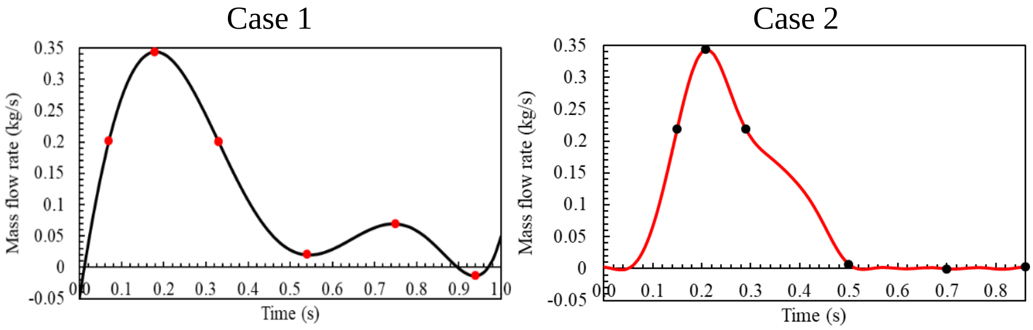

Figure 5.34 - Selected points for Case 2

Figure 5.35 and Figure 5.36 can be examined together, since the magnitude of the velocity vector is shown in the central plane in the former and w=0.5 m/s iso-surface and streamlines in the later. Note that an interesting fact happened at Points 2 and 3 of each case. It is possible to notice that for Case 1, the jet strikes the aortic wall in 0.18 s and decelerates from there, as indicated at the instant of 0.33 s. On the other hand, for Case 2, at the instant of maximum flow, the fluid has not yet reached the wall, and the same happened only in 0.29 s. If we look at the flow graphs in each case, it is easy to see that more fluid volume has already entered the aorta for Case 1 than for Case 2, thus explaining this difference between Points 2 and 3 of each case. Finally, during diastole, it is possible to observe that the results are qualitatively similar, where the fluid starts to decelerate reaching very low velocities values at the last selected moment.

For the streamlines and jet the comparison between Cases 1 and 2, there is a difference in the systole points as seen in Figure 5.36. For case 1, at the instant of maximum flow (0.18 s), the jet impacts the wall and spreads inside the aorta with a deceleration (0.33 s), however, for Case 2, at the instant of maximum flow (0.21 s) the jet has not yet reached its maximum size for impact on the wall, the impact only occurs at the instant of 0.29 s where, due to the impact, it is possible to observe the appearance of more recirculation zones, as seen in Case 1 for the time instant of 0.33s. For the first instant of diastole (0.54 s), for Case 1 it is observed that the fluid starts to decelerate strongly, to the point that the jet with the selected value is no longer present. On the other hand, in Case 2, at the same time instant, there is still the presence of the jet, indicating that there is still fluid with a velocity greater than or equal to w = 0.5 m/s. For both cases, it is possible to notice great recirculation inside the aorta at Point 4. For the two following moments, for Case 1, it is observed that the fluid continues to decelerate with great recirculation in practically the entire aorta with very flow velocity. In Case 2, the fluid also decelerates with recirculation, but this is more present in the region of the ascending aorta, in the superior outlets and in the aortic arch.

In Figure 5.37, it is possible to observe the impact of the boundary condition on the pressure field. Note that Case 2 presents higher pressure values at all chosen moments, since the inlet pressure range is higher. At the same time, at the instant of maximum flow, it is possible to observe that for Case 1 the jet has already impacted the wall, while in Case 2 the jet is still developing, reaching the wall only at t= 0.29 s, where the largest pressure values are seen, as indicated by the redder region in the ascending aorta. As in the section where the impact of the turbulence model was evaluated, here it can be seen that the pressure values increase as the cardiac cycle progresses, since the pressure peak occurs after the flow rate peak.

In Figure 5.38 it is possible to verify that Case 2 presents higher WSS values, which are concentrated in the aortic root region, because the flow has not yet reached its peak flow and the fluid has not traveled through most of the ascending aorta. For time instant 2, as already observed, Case 1 presents a region of higher values more spread out near the region of impact of the jet on the wall, while in this case, the jet has not yet fully impacted the wall. Thus, the highest values are still close to the aortic root region, forming a kind of ring of maximum values. For time instant 3, in Case 1, the blood jet has already covered a good part of the ascending aorta, creating a larger region with higher values of WSS. In Case 2, the jet impacts the wall at instant 3, resulting in a wider region than in the previous instant, with high values close to the point of impact of the jet. Thus, we can observe a certain delay for the impact of the jet on the wall for Case 2 when compared to Case 1.

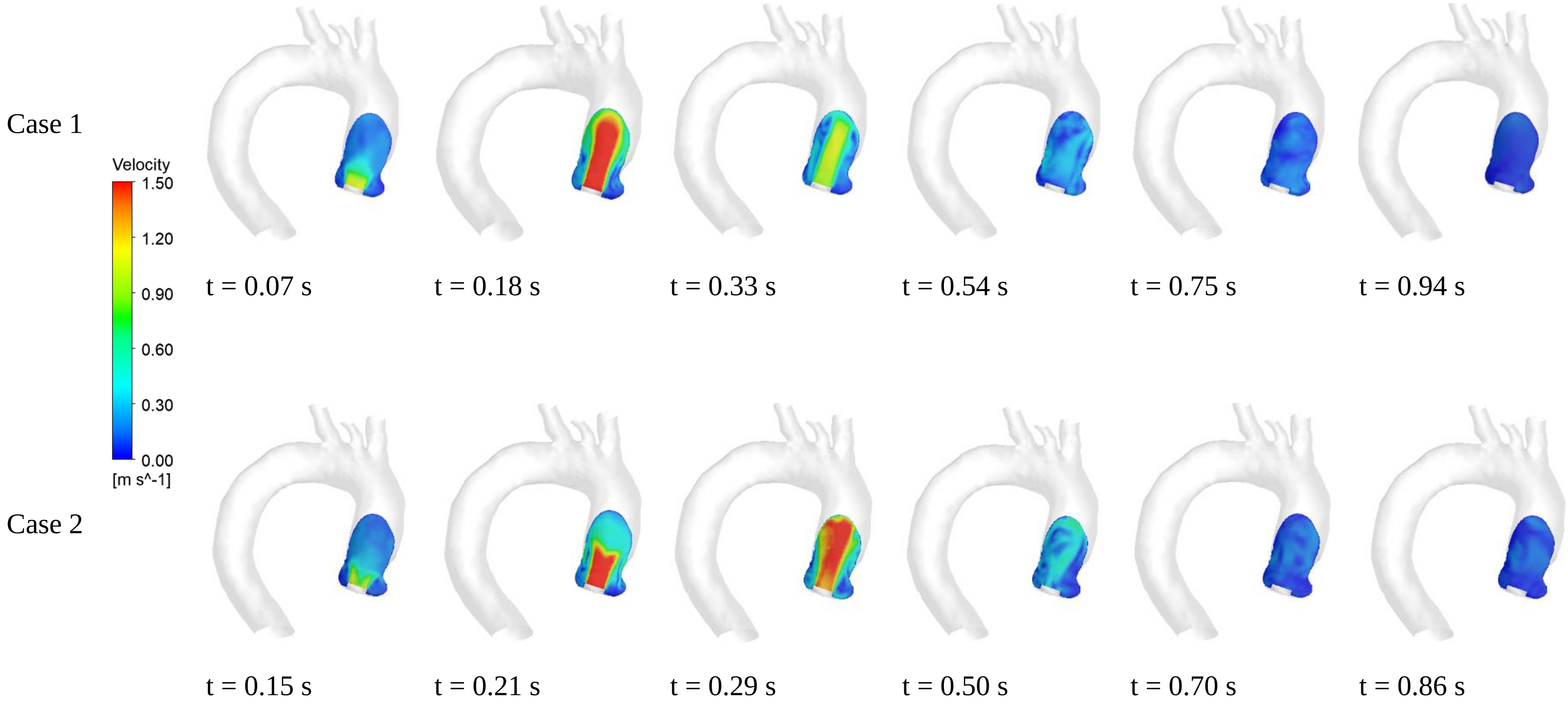

Figure 5.35 - Velocity contours during the cardia cycle for Case 1 and Case 2. SAS.SST.

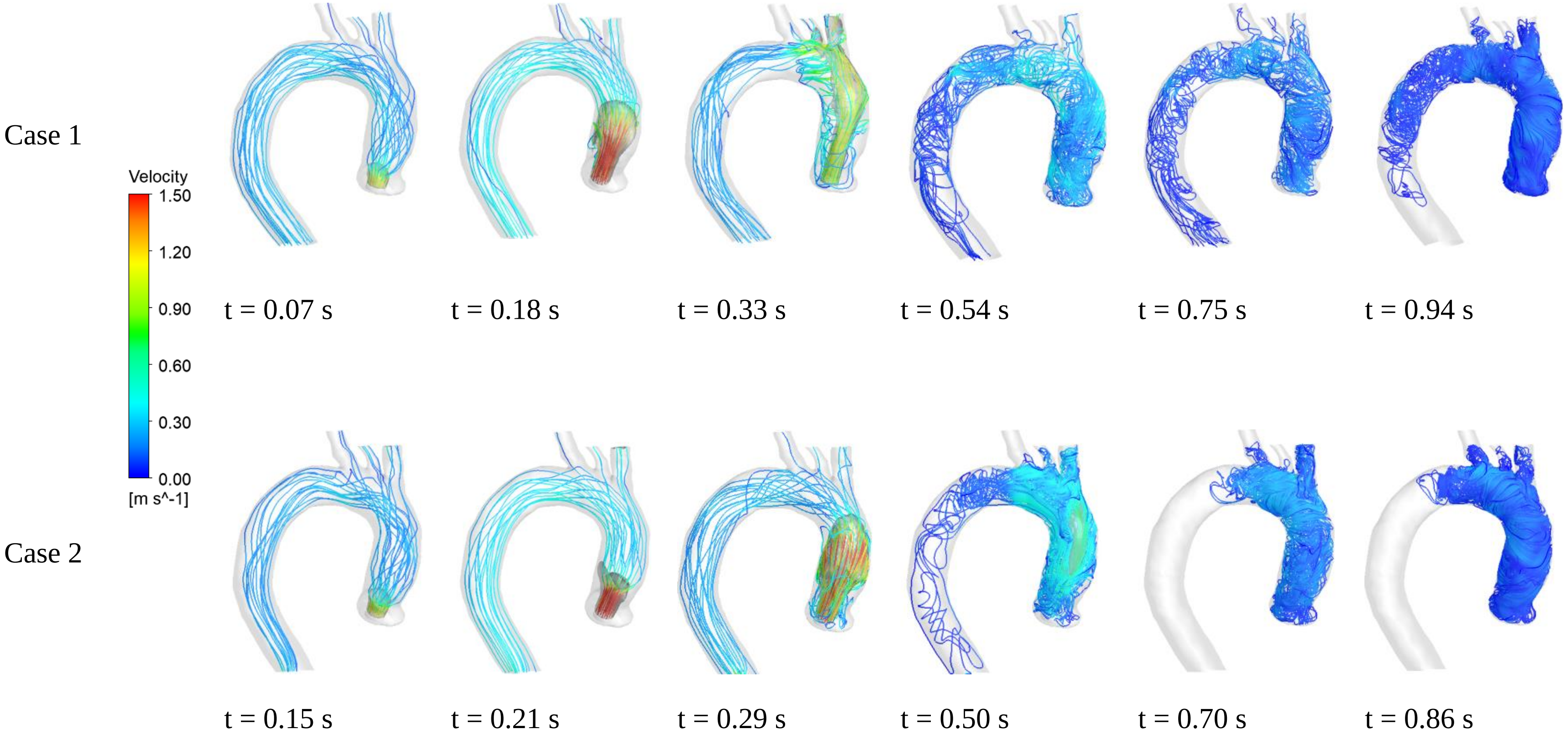

Figure 5.36 – Streamlines and iso-surface for Case 1 and Case 2

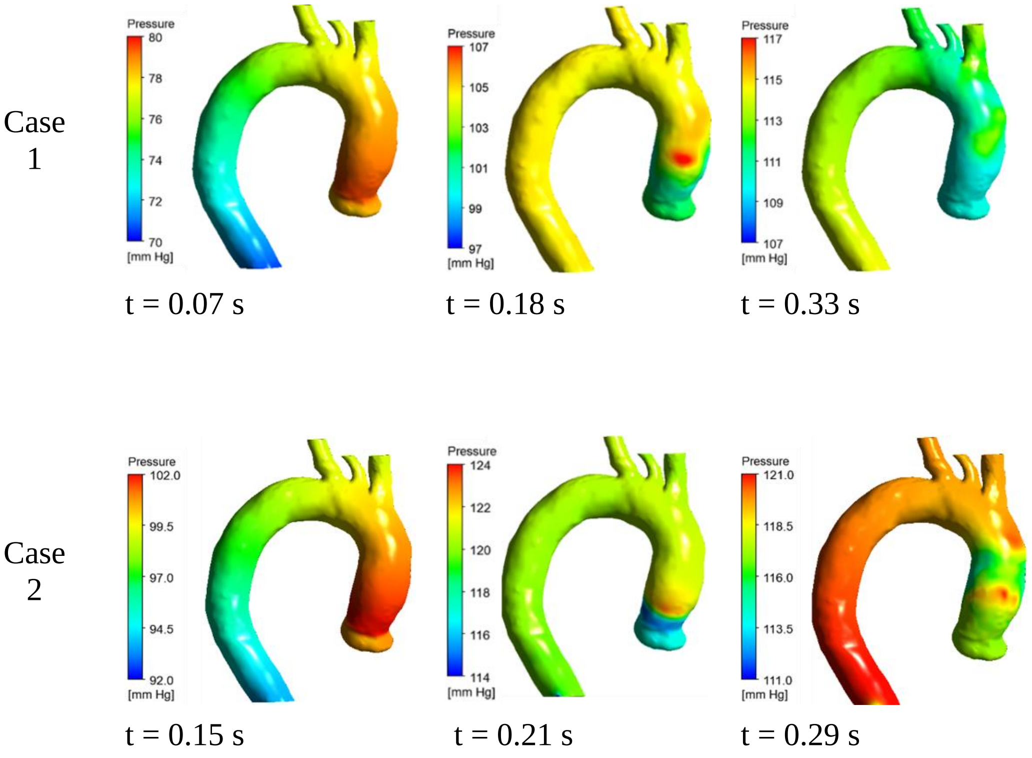

Figure 5.37 - Pressure contours during the systole for Case 1 and Case 2. SAS-SST.

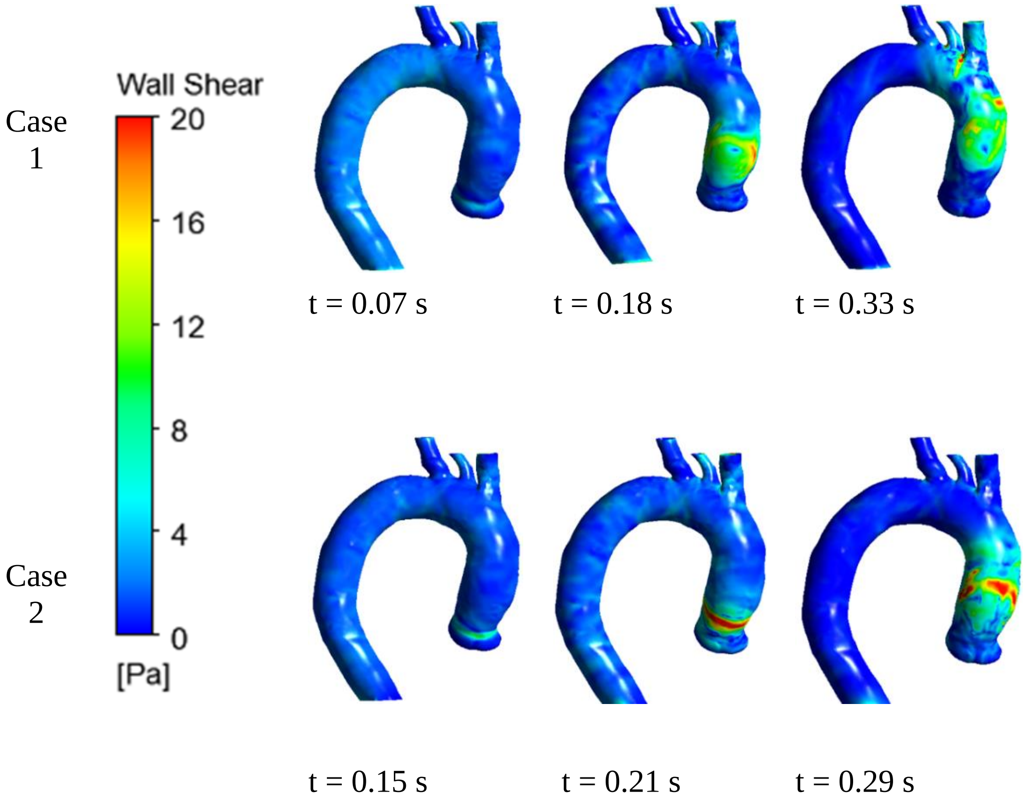

Figure 5.38 - WSS contours during the systole for Case 1 and Case 2. SAS-SST.

The effect of the boundary condition on κ during the cardiac cycle, in shown in Figure 5.39. For Case 1 and Case 2, the initial instants are very similar to each other. However, in the following points there are great differences. While in Case 1 at time 3, there is a larger region with high values of κ, in Case 2, this region is still small because the fluid jet is still growing as can be seen in Figure 5.36. For the following time instants, for Case 1, with the decrease in velocity, the κ values also decrease. For Case 2, at these time instants, higher values of κ are perceived, since at these instants the velocity inside the aorta is higher, as seen and discussed earlier (Figure 5.36). It is only at the final time instant that there is practically no value of κ, since in both cases the fluid is practically at rest.

The behavior of turbulent viscosity throughout the cardiac cycle (Figure 5.39) is similar as for κ. For Case 1, there are higher values of viscosity in the first three chosen instants, since velocity is high, as well as κ, causing regions with higher values of turbulent viscosity. On the other hand, in the subsequent time instants, Case 2 presents regions with greater turbulent viscosity, since in these moments there are still regions with higher values of velocity (Figure 5.36), generating greater turbulent kinetic energy and consequently greater μ_t. Finally, it is important to mention that even in the final moments, for Case 2 there are still values between 0.01 and 0.03 Pa.s of turbulent viscosity while for Case 1, the values are in the range of 0 to 0.01 Pa.s, indicating that in Case 2, the flow still presents a little turbulence when compared to Case 1.

In Figure 5.41, the Q-criterion evolution is shown for both cases at the different time instants. At the initial, the beginning of the hairpin formation can be seen for Case 1, while for Case 2, it presents only a small structure in the shape of a toroid. For time instant 2, Case 1 already illustrates coherent structures with high values of normalized helicity because of high values of WSS (Figure 5.38). At the final time instant, with the pressure drop for Case 1, the coherent structures disappear, while in Case 2, the highest values of WSS present at that instant (Figure 5.38) are related to higher values of normalized helicity and more structures in the inside.

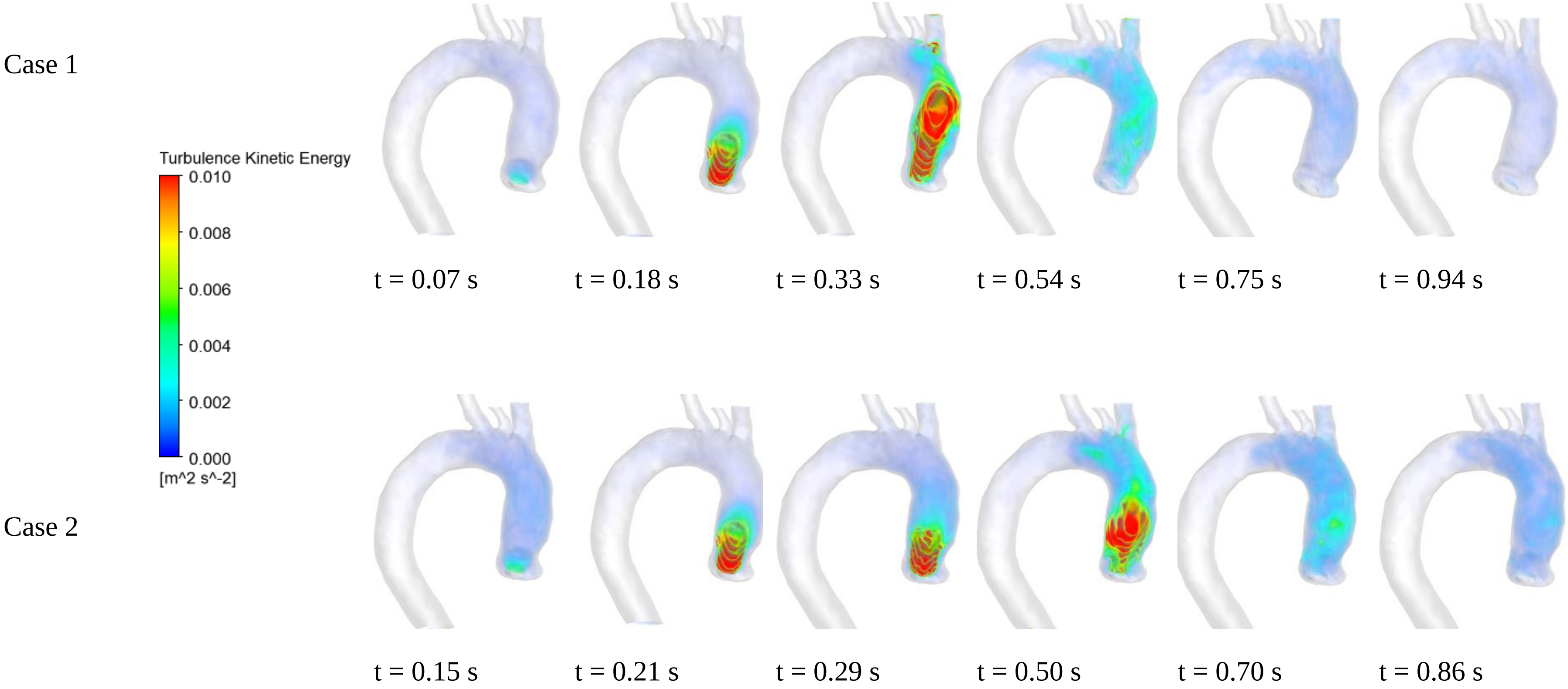

Figure 5.39 - Turbulent Kinetic Energy evolution for Case 1 and Case 2. SAS-SST.

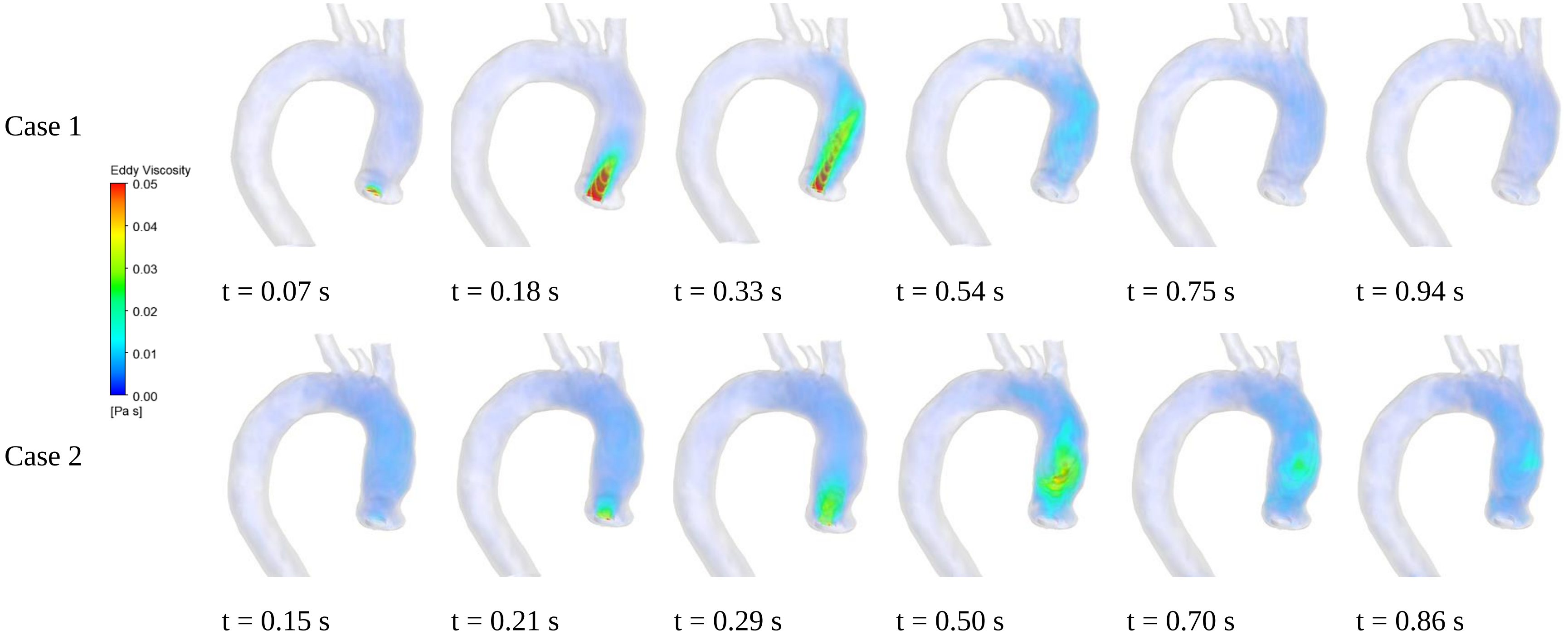

Figure 5.40 - Turbulent Viscosity Evolution for Case 1 and Case 2. SAS-SST.

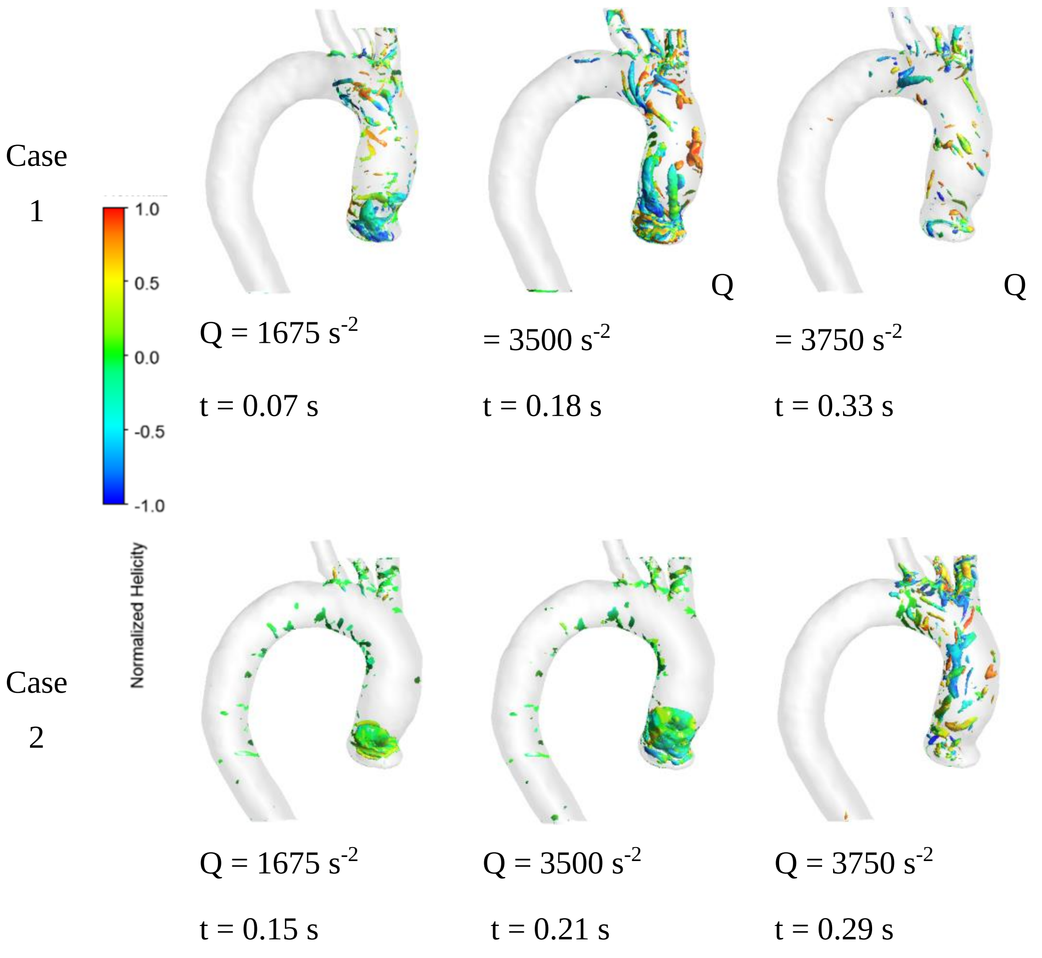

Figure 5.41 – Q-criterion evolution for Case 1 and Case 2. SAS-SST.

5.4.1 Time average variables. SAS-SST

Concerning to the mean temporal study, the results for the TAP, TAWSS and OSI are shown in Figure 5.42, Figure 5.43 and Figure 5.44, respectively. In this comparison, it is possible to notice a qualitative and quantitative difference in the results of TAP on the wall (Figure 5.42). For Case 2, there are few regions with high values, which are concentrated in the ascending aorta. On the other hand, as already described, in Case 1 the values extend over almost the entire middle and upper part of the ascending aorta, indicating a greater distribution of maximum values. Quantitatively, the average and maximum values of Case 2 are much higher than those of Case 1, in the order of 10 mmHg. The higher value in case 2 is explained by the higher inlet pressure values along the cardiac cycle for case 1. Observing Figure 5.30, the values during systole are equivalent, ranging from 80 mmHg to 120 mmHg, however, after the middle of the cycle, in the period of diastole, Case 2 has higher pressure values, which are reflected in higher pressure values on the wall. Case 2 presented a region of values greater than in Case 1, although its maximum value was close to Case 1. The higher average value in the region of interest in Case 2 was mainly due to the larger area with higher values.

The impact of the boundary condition in the WSS was smaller than in the pressure, as can be seen in Figure 5.43, which shows equivalent distributions of TAWSS for both boundary conditions, with equivalent maximum TAWSS. However, Case 2 presents a higher average value.

Case 1 Case 2

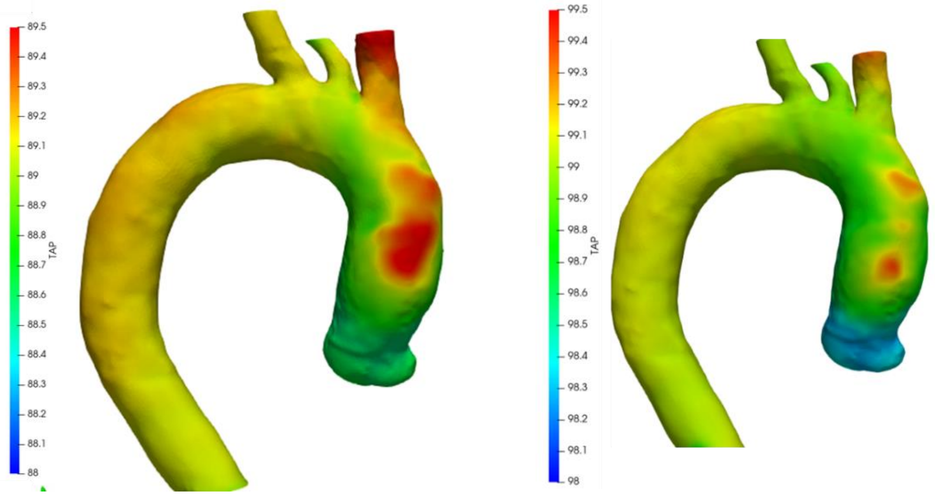

TAP_{mean}=88.85 TAP_{max}=89.59 TAP_{mean}=98.70 TAP_{max}=99.39

Figure 5.42 – TAP (mmHg) for Case 1 and Case 2. SAS-SST.

The OSI distribution for both boundary conditions are shown in Figure 5.44. Note that the OSI values are inversely proportional to the TAWSS values. In this case, it is worth highlighting the highest OSI values for the Case 2, which in this case are more prominently present throughout the aorta, showing a more significant impact of boundary condition in the OSI distribution, obtained with the SAS SST model.

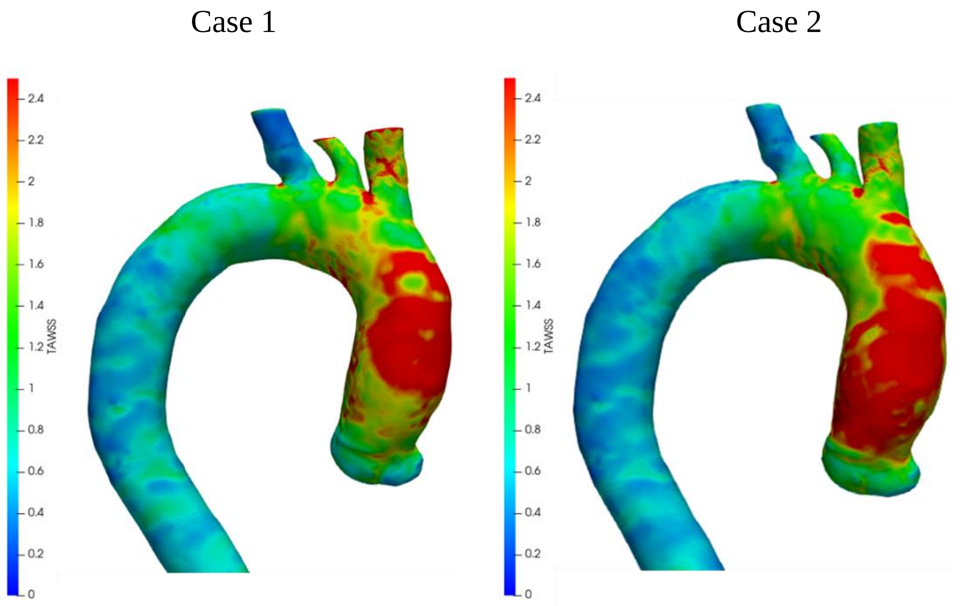

Case 1 Case 2

$TAWSS_{mean}$=1.76 $TAWSS_{max}$=5.34 $TAWSS_{mean}$=1.87 $TAWSS_{max} = 5.35$

Figure 5.43 – TAWSS (Pa) for Case 1 and Case 2. SAS-SST.

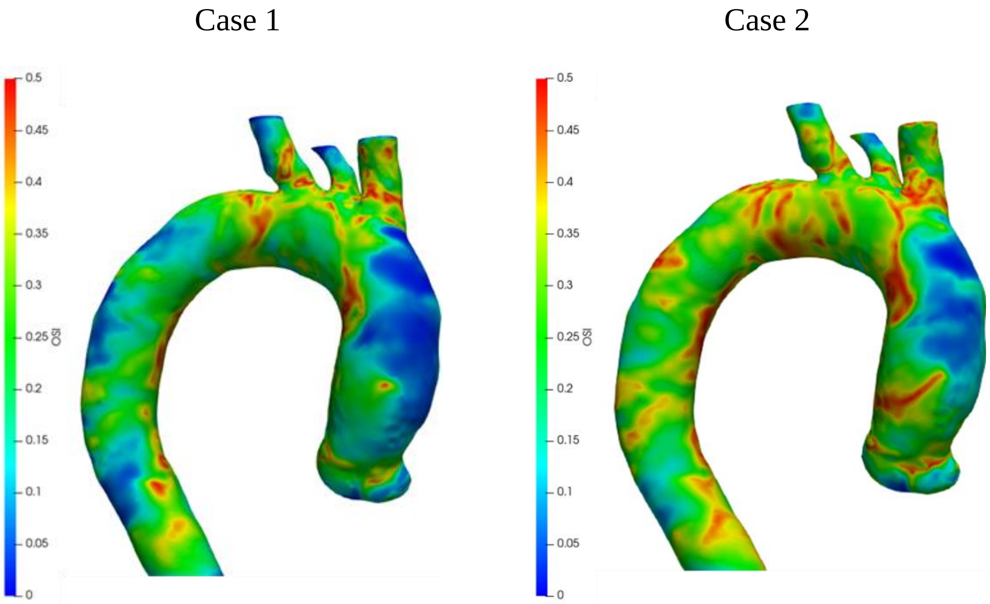

Case 1 Case 2

Figure 5.44 - OSI for Case 1 and Case 2. . SAS-SST.

6 FINAL REMARKS

The main objective of this work was to apply CFD to numerically evaluate the distribution of stresses (pressure and shear), velocity and turbulent quantities during the cardiac cycle, in the aorta of a patient who underwent TAVI. To achieve this, the present work was basically divided into two main parts.

The first part consisted of selecting a turbulence model capable of accurately predicting the flow field inside an aorta. To this end, different turbulence models were compared to high-fidelity PIV experimental data of Bessa *et al.* (2021), obtained for the same real scale aorta, during steady state, in the condition of maximum mass flow, employing exactly the same fluid properties and boundary conditions. The aorta model was created from tomography angiography images of the patient exam. Bessa *et al.* (2021) measured the velocity components and determined their mean values, as well as their fluctuations at six different planes parallel to the brachiocephalic artery ($x - y$ plane), where the system's origin was located.

Aiming to analyze the cardiac cycle, which is formed of two parts, systole (with high flow rate) and diastole (very low flow rate), the turbulence model must be capable of capture the transition from laminar to turbulent flow. Thus, two transitional models based on the URANS methodology were selected: Transitional $\kappa - \omega$ SST and SAS SST models. These model's prediction was also compared with the solution obtained with the κ-ω SST turbulence model employed by Ibanez et al. (2020). To select the most adequate turbulence model, velocity components, as well as turbulent quantities, like the turbulent kinetic energy (κ) and the components of the Reynolds tensor were evaluated. From the analysis performed, no model indicates a clear superiority in relation to the others. As the goal is to simulate and identify the impact of the laminar to turbulent transition and the relaminarization, the SAS-SST model was selected for further investigations of the cardiac cycle, due to the slightly better agreement obtained with the experimental data.

In the second part of this work, the blood flow in the ascending aorta was analyzed during the cardiac cycle, employing real blood properties, in the same aorta model. As mentioned, the SAS-SST model with intermittence was employed to predict the flow during the cardiac cycle. The flow parameters were only analyzed after a periodic regime had been attained. It was shown that three cycles were sufficient. However, to improve the quality of the results, all properties examined were obtained with the average of the data from the third to the fifty cycles.

The analysis of the cardiac cycle was subdivided into two sub steps. The first one was aimed to evaluate the impact of the SAS SST transitional model versus the κ-ω SST model on the results. For this step, there are no experimental data available, thus the objective was to verify the performance of the transitional turbulence model to damp turbulence and identify this impact in relevant flow parameters in relation to the κ-ω SST, previous examined by Ibanez et al (2020).

The impact of the turbulence models in the flow field was performed through the analysis of the magnitude of the velocity vector, the z-velocity component, streamlines, as well as wall pressure and wall shear stress (WSS). Turbulence quantities, like turbulent kinetic energy, Q-criterion and normalized helicity were also compared. These variables were examined at different time instants during the cardiac cycle. Further, time average variables within the cardiac cycle were examined (wall pressure, WSS and oscillatory shear index).

From the results obtained, it was shown that the transitional SAS SST model did not present any impact in the flow variable at the systole peak, when compared with the prediction of the κ-ω SST model. However, during the flow deceleration in the systole region and diastole, the transitional model damped the turbulence and significant differences were observed in all turbulent variables. The turbulent viscosity as well as κ were significantly reduced, and different coherent structures were obtained. However, qualitatively the flow behavior during the cycle was very similar. Because of the turbulence damping due to transition to laminar flow, significant impact was observed for the time average WSS (13% smaller) and for the oscillatory shear index, although approximately the same time average pressure was obtained with both models.

The last part of this work consisted in analyzing the impact in the flow field of different boundary condition, representing patients with different heart beats, consequently different cycles period, and different pressure and flow rate along the cycle. The SAS SST transitional model with intermittence was employed and two sets of boundary conditions varying with time were defined, based on physiological profiles. In both cases, pressure profile was prescribed at the inlet, with a total outflow mass flow rate profile, with the same percentage of distribution through the 4 outlets of the aorta. Case 1 was based on the work of Ibanez et al. (2020), while Case 2, was based on Johnson *et al.* (2020). In the selection of the boundary condition, care was taken so that both cases presented the same maximum flow rate and maximum pressure. In both cases, the pressure peak occurred after the mass flow rate peak. Case 2 presented an average pressure along the cycle higher than Case 1. Besides different period length, the cases presented different acceleration and deceleration along the systole. At the diastole period, smaller mass flow rate was imposed for Case 2 than for Case 1.

Examining the results obtained for both cases, it was clear that although the evolution of the flow is similar, the boundary conditions impacted on the evolution of the flow during the cycle. As the inlet jet enters the domain, during the acceleration period of the systole, a centered strong jet can be observed, with recirculating flow around it. The flow impacts at the aorta wall, resulting in peak of pressure. However, it was observed a delay of the flow development, i.e., different time instant of jet impact at the wall and resulting wall pressure and wall shear peaks. This delay of the flow development impacted directly on the turbulent quantities. Significant differences were observed with relation to the Q-criteria, and normal helicity distribution, resulting in different coherent structure for each case. With respect to the impact of the boundary conditions in the time average quantities, it was observed similar TAWSS, with almost the same maximum value and with a mean value only 5% higher for Case 2. As a result of the different time evolution of the flow during the cycle, Case 2 presented several small regions along the ascending aorta with high values of the OSI. The largest impact of the boundary conditions was in the time average pressure level, what was expected due to the higher inlet pressure values imposed during the cycle. However, the variation of the pressure level in relation to its mean value between both cases was negligible.

As a conclusion, it can be said that the selection of the SAS SST model with intermittency was positive, as it was able to demonstrate the transition effects of the flow. The flow distribution for different patients (represented by the different boundary condition) is qualitatively similar, but with different time evolution. The absolute values of the velocity, pressure and turbulence quantities presents a significant dependency on the prescribe boundary values. The largest impact was in the formation of the coherent structures.

From the analysis performed, it can be suggested, that this type of analysis must be personalized. However, with respect to time average results, normalization of the prediction may help to generalize the findings.

As suggestions for future works, it would be interesting to evaluate the impact of a better representation of the aortic valve, considering a realistic 3D model. A more realistic definition of the outflow boundary condition, employing the Windkessel model (Westerhof et al, 2009) can also improve the quality of the predictions. Further, simulating the same flow in the same domain with other turbulence models such as $\kappa - \omega$ with intermittency, LES and DNS would be of great value. Another suggestion is to evaluate the effects of aortic compliance through an FSI simulation, what would bring the results even closer to reality. Finally, the flow inside the aorta of different patients, with other combinations of boundary conditions can corroborate the findings of the present work.

REFERENCES

ABRAHAM, J. P.; SPARROW, E. M.; TONG, J. C.K.; BETTENHAUSEN, D. W. Internal flows which transist from turbulent through intermittent to laminar. **International Journal of Thermal Sciences**, vol. 49, no. 2, p. 256–263, 2010. DOI 10.1016/j.ijthermalsci.2009.07.013. Available at: http://dx.doi.org/10.1016/j.ijthermalsci.2009.07.013.

ALASTRUEY, Jordi; XIAO, Nan; FOK, Henry; SCHAEFFTER, Tobias;

FIGUEROA, C. Alberto. On the impact of modelling assumptions in multi-scale, subject-specific models of aortic haemodynamics. **Journal of the Royal Society Interface**, vol. 13, no. 119, 2016. https://doi.org/10.1098/rsif.2016.0073.

ALMEIDA, Gabriela de Castro. Numerical investigation of the evolution of blood flow patterns of different years in patients with ascending aortic aneurysm. no. February, 2019. .

ALMEIDA, Gabriela De Castro; TEIXEIRA, Pedro Soares. COB-2019-1362 EVALUATION OF TURBULENT PROPERTIES IN AORTAS WITH. no. 2007, 2019. .

BASRI, Adi A.; ZUBAIR, Mohamed; AZIZ, Ahmad F.A.; ALI, Rosli M.; TAMAGAWA, Masaaki; AHMAD, Kamarul A. Computational fluid dynamics study of the aortic valve opening on hemodynamics characteristics. **IECBES 2014, Conference Proceedings - 2014 IEEE Conference on Biomedical Engineering and Sciences: “Miri, Where Engineering in Medicine and Biology and Humanity Meet,”** no. December, p. 99–102, 2014. https://doi.org/10.1109/IECBES.2014.7047660.

BECSEK, Barna; PIETRASANTA, Leonardo; OBRIST, Dominik. Turbulent Systolic Flow Downstream of a Bioprosthetic Aortic Valve: Velocity Spectra, Wall Shear Stresses, and Turbulent Dissipation Rates. **Frontiers in Physiology**, vol. 11, no. September, p. 1–19, 2020. https://doi.org/10.3389/fphys.2020.577188.BESSA, G.M.; **Estudo do**

escoamento em modelo de aorta utilizando a velocimetria por imagens esteroscópicas de partículas. 2019. 210 f. PUC-Rio, 2019.

BESSA, Guilherme M.; FERNANDES, Leonardo S.; GOMES, Bruno A.A.; AZEVEDO, Luis F.A. **Influence of aortic valve tilt angle on flow patterns in the ascending aorta**. [*S. l.*]: Springer Berlin Heidelberg, 2021. vol. 62, . DOI 10.1007/s00348-021-03199-3. Available at: https://doi.org/10.1007/s00348-021-03199-3.

BORAZJANI, Iman; GE, Liang; SOTIROPOULOS, Fotis. High-resolution fluid-structure interaction simulations of flow through a bi-leaflet mechanical heart valve in an anatomic aorta. **Annals of Biomedical Engineering**, vol. 38, no. 2, p. 326–344, 2010. https://doi.org/10.1007/s10439-009-9807-x.

BROWN, Alistair G.; SHI, Yubing; MARZO, Alberto; STAICU, Cristina; VALVERDE, Isra; BEERBAUM, Philipp; LAWFORD, Patricia V.; HOSE, D. Rodney. Accuracy vs. computational time: Translating aortic simulations to the clinic. **Journal of Biomechanics**, vol. 45, no. 3, p. 516–523, 2012. DOI 10.1016/j.jbiomech.2011.11.041. Available at: http://dx.doi.org/10.1016/j.jbiomech.2011.11.041.

BURDEN, R. L.; FAIRES, J. D. **Análise Numérica**. [*S. l.*]: Cengage Learning, 2008.

CELIS, Diego. **Numerical study of the influence of tilt valve angle on blood flow in an aortic modele**. 2017. Dissertação de Mestrado. PUC-Rio, 2017.

CELIS, Diego; GOMES, Bruno Alvares de Azevedo; IBANEZ, Ivan; AZEVEDO, Pedro Nieckele; TEIXEIRA, Pedro Soares; NIECKELE, Angela Ourivio. Prediction of stress map in ascending aorta-optimization of the coaxial position in transcatheter aortic valve replacement. **Arquivos Brasileiros de Cardiologia**, vol. 115, no. 4, p. 680–687, 2020. https://doi.org/10.36660/abc.20190385.

CHARITOS, Efstratios I; SIEVERS, Hans-Hinrich. Anatomy of the aortic root: implications for valve-sparing surgery. **Annals of Cardiothoracic Surgery**, vol. 2, no. 1, p. 53–56, 2013. https://doi.org/10.3978/j.issn.2225-319X.2012.11.18.

COURANT, R; FRIEDRICHS, K; LEWY, H. Über die partiellen Differenzengleichungen der mathematischen Physik. **Digizeitschriften e.V**, , p.

44, 1928. .

CROWLEY, Timothy A.; PIZZICONI, Vincent. Isolation of plasma from whole blood using planar microfilters for lab-on-a-chip applications. **Lab on a Chip**, vol. 5, no. 9, p. 922–929, 2005. https://doi.org/10.1039/b502930a.

DAVIES, P. F.; REMUZZI, A.; GORDON, E. J.; DEWEY, C. F.; GIMBRONE, M. A. Turbulent fluid shear stress induces vascular endothelial cell turnover in vitro. **Proceedings of the National Academy of Sciences of the United States of America**, vol. 83, no. 7, p. 2114–2117, 1986. https://doi.org/10.1073/pnas.83.7.2114.

DREŠAR, Primož; RUTTEN, Marcel C.M.; GREGORIČ, Igor D.; DUHOVNIK, Jožef. A numerical simulation of heartassist5 blood pump using an advanced turbulence model. **ASAIO Journal**, vol. 64, no. 5, p. 673–679, 2018. https://doi.org/10.1097/MAT.0000000000000703.

EGOROV, Y.; MENTER, F. R.; LECHNER, R.; COKLJAT, D. The scale-adaptive simulation method for unsteady turbulent flow predictions. part 2: Application to complex flows. **Flow, Turbulence and Combustion**, vol. 85, no. 1, p. 139–165, 2010. https://doi.org/10.1007/s10494-010-9265-4.

FEIJÓ, Vagner. **MODELAGEM DO FLUXO SANGUÍNEO NA AORTA ABDOMINAL UTILIZANDO INTERAÇÃO FLUIDO-ESTRUTURA**. 2007. 2007.

GABRIEL, S. A.; DING, Y.; FENG, Y. Extending the oscillatory index to discern oscillatory flow modes. **Proceedings of the 20th Australasian Fluid Mechanics Conference, AFMC 2016**, no. December, 2016. .

GELIO, Rodrigo Meyer. **Influência de modelos simplificados da valva aórtica no escoamento na aorta ascendente**. 2021. Pontifícia Universidade Católica do Rio de Janeiro (PUC-Rio), 2021.

GOFT, Daniel Mendelson. **Influência do posicionamento angular da prótese valvar na distribuição de tensões em aortas aneurismáticas**. 2020. Pontifícia Universidade Católica do Rio de Janeiro (PUC-Rio), 2020.

GOMES, Bruno Alvares de Azevedo; CAMARGO, Gabriel Cordeiro; DOS SANTOS, Jorge Roberto Lopes; AZEVEDO, Luis Fernando Alzuguir; NIECKELE, Ângela Ourivio; SIQUEIRA-FILHO, Aristarco Gonçalves; DE

OLIVEIRA, Glaucia Maria Moraes. Influência do ângulo de Lnclinação da prótese percutânea aórtica no campo de velocidade e estresse de cisalhamento. **Arquivos Brasileiros de Cardiologia**, vol. 109, no. 3, p. 231–240, 2017. https://doi.org/10.5935/abc.20170115.

HAO, Qing. **Modeling of Flow in an In Vitro Aneurysm Model : A Fluid-Structure Interaction Approach**. [*S. l.*: *s. n.*], 2010.

HARLOFF, Andreas; NUSSBAUMER, Andrea; BAUER, Simon; STALDER, Aurélien F.; FRYDRYCHOWICZ, Alex; WEILLER, Cornelius; HENNIG, Jürgen; MARKL, Michael. In vivo assessment of wall shear stress in the atherosclerotic aorta using flow-sensitive 4D MRI. **Magnetic Resonance in Medicine**, vol. 63, no. 6, p. 1529–1536, 2010. https://doi.org/10.1002/mrm.22383.

HEALTH LITERACY HUB. Aorta Explained - Anatomy 101 For patients. 2021. **Aorta Explained - Anatomy 101 For patients**. Available at: https://healthliteracyhub.com/pt/anatomia-101-blog/estrutura-e-funcao-da-aorta/. Accessed on: 11 Jul. 2021.

HUNT, J C R; WRAY, a a; MOIN, P. Eddies, streams, and convergence zones in turbulent flows. **Center for Turbulence Research, Proceedings of the Summer Program**, no. 1970, p. 193–208, 1988. .

HUSSEIN, Nabil; VOYER-NGUYEN, Pascal; PORTNOY, Sharon; PEEL, Brandon; SCHRAUBEN, Eric; MACGOWAN, Christopher; YOO, Shi-Joon. Simulation of semilunar valve function: computer-aided design, 3D printing and flow assessment with MR. **3D Printing in Medicine**, vol. 6, no. 1, p. 1–9, 2020. https://doi.org/10.1186/s41205-020-0057-8.

HUTCHESON, J. D.; AIKAWA, E. **Heart Valve Disease**. [*S. l.*]: Elsevier Inc., 2014. DOI 10.1016/B978-0-12-386456-7.03308-6. Available at: http://dx.doi.org/10.1016/B978-0-12-386456-7.03308-6.

IBANEZ, Ivan. **Estudo numérico da influência da inclinação da prótese valvar aórtica no fluxo sanguíneo em aorta ascendente Ivan Fernney Ibanez Aguilar Estudo numérico da influência da inclinação da prótese valvar aórtica no fluxo sanguíneo e**. 2019. 2019.

IBANEZ, Ivan; DE AZEVEDO GOMES, Bruno A.; NIECKELE, Angela O. **Effect of percutaneous aortic valve position on stress map in ascending aorta:**

A fluid-structure interaction analysis. [*S. l.*: *s. n.*], 2020. vol. 45, . https://doi.org/10.1111/aor.13883.

JOHNSON, Emily L.; WU, Michael C.H.; XU, Fei; WIESE, Nelson M.; RAJANNA, Manoj R.; HERREMA, Austin J.; GANAPATHYSUBRAMANIAN, Baskar; HUGHES, Thomas J.R.; SACKS, Michael S.; HSU, Ming Chen. Thinner biological tissues induce leaflet flutter in aortic heart valve replacements. **Proceedings of the National Academy of Sciences of the United States of America**, vol. 117, no. 32, p. 19007–19016, 2020. https://doi.org/10.1073/pnas.2002821117.

KALAUN, Karim. **Avaliação Dos Padrões Hemodinâmicos Relacionados Ao Crescimento De Aneurisma Na Aorta Ascendente**. 2019. Pontifícia Universidade Católica do Rio de Janeiro (PUC-Rio), 2019.

KATSI, Vasiliki; MAGKAS, Nikolaos; ANTONOPOULOS, Alexios; TRANTALIS, Georgios; TOUTOUZAS, Konstantinos; TOUSOULIS, Dimitrios. Aortic valve: anatomy and structure and the role of vasculature in the degenerative process. **Acta Cardiologica**, vol. 0, no. 0, p. 1–14, 2020. DOI 10.1080/00015385.2020.1746053. Available at: https://doi.org/10.1080/00015385.2020.1746053.

KLABUNDE, Richard. Cardiovascular Physiology Concepts - Turbulent Flow. 2018. Available at: https://www.cvphysiology.com/Hemodynamics/H007.

KOMUTRATTANANONT, Pornhatai; MAHAKKANUKRAUH, Pasuk; DAS, Srijit. Morphology of the human aorta and age-related changes: Anatomical facts. **Anatomy and Cell Biology**, vol. 52, no. 2, p. 109–114, 2019. https://doi.org/10.5115/acb.2019.52.2.109.

KU, D. N.; GIDDENS, D. P.; ZARINS, C. K.; GLAGOV, S. Pulsatile flow and atherosclerosis in the human carotid bifurcation. Positive correlation between plaque location and low and oscillating shear stress. **Arteriosclerosis**, vol. 5, no. 3, p. 293–302, 1985. https://doi.org/10.1161/01.atv.5.3.293.

LANGTRY, Robin B.; MENTER, Florian R. Correlation-based transition modeling for unstructured parallelized computational fluid dynamics codes. **AIAA Journal**, vol. 47, no. 12, p. 2894–2906, 2009. https://doi.org/10.2514/1.42362.

LANTZ, Jonas; GÅRDHAGEN, Roland; KARLSSON, Matts. Quantifying turbulent wall shear stress in a subject specific human aorta using large eddy simulation. **Medical Engineering and Physics**, vol. 34, no. 8, p. 1139–1148, 2012. DOI 10.1016/j.medengphy.2011.12.002. Available at: http://dx.doi.org/10.1016/j.medengphy.2011.12.002.

LEE, Byoung Kwon. Computational fluid dynamics in cardiovascular disease. **Korean Circulation Journal**, vol. 41, no. 8, p. 423–430, 2011. https://doi.org/10.4070/kcj.2011.41.8.423.

LO, Ernest W.C.; MENEZES, Leon J.; TORII, Ryo. Impact of inflow boundary conditions on the calculation of CT-based FFR. **Fluids**, vol. 4, no. 2, p. 1–16, 2019. https://doi.org/10.3390/fluids4020060.

MADHAVAN, Sudharsan; KEMMERLING, Erica M.Cherry. The effect of inlet and outlet boundary conditions in image-based CFD modeling of aortic flow. **BioMedical Engineering Online**, vol. 17, no. 1, p. 1–20, 2018. DOI 10.1186/s12938-018-0497-1. Available at: https://doi.org/10.1186/s12938-018-0497-1.

MANCHESTER, Emily L.; PIROLA, Selene; SALMASI, Mohammad Yousuf; O'REGAN, Declan P.; ATHANASIOU, Thanos; XU, Xiao Yun. Analysis of Turbulence Effects in a Patient-Specific Aorta with Aortic Valve Stenosis. **Cardiovascular Engineering and Technology**, vol. 12, no. 4, p. 438–453, 2021. https://doi.org/10.1007/s13239-021-00536-9.

MENTER, F. R. Two-equation eddy-viscosity turbulence models for engineering applications. **AIAA Journal**, vol. 32, no. 8, p. 1598–1605, 1994. https://doi.org/10.2514/3.12149.

MENTER, F. R.; LANGTRY, R. B.; LIKKI, S. R.; SUZEN, Y. B.; HUANG, P. G.; VÖLKER, S. A correlation-based transition model using local variables - Part I: Model formulation. **Journal of Turbomachinery**, vol. 128, no. 3, p. 413–422, 2006. https://doi.org/10.1115/1.2184352.

MOSTAFA, Sheikh Shanawaz; ISLAM, Muhammad Muinul; AHMAD, Mohiuddin. Correlation of Heart-rate and Cardiac Cycle Duration under Different Body Positions and Breathing. **International Conference on Advances in Electrical Engineering**, no. September 2014, 2011. .

OSTADFAR, Ali. **Biofluid Dynamics in Human Organs**. [*S. l.*: *s. n.*], 2016. https://doi.org/10.1016/b978-0-12-802408-9.00004-1.

PATANKAR, Suhas V. **Numerical Heat Transfer and Fluid Flow**. [*S. l.*: *s. n.*], 1980.

PEROCCO, Enrico Luigi M; GELIO, Rodrigo Meyer L; NIECKELE, Angela O. IMPACT OF AORTIC VALVE TOPOLOGY IN THE HEMODYNAMIC FLOW PATTERNS IN THE ASCENDING AORTA. **International Congress of Mechanical Engineering**, no. 1999, 2021. .

PIAZZA, Nicoló; DE JAEGERE, Peter; SCHULTZ, Carl; BECKER, Anton E.; SERRUYS, Patrick W.; ANDERSON, Robert H. Anatomy of the aortic valvar complex and its implications for transcatheter implantation of the aortic valve. **Circulation. Cardiovascular interventions**, vol. 1, no. 1, p. 74–81, 2008. https://doi.org/10.1161/CIRCINTERVENTIONS.108.780858.

PINHO, Hannah Alves. **Análise numérica do escoamento em aorta ascendente**. 2016. Pontifícia Universidade Católica do Rio de Janeiro (PUC-Rio), 2016.

POPE, S.B. **Turbulent flows**. [*S. l.*]: IOP Publishing, 2001.

REYMOND, Philippe; CROSETTO, Paolo; DEPARIS, Simone; QUARTERONI, Alfio; STERGIOPULOS, Nikos. Physiological simulation of blood flow in the aorta: Comparison of hemodynamic indices as predicted by 3-D FSI, 3-D rigid wall and 1-D models. **Medical Engineering and Physics**, vol. 35, no. 6, p. 784–791, 2013. DOI 10.1016/j.medengphy.2012.08.009. Available at: http://dx.doi.org/10.1016/j.medengphy.2012.08.009.

SCHMITT, G. About Boussinesq ' s turbulent viscosity hypothesis : François G Schmitt To cite this version : HAL Id : hal-00264386 About Boussinesq ' s turbulent viscosity hypothesis : historical remarks and a direct evaluation of its validity. **Comptes Rendus Mécanique, Elsevier Masson**, vol. 10, p. 617–627, 2008. .

SCOVILLE, Heather. Evolution of the Human Heart into Four Chambers. 2020. **Thought.co**. Available at: https://www.thoughtco.com/evolution-of-the-human-heart-1224781. Accessed on: 29 Jun. 2021.

SEDOV, L. I.; HODGE, P. G. **Introduction to the Mechanics of a Continuous Medium**. [*S. l.*: *s. n.*], 1966. vol. 33, . https://doi.org/10.1115/1.3625016.

SIMAO, Mariana; FERREIRA, Jorge M.; TOMAS, Antonio C.; FRAGATA, Jose; RAMOS, Helena M. Aorta ascending aneurysm analysis using CFD models towards possible anomalies. **Fluids**, vol. 2, no. 2, p. 1–15, 2017. https://doi.org/10.3390/fluids2020031.

SINGH, S. D.; XU, X. Y.; WOOD, N. B.; PEPPER, J. R.; IZGI, C.; TREASURE, T.; MOHIADDIN, R. H. Aortic flow patterns before and after personalised external aortic root support implantation in Marfan patients. **Journal of Biomechanics**, vol. 49, no. 1, p. 100–111, 2016. https://doi.org/10.1016/j.jbiomech.2015.11.040.

TAN, F. P.P.; SOLOPERTO, G.; BASHFORD, S.; WOOD, N. B.; THOM, S.; HUGHES, A.; XU, X. Y. Analysis of flow disturbance in a stenosed carotid artery bifurcation using two-equation transitional and turbulence models. **Journal of Biomechanical Engineering**, vol. 130, no. 6, p. 1–12, 2008. https://doi.org/10.1115/1.2978992.

TANG, A. Y.S.; FAN, Y.; CHENG, S. W.K.; CHOW, K. W. Biomechanical factors influencing type b thoracic aortic dissection: Computational fluid dynamics study. **Engineering Applications of Computational Fluid Mechanics**, vol. 6, no. 4, p. 622–632, 2012. https://doi.org/10.1080/19942060.2012.11015447.

VERGARA, Christian; LE VAN, Davide; QUADRIO, Maurizio; FORMAGGIA, Luca; DOMANIN, Maurizio. Large eddy simulations of blood dynamics in abdominal aortic aneurysms. **Medical Engineering and Physics**, vol. 47, p. 38–46, 2017. DOI 10.1016/j.medengphy.2017.06.030. Available at: http://dx.doi.org/10.1016/j.medengphy.2017.06.030.

WESTERHOF, Nico; LANKHAAR, Jan Willem; WESTERHOF, Berend E. The arterial windkessel. **Medical and Biological Engineering and Computing**, vol. 47, no. 2, p. 131–141, 2009. https://doi.org/10.1007/s11517-008-0359-2.

WILCOX, D. C. **Turbulence modeling for CFD**. [*S. l.*]: D C W Industries, 1993.

WORLD HEALTH ORGANIZATION. The top 10 causes of death. 9 Dec. 2019. Available at: https://www.who.int/news-room/fact-sheets/detail/the-top-10-causes-of-death. Accessed on: 4 May 2022.

YOUNSI, M.; DJERRADA, A.; BELAMRI, T.; MENTER, F. Application of the SAS turbulence model to predict the unsteady flow field behaviour in a forward centrifugal fan. **International Journal of Computational Fluid Dynamics**, vol. 22, no. 9, p. 639–648, 2008. https://doi.org/10.1080/10618560802432944.

APPENDIX

This appendix contains additional results from Chapter 5 of this work, where comparison of three turbulence models with experimental data was presented. The mean relative and absolute error of plane average values of the velocity vector components and for the six components of the Reynolds tensor of each model in relation to the experimental data are shown in the following tables.

Table A.1 - Relative error for mean quantity for planes 1-6

	Relative error - Plane 1			Relative error - Plane 2			Relative error - Plane 3		
Quantity	SAS	κ-ω	Transitional	SAS	κ-ω	Transitional	SAS	κ-ω	Transitional
umean	-39%	69%	28%	317%	1741%	3023%	58%	53%	119%
vmean	-26%	-1%	0%	-25%	-32%	-35%	-59%	-77%	-81%
wmean	-15%	-16%	-18%	-13%	-13%	-10%	5%	12%	15%
kmean	44%	352%	814%	55%	287%	531%	21%	197%	328%
R12mean	-105%	-448%	-1180%	-230%	-516%	-413%	420%	1008%	1125%
R23mean	-100%	-101%	-87%	-99%	-99%	-77%	-101%	-75%	-38%
R13mean	-100%	-101%	-87%	-99%	-99%	-77%	-101%	-75%	-38%
R11mean	352%	1302%	2734%	237%	734%	1280%	85%	357%	568%
R22mean	-20%	157%	395%	9%	167%	315%	-10%	113%	201%
R33mean	70%	426%	1021%	40%	262%	509%	23%	208%	349%
Average	6%	164%	362%	19%	243%	505%	34%	172%	255%

	Relative Error - Plane 4			Relative Error - Plane 5			Relative Error - Plane 6		
Quantity	SAS	κ-ω	Transitional	SAS	κ-ω	Transitional	SAS	κ-ω	Transitional
umean	28%	-1%	-10%	-25%	-29%	-34%	-178%	-56%	-65%
vmean	-105%	-112%	-109%	353%	344%	343%	-176%	-168%	-172%
wmean	21%	23%	23%	21%	18%	15%	36%	30%	25%
kmean	-42%	43%	101%	-150%	0%	99%	-55%	8%	40%
R12mean	-68%	-21%	23%	-216%	-108%	-24%	-107%	-209%	-201%
R23mean	14%	371%	750%	801%	968%	1107%	-112%	-122%	-131%
R13mean	14%	371%	750%	801%	968%	1107%	-112%	-122%	-131%
R11mean	-1%	145%	244%	-57%	92%	194%	-36%	56%	106%
R22mean	-54%	13%	57%	-230%	-74%	25%	-66%	-17%	9%
R33mean	-49%	26%	78%	-157%	-13%	82%	-52%	10%	39%
Average	-24%	86%	191%	114%	217%	291%	-86%	-59%	-48%

Table A.2 - Absolute error for mean quantity for planes 1-6

	Absolute error - Plane 1			Absolute error - Plane 2			Absolute error - Plane 3		
Quantity	SAS	κ-ω	Transitional	SAS	κ-ω	Transitional	SAS	κ-ω	Transitional
umean	1%	1%	-1%	-1%	-3%	-6%	-2%	-1%	-3%
vmean	-8%	-12%	-14%	-7%	-8%	-9%	-15%	-20%	-21%
wmean	-5%	-9%	-9%	-3%	-3%	-2%	1%	3%	4%
kmean	0%	2%	6%	1%	5%	10%	1%	6%	9%
R12mean	0%	0%	0%	0%	0%	0%	0%	0%	0%
R23mean	-1%	-1%	-1%	-1%	-1%	-1%	-1%	-1%	0%
R13mean	-1%	-1%	-1%	-1%	-1%	-1%	-1%	-1%	0%
R11mean	1%	2%	5%	1%	4%	7%	1%	4%	7%
R22mean	0%	1%	4%	0%	3%	6%	0%	3%	5%
R33mean	0%	1%	4%	1%	4%	7%	0%	4%	7%
Average	-1%	-1%	-1%	-1%	0%	1%	-2%	0%	1%

	Absolute error - Plane 4			Absolute error - Plane 5			Absolute error - Plane 6		
Quantity	SAS	κ-ω	Transitional	SAS	κ-ω	Transitional	SAS	κ-ω	Transitional
umean	-2%	0%	1%	2%	2%	3%	2%	1%	1%
vmean	-30%	-32%	-31%	-43%	-42%	-42%	-48%	-46%	-47%
wmean	6%	6%	7%	8%	7%	6%	10%	8%	7%
kmean	-2%	2%	6%	-5%	0%	3%	-4%	1%	3%
R12mean	0%	0%	0%	0%	0%	0%	0%	0%	0%
R23mean	0%	0%	1%	2%	3%	3%	2%	2%	2%
R13mean	0%	0%	1%	2%	3%	3%	2%	2%	2%
R11mean	0%	3%	5%	-1%	2%	4%	-1%	2%	3%
R22mean	-3%	1%	3%	-5%	-2%	1%	-4%	-1%	1%
R33mean	-2%	1%	4%	-3%	0%	2%	-2%	0%	2%
Average	-3%	-2%	0%	-4%	-3%	-2%	-4%	-3%	-3%

Table A.3 - Relative error for maximum quantity for planes 1-3

	Relative error –Plane 1			Relative error - Plane 2			Relative error - Plane 3		
Quantity	SAS	κ-ω	Transitional	SAS	κ-ω	Transitional	SAS	κ-ω	Transitional
umax	246%	253%	120%	98%	161%	117%	12%	55%	35%
vmax	-20%	-24%	-21%	-19%	-24%	-23%	-21%	-33%	-40%
wmax	-15%	-24%	-22%	-14%	-24%	-24%	-14%	-26%	-30%
umin	69%	91%	68%	132%	268%	241%	88%	65%	41%
vmin	76%	-31%	1%	113%	231%	216%	262%	319%	275%
wmin	136%	284%	266%	264%	247%	247%	151%	190%	206%
kmax	-64%	-5%	70%	-51%	5%	52%	-39%	21%	53%
R12max	303%	980%	2286%	87%	289%	482%	-60%	-16%	6%
R23max	-95%	-92%	-78%	-95%	-91%	-86%	-92%	-83%	-74%
R13max	174%	431%	1003%	22%	77%	255%	-25%	7%	55%
R11max	214%	704%	1245%	58%	239%	393%	-66%	-36%	-17%
R22max	-76%	-39%	-9%	-73%	-36%	-22%	-58%	-21%	-19%
R33max	-45%	27%	186%	-11%	80%	177%	-7%	98%	150%
Average	69%	197%	394%	39%	109%	156%	10%	42%	49%

Table A.4 - Relative error for maximum quantity for planes 4-6

	Relative Error - Plane 4			Relative Error - Plane 5			Relative Erro - Plane 6		
Quantity	SAS	κ-ω	Transitional	SAS	κ-ω	Transitional	SAS	κ-ω	Transitional
umax	4%	27%	20%	-2%	-9%	-14%	5%	-21%	-30%
vmax	-13%	-35%	-47%	-8%	-30%	-37%	-43%	-38%	-41%
wmax	-13%	-24%	-30%	-4%	-20%	-28%	24%	-1%	-15%
umin	6%	-22%	-35%	24%	-14%	-30%	74%	7%	-10%
vmin	294%	232%	171%	717%	504%	397%	505%	333%	259%
wmin	65%	91%	110%	209%	79%	115%	89%	-4%	-35%
kmax	-90%	-83%	-79%	-71%	-63%	-52%	-66%	-61%	-50%
R12max	-85%	-69%	-66%	-90%	-86%	-87%	-93%	-94%	-92%
R23max	-97%	-95%	-94%	-44%	-28%	-7%	-64%	-60%	-58%
R13max	-81%	-68%	-55%	-65%	-56%	-50%	-77%	-73%	-73%
R11max	-72%	-56%	-45%	-77%	-73%	-65%	-85%	-83%	-79%
R22max	-90%	-81%	-78%	-87%	-81%	-75%	-80%	-76%	-70%
R33max	-93%	-89%	-86%	-80%	-75%	-68%	-80%	-78%	-71%
Average	-20%	-21%	-24%	32%	4%	0%	8%	-19%	-28%

Table A. 5 - Absolute error for maximum quantity for planes 1-3

	Absolute error - Plane 1			Absolute error - Plane 2			Absolute error - Plane 3		
	SAS	κ-ω	Transitional	SAS	κ-ω	Transitional	SAS	κ-ω	Transitional
umax	17%	18%	8%	13%	21%	15%	4%	18%	12%
vmax	-42%	-51%	-44%	-40%	-49%	-48%	-41%	-65%	-76%
wmax	-41%	-64%	-58%	-35%	-62%	-63%	-35%	-63%	-74%
umin	-10%	-13%	-9%	-21%	-43%	-39%	-49%	-37%	-23%
vmin	-11%	5%	0%	-17%	-35%	-33%	-41%	-50%	-43%
wmin	-20%	-42%	-39%	-40%	-38%	-38%	-24%	-30%	-32%
kmax	-12%	-1%	13%	-11%	1%	11%	-8%	4%	11%
R12max	1%	2%	6%	1%	3%	5%	-3%	-1%	0%
R23max	-14%	-13%	-11%	-17%	-16%	-15%	-14%	-12%	-11%
R13max	1%	2%	6%	0%	1%	4%	-1%	0%	2%
R11max	3%	11%	19%	2%	10%	16%	-15%	-8%	-4%
R22max	-21%	-11%	-2%	-23%	-11%	-7%	-16%	-6%	-5%
R33max	-5%	3%	19%	-1%	10%	21%	-1%	13%	19%
Average	-12%	-12%	-7%	-15%	-16%	-13%	-19%	-18%	-17%

Table A 6 - Absolute error for maximum quantity for planes 4-6

	Absolute error - Plane 4			Absolute error - Plane 5			Absolute error - Plane 6		
	SAS	κ-ω	Transitional	SAS	κ-ω	Transitional	SAS	κ-ω	Transitional
umax	2%	11%	8%	-1%	-5%	-9%	4%	-17%	-24%
vmax	-16%	-44%	-58%	-4%	-16%	-20%	-33%	-29%	-31%
wmax	-33%	-61%	-77%	-10%	-48%	-70%	44%	-1%	-28%
umin	-7%	27%	43%	-25%	15%	32%	-43%	-4%	6%
vmin	-63%	-50%	-37%	-90%	-63%	-50%	-120%	-79%	-61%
wmin	-14%	-20%	-24%	-26%	-10%	-14%	-21%	1%	8%
kmax	-123%	-114%	-108%	-41%	-36%	-30%	-32%	-30%	-25%
R12max	-9%	-7%	-7%	-16%	-15%	-15%	-24%	-25%	-24%
R23max	-92%	-90%	-88%	-4%	-2%	-1%	-8%	-8%	-7%
R13max	-7%	-6%	-5%	-4%	-4%	-3%	-7%	-7%	-7%
R11max	-23%	-18%	-15%	-37%	-35%	-32%	-63%	-61%	-58%
R22max	-71%	-64%	-62%	-62%	-58%	-53%	-54%	-51%	-47%
R33max	-180%	-172%	-167%	-50%	-48%	-43%	-38%	-37%	-34%
Average	-49%	-47%	-46%	-28%	-25%	-24%	-30%	-27%	-26%